UNIVERSITÀ
DEGLI STUDI
DI PADOVA

SEDE AMMINISTRATIVA:

UNIVERSITÀ DEGLI STUDI DI PADOVA

DIPARTIMENTO DI FISICA E ASTRONOMIA

CORSO DI DOTTORATO DI RICERCA IN: PHYSICS
CICLO XXXVI

Study of the proton-induced production of the theranostic radionuclide ^{47}Sc

TESI REDATTA CON IL CONTRIBUTO FINANZIARIO DEI LABORATORI NAZIONALI DI LEGNARO DELL'ISTITUTO NAZIONALE DI FISICA NUCLEARE

Coordinatore: CH.MO PROF. GIULIO MONACO
Supervisore: CH.MA PROF.SSA LAURA DE NARDO
Co-supervisori: DOTT.SSA GAIA PUPILLO E DOTT.SSA LILIANA MOU

Dottoranda: LUCIA DE DOMINICIS

Anno Accademico 2022/2023

Abstract

The research activities reported in this thesis were conducted in the framework of a collaboration between the Physics and Astronomy Department of the Padova University and the Legnaro National Laboratories of the National Institute of Nuclear Physics (INFN-LNL), where the LARAMED (LAboratory of RADionuclides for MEDicine) project was developed since 2012. The aim of this project is to investigate new or alternative cyclotron-based production routes for standard or emerging medical radionuclides for innovative radiopharmaceuticals.

^{47}Sc is a promising theranostic radionuclide thanks to its γ and β^- decay emissions which can be employed in imaging and therapeutic medical applications, respectively. At present, the challenge is to find a valid production route which allows to obtain large and enough pure quantities. The first step to evaluate a possible production route is the measurement of the cross-sections. For this reason, in this work the proton-induced nuclear reactions on enriched ^{48}Ti, ^{49}Ti and ^{50}Ti targets are presented, concerning not only the production of ^{47}Sc but also of its contaminants, namely ^{43}Sc, ^{44m,g}Sc, ^{46}Sc, ^{48}Sc, ^{48}V, and ^{43}K. Co-produced contaminants play a key role in the assessment of the purity of the final product: their production has to be avoided to reduce the useless radiation dose to a patient. The quantification of the extra dose administered to human organs is possible through dosimetric simulations. In this thesis dosimetric analysis for the production routes involving enriched ^{48}Ti, ^{49}Ti and ^{50}Ti targets and the ^{nat}V are provided, considering the DOTA-folate conjugate cm10 as an example of radiopharmaceutical. Limitation in the amount of the additional dose due to co-produced contaminants allows to individuate which are the optimal beam energy interval and irradiation time for the ^{47}Sc production.

From cross-section trends and dosimetric studies, with also the support of theoretical simulations performed by collaborators expert in nuclear modelling, a multilayer target composed by a first layer of ^{nat}V and a second layer of ^{50}Ti was designed, and described in an INFN patent (request number 102023000018477), to maximize the ^{47}Sc production keeping the activity of contaminants below 1%.

Contents

Introduction

The first use of radiation for therapeutic applications dates back to January 1896, immediately after the discovery of X-rays by Roentgen in November 1895, when these "new rays" were used to treat a breast cancer [1]. It was the beginning of a huge progress, over the decades, involving scientists from different fields, such as physics, medicine, chemistry, and engineering. The work of this scientific community led to the artificial production of the radiation for medical use at the Oak Ridge National Laboratory in 1946 [2]. Radionuclides started to be produced to study the physiological processes and to non-invasively diagnose, stage, and treat the diseases, which is the aim of the modern nuclear medicine. The vehicle to bring the radiation to the affected cells is the radiopharmaceutical. A radiopharmaceutical is either a radionuclide alone, such as iodine-131, or a radionuclide attached to a carrier molecule (a drug, a protein, a peptide...) which, when introduced into the body by injection, inhalation or ingestion, accumulates in the organ or tissue of interest. Depending on the type of radiation emitted by the radionuclide, the radiopharmaceutical can be used for imaging or treatment purposes, or both. The use of a well-combined pair of radionuclides that allows to perform both therapy and diagnosis, such as the β^+ emitter ^{68}Ga matched with the therapeutic ^{177}Lu, is the basis of the theranostic approach [3]. The real theranostic pair is composed by two radioisotopes of the same chemical element, enabling the use of the same targeting molecule. Although, the most recent theranostic approach includes the use of a single radionuclide emitting a therapeutic radiation together with a low energy γ ray detectable with SPECT (Single Photon Emission Computed Tomography) cameras for imaging, as it is ^{47}Sc. One of the most promising aspects of theranostics is its step towards personalized medicine: through a deeper understanding of physiological and pathological processes it is possible to predict the patient response to the treatment and so to increase therapeutic successes. Theranostic radionuclides can be used at different stages in the diseases' treatment, starting from the detection and diagnosis up to the

treatment, the progression assessment, and the long-term follow-up, to provide a therapeutic plan adjusted according to the uniqueness of the patient.

In response to the personalized medicine implementation, the International Atomic Energy Agency (IAEA) expressed the need to study additional theranostic radionuclides, in particular ^{67}Cu, ^{186}Re, and ^{47}Sc, in a specific coordinated research project [4].

At the Legnaro National Laboratories of the National Institute of Nuclear Physics (INFN-LNL) this demand was supported in the context of LARAMED (LAboratories of RAdionuclides for MEDicine) project which aims to investigate new cyclotron-based production routes for emerging medical radionuclides, but also, to identify alternative production routes for conventional ones. These challenges have been faced by the LARAMED team through several dedicated projects, funded by INFN, since 2012, and described in details in [5, 6]. The main ones are: APOTEMA and TECHN-OSP for the production of the conventional ^{99m}Tc, the gold standard radionuclide for SPECT imaging; COME and CUPRUM_TTD for the emerging theranostic radionuclide ^{67}Cu production; METRICS concerning the production of ^{52}Mn, for multi-modal imaging PET-MRI (Positron Emission Tomography-Magnetic Resonance Imaging); PASTA and REMIX focused on ^{47}Sc and Tb-family productions. Whatever the chosen radionuclide is, to obtain a high yield all the steps of the production process have to be refined and this requires a solid and heterogeneous workgroup composed by scientists from different fields, such as physics, engineering, radiochemistry, medical physics, and nuclear medicine.

In such a multidisciplinary context, this Ph.D. thesis deals with the nuclear cross-section evaluations of the emerging radionuclide ^{47}Sc. The properties of this radionuclide that make it a suitable candidate for medical applications are its β^- emission (mean energy= 162 keV [7]), useful for therapy, and the associated γ ray of 159 keV [7], useful for imaging with SPECT cameras. Moreover, ^{47}Sc has a half-life of 3.3492 d [7] which allows to follow the slow biodistribution of large molecules in the body. It can also be paired to the β^+ emitters counterparts ^{44m}Sc and ^{43}Sc to have the possibility to also perform PET (Positron Emission Tomography) imaging exploiting the same carrier molecule.

The knowledge of the cross-sections as a function of the beam energy of all the co-produced radionuclides is a necessary first step to individuate a possible energy interval in which the ^{47}Sc production is maximized while the presence of co-produced contaminants is minimized. Usually, to achieve this objective

expensive enriched target materials are required. In fact, in this work proton-induced reactions on enriched ^{48}Ti, ^{49}Ti, and ^{50}Ti targets, properly manufactured at the INFN-LNL in the context of the E_PLATE project, were investigated up to 70 MeV.

Yields deduced from cross-section trends are exploited in dosimetric evaluations to assess which are the optimal irradiation conditions, in terms of energy of the beam and duration of the irradiation, for the production of ^{47}Sc. In radiopharmaceutical-dependent dosimetric simulations, the doses administered to a patient due to both ^{47}Sc and its potentially present contaminants are estimated. Irradiation parameters determination is based on the limitation of the dose given by contaminants which can be useless or even harmful for a patient. The ^{nat}V(p,x)^{47}Sc production route is also considered in dosimetric calculations performed during my Ph.D. activities.

The work presented here is the outcome of the PASTA project, funded by CSN5 scientific commission of the INFN for the years 2017-2018, and of the REMIX project, funded by INFN-CSN5 for the years 2021-2023. It is organized in the following 5 chapters.

Chapter 1. Firstly, the radiopharmaceuticals' structure and their employment in medical applications are described. A brief presentation of ^{47}Sc as an emerging medical radionuclide is also given.

Chapter 2. An excursus of the main radionuclides production methods is done, with a focus on the possible routes for ^{47}Sc production proposed up to now, worldwide and at the INFN-LNL.

Chapter 3. The activation experiments performance is described, from the targets manufacturing and their irradiation, to γ spectroscopy and data analysis, presenting the cross-section calculation formalism.

Chapter 4. Cross-section results obtained for the enriched Ti targets are presented and discussed to individuate energy intervals suitable for ^{47}Sc production.

Chapter 5. Dosimetric simulations performance with two different software are outlined and results analysed to establish the best irradiation parameters for any production route.

Chapter 1

The role of radionuclides in nuclear medicine

Nuclear medicine is the field of medicine that uses a trace amount of a radioactive substance (in the order of μg on average for diagnostic tests [8]), radionuclides in their elemental form or in stable compounds, for diagnosis and treatment of many health conditions such as cancers, neurological diseases, or heart diseases [9]. Nowadays, over 40 million nuclear medicine procedures are performed each year worldwide, and this number is constantly increasing [10]. Especially the diagnostic procedures are now routine. Over 10,000 hospitals worldwide use radioisotopes, and about 90% of the procedures are for diagnosis. The most common used radionuclide in diagnosis is ^{99m}Tc. It is estimated to be used in almost 85% of the nuclear medicine diagnostic scans, which corresponds to about 30 million patient examinations per year [11]. All these nuclear medicine procedures require the use of a radiopharmaceutical to target specific organs or deliver localized radiation to the diseased cells.

1.1 Definition and mode of action of a radiopharmaceutical

A radiopharmaceutical is a chemical complex that contains radioactive atoms within its structure suitable and safe for human administration for diagnosis or treatment of a disease. Over the years, three generations of radiopharmaceuticals emerged, based on chemical structure and localization specificity [12].

First generation radiopharmaceuticals. They are simple labelled molec-

ular species targeting specific organs through a non-substrate-specific localization mechanism or particles able to participate to physiological body processes.

This is the case, for example, of iodine which has a tropism for thyroid glands since it is an essential component of the thyroid hormones. When introduced in human body, the radioactive ^{123}I or ^{131}I accumulates in thyroid and allows the imaging or treatment, respectively, of some types of thyroid cancers. This practice started in 1940s. A similar natural affinity is typical also of thallium which behaves similarly to potassium in the myocardium. After infarction, the potassium accumulates less in the heart muscle. If the radioactive ^{201}Tl is used, a reduced radioactivity is registered after a heart attack and the viability of the cardiac muscle can be visualized.

Second generation radiopharmaceuticals. From 1980's, the development of coordination compounds, with the radionuclide bonded through ligands in a well-defined geometry, led to the second generation agents. They are taken up or metabolized by specific organs.

Belongs to this generation the radiopharmaceutical ^{18}FDG (fluorodeoxyglucose). ^{18}FDG is used to monitor the glucose metabolism of the cells. Normal glucose enters the cells thanks to a transporter expressed on the cells' membrane, the GLUT1 carrier, and consequently the same happens to the glucose analogue. Cancer cells are characterized by a higher rate of duplication, that requires a lot of energy which means an abnormally high glucose consumption. In this way, the higher accumulation of these glucose analogues radiolabelled with ^{18}F in tumour cells helps visualizing the cancerous area. Another example is the ^{99m}Tc-MAG3 complex, used in renal tubular clearance studies. Molecular diagrams of both the molecules are reported in figure 1.1.

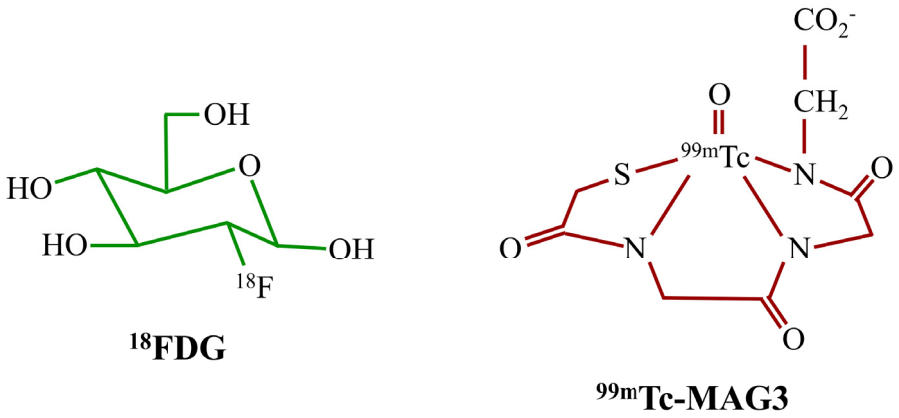

Figure 1.1: ^{18}FDG (single bond) and ^{99m}Tc-MAG3 (complexation bond) molecular diagrams.

Third generation radiopharmaceuticals. In the 1990's, the concept of bifunctional chelating agents (BFCA) was developed. In radiopharmaceuticals designed through this approach, the ligands not only chelate the radionuclide but they can also be modified with functional groups able to control the biodistribution of the final complex. For this reason, third generation radiopharmaceuticals are considered target-specific or receptor-specific. A third generation radiopharmaceutical, represented in figure 1.2, is composed of three main parts:

- The radionuclide of interest which is incorporated in a radioactive compound that keeps the radionuclide in a chemically stable form for the time necessary to reach the targeted cells (e.g., cancer cells).
- The targeting molecule (e.g., small proteins, peptides, fragments of monoclonal antibody or nanoparticles) which is able to recognize and selectively bind to cancer cells. Diseased cells are often characterized by the overexpression of a specific target, such as an antigen or a receptor. Therefore, the vector should be selected on the basis of its affinity with the target. For example, an antibody is capable of binding specifically to an antigen, and a small peptide selectively binds to the overexpressed receptor.
- The BFCA which strongly coordinates the radionuclide and is covalently bonded to the bioactive targeting fragment, directly or via a linker.

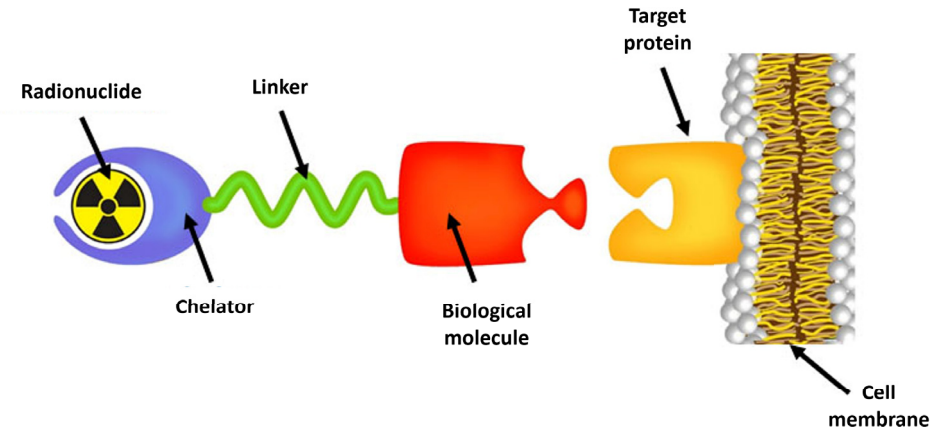

Figure 1.2: Structure of a third generation radiopharmaceutical.

These third generation radiopharmaceuticals are the focus of the current scientific research interest.

There are some ideal characteristics for a radiopharmaceutical that should be considered in the design of a new one [13]:

- **Easy availability.** The radiopharmaceutical should be easily produced, simply available in nuclear medicine departments, and not excessively expensive.
- **Short effective half-life.** A radionuclide decays with its proper physical half-life. A radiopharmaceutical disappears from the body though urinary excretion, perspiration, and similar mechanisms, determining a biological half-life. The combination of physical and biological half-lives gives the effective half-life which should be short enough to not exceed the time of the medical procedure, but, at the same time, should be long enough to allow the medical procedure performance.
- **High target-to-nontarget activity ratio.** It is desirable that the radiopharmaceutical localizes preferentially in the organ of interest. In case of diagnostic studies, the activity coming from nontarget areas can cause the obscuration of structural details in the picture. In therapeutic procedures, a low target-to-nontarget activity ratio can mean an extra exposition of healthy tissues to radiation.

An ideal radiopharmaceutical should satisfy the above requirements to guarantee the efficacy of the medical procedure with a minimum radiation dose to the patient. However, it is difficult to meet all these criteria, and the radiopharmaceutical of choice is the best of many compromises.

1.2 Nuclear imaging through radiopharmaceuticals

Nuclear imaging is the tool exploited in nuclear medicine to perform diagnosis of many human body diseases and tumours. The functional image, obtainable through PET or SPECT imaging, gives information regarding the expression of a molecule or a receptor, or the metabolism and functioning of an organ, but not the precise anatomy of the body area affected by the disease. This is why, currently, there is a high interest in the hybrid combination of the functional imaging with other medical imaging modalities to get the anatomical information with a better spatial resolution about soft tissues (with the Magnetic Resonance Imaging, MRI) and bones or lungs (with the Computed Tomography, CT) [14].

A radionuclide included in a radiopharmaceutical for diagnostic applications must provide a γ ray emission able to get out of the human body to be detected. In fact, gamma rays have a high penetrating power, as can be seen in figure 1.3. They can easily cross skin or clothing, unlike alpha of beta particles, and only many centimetres of lead can stop them.

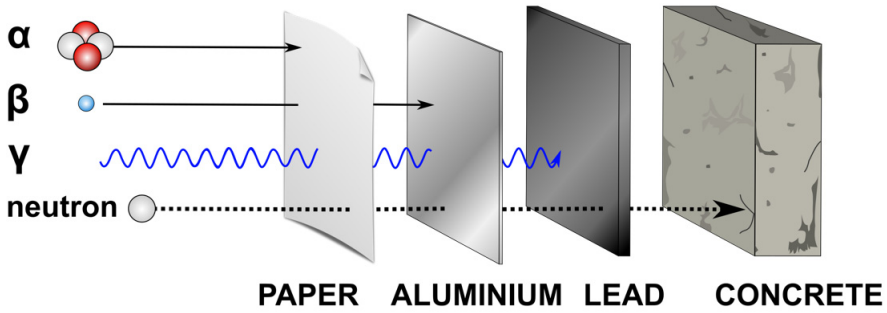

Figure 1.3: Penetrating power of diverse types of radiation.

Usually, the needed γ rays can be directly emitted by a nucleus or can be the result of a β^+ annihilation process.

The first process, known as γ decay, typically occurs in excited state nuclei. The disposition of protons and neutrons in a nucleus can be considered similar to that of electrons in an atom: on discrete energy states. So, exactly as for electrons, an excited state of the nucleus consists in a proton or a neutron that jumped from its ground state to a higher energy state, usually after undergoing an α or a β decay. The nucleus in this excited state has a surplus of energy that has to be released somehow. The emission of a γ ray is the way in which the nucleus releases this energy and goes back to its ground state or at least to a less energetic state. Those γ rays directly emitted by the nucleus are the ones employed in diagnostic exams performed with SPECT cameras. In figure 1.4 the γ decay scheme of the gold standard for SPECT imaging, ^{99m}Tc, is represented, as example, and the γ ray exploited for nuclear imaging is highlighted.

On the other hand, a pair of γ rays can be generated in the annihilation process of a β^+ particle. The β decay occurs when there is a disequilibrium in the number of protons and neutrons in a nucleus. To try to reach a balance in the nucleus, a nucleon transmutes into the other, with a subsequent release of particles to respect the physical conservation laws. Specifically, when there are too many protons a proton transforms into a neutron and one positron and one neutrino are emitted. This is called β^+ decay.

When emitted in a medium, a positron runs a very short distance because

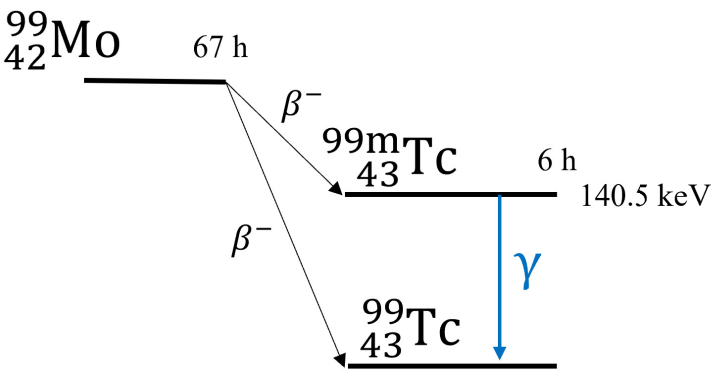

Figure 1.4: Simplified γ decay scheme of ^{99m}Tc.

immediately interacts with an electron of the medium and annihilates. This is the case of a β^+ particle emitted by a medical radionuclide in the human body: it quickly encounters the electrons of the atoms constituting the tissues and annihilates. The result of the annihilation process is a couple of γ photons of the same energy, namely 511 keV, the rest energy of an electron or a positron, moving in the same direction but towards opposite sides. The interaction is shown in figure 1.5. The two γ rays simultaneously generated in this way can be exploited in medical imaging with the PET technique.

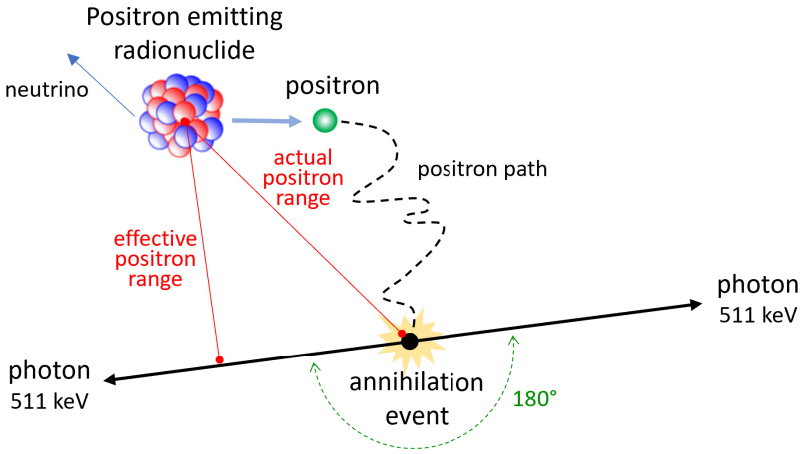

Figure 1.5: Annihilation process for a positron emitted in β^+ decay. The positron range in tissue before annnihilation is approximately 1 mm, depending on the positron energy [15]. The two generated γ rays are exploited in PET exams. The highlighted range effects are the cause of blur in the images.

1.2.1 SPECT

Single Photon Emission Computed Tomography is the most currently used technique, accounting for about 95% of radiodiagnostic scans in over 40 million pro-

cedures made annually worldwide [16]. The device used in SPECT imaging is called scintillation camera or gamma camera. As can be seen in figure 1.6, a scintillation camera typically consists of a lead collimator, a large area scintillator and an array of photomultiplier tubes (PMTs).

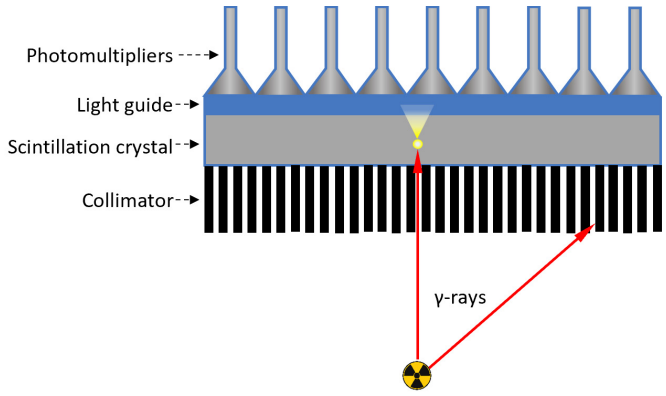

Figure 1.6: Scheme of a gamma camera used for SPECT.

The collimator function is to let pass only the γ rays travelling parallel to the holes and to stop all the others. This allows the reconstruction of the trajectory of the photons and so improves the spatial resolution of the image [17]. The γ rays passing through the collimator encounter the scintillation crystal which converts these high energy photons in visible light. These flashes of light are then converted into electric signals at the exit of the PMTs. The signals coming from an array of PMTs are processed by electronic circuitry to provide information about the energy deposited and the average position of photon interaction into the crystal.

At the end of the signal processing, the gamma camera provides a two-dimensional projection image of the distribution of the radiopharmaceutical inside the patient. To get a three-dimensional SPECT image, several two-dimensional images, acquired at different views around the patient, are combined following proper image reconstruction methods [18]. To accelerate the images acquisition procedure, also because the motion of the patient is a source of medical image degradation, two or three gamma cameras are used at the same time as in the configurations represented in figure 1.7.

The main struggle in the scintillation cameras is between the detection efficiency and the spatial resolution. While the first one improves with higher thicknesses of the crystal (when considering photopeak energies over 100 keV otherwise the camera is almost 100% efficient for every thickness), the second one goes better with lower thicknesses. In the case of thallium doped sodium io-

Figure 1.7: SPECT imaging systems with three and two gamma cameras [19].

dide detectors (NaI(Tl)), that are the scintillators ordinarily used for SPECT, the optimal γ ray energy range is approximately 100÷200 keV [20]. In fact, the most used radioisotope in SPECT procedures, ^{99m}Tc, has a half-life of 6.0072 h and a 140.511 keV γ ray with an intensity of 89% [7]. It is actually incorporated in 28 radiopharmaceuticals already approved by the FDA (Food and Drug Administration, USA) which are mainly devoted to myocardial and cerebral perfusion, renal function and bone scintigraphy diagnosis [16].

In recent years, commercial SPECT systems based on cadmium-zinc-telluride (CZT) have been introduced. They are solid-state semiconductors working at room temperature that directly convert photons in signals collecting the electron-hole pairs created inside the detector [21, 22]. Among the advantages, these detectors promise a high energy and spatial resolutions. This progress, together with advances in image reconstruction methods, contributed to renewing the interest in SPECT imaging for medical applications.

1.2.2 PET

Positron Emission Tomography measures the two annihilation photons produced back-to-back in a β^+ decay. The acquisition of the photons is performed thanks to a typical ring configuration of scintillation detectors, that convert the 511 keV photons in visible or near ultraviolet light, coupled to PMTs that produce an electrical current from slowed down photons, as reported in figure 1.8. The most commonly used scintillators in PET scanning are the Bismuth Germanate Oxide (BGO) crystals and the Lutetium OxyorthoSilicate or Lutetium Yttrium

OxyorthoSilicate (LSO or LYSO) [23]. Their advantage in comparison to the previously used NaI(Tl) is their high density and atomic number Z that guarantee a high efficiency even in small-size crystals. In fact, photons interactions probability increases in this kind of materials resulting in a shorter travel distance.

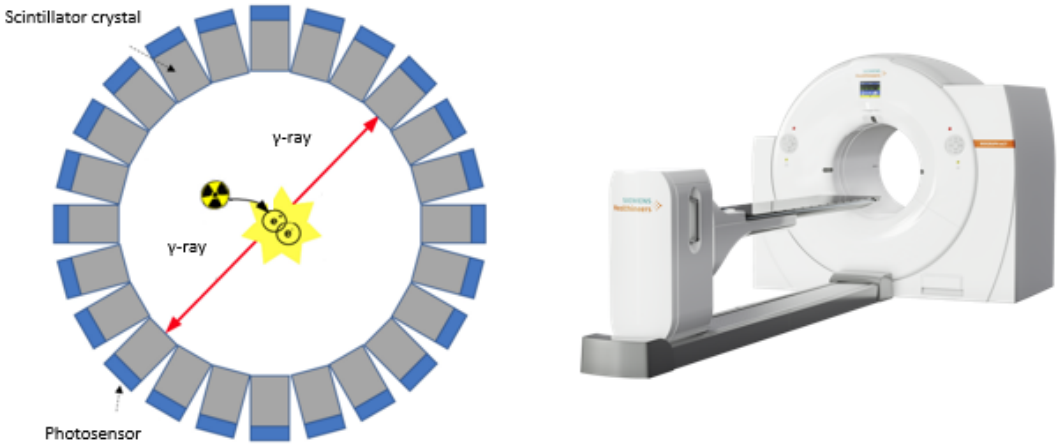

Figure 1.8: Scheme of a PET ring configuration system and a typical PET camera [24].

The most important characteristic of PET imaging is that two photons are expected to be observed at roughly the same time. The not exact coincidence of the two photons' detections can occur, mainly because the annihilation happened closer to a detector than the opposite one or because of the timing resolution of the detector and the electronics. For this reason, a coincidence time window of the order of $3 \div 5$ ns is established [25]. If the two photons are measured within each other's coincidence window they are assumed to be produced in the same annihilation process. The annihilation event is then localized along the line connecting the two detection points, as can be seen in figure 1.8. Thousands of events are reconstructed in this way during a PET examination procedure. From these data the medical image is generated through advanced image reconstructing algorithms.

Given the recent improvement of the timing resolution performance of photosensors, the Time-of-Flight (ToF) technique has been proposed to be introduced in conventional PET to improve the sensitivity and so the image quality. Thanks to this combination, the difference in the arrival time between the two photons coming from the same annihilation process can be used to evaluate the location of the annihilation itself. This can contribute to reduce the background noise in the final PET image [25].

The mostly used radionuclide in PET medical procedures is ^{18}F, with its half-life of 109.77 m and a 249.8 keV β^+ emission with a 96.73% branching mode [7]. Over one million scans are carried out annually and this number is predicted to increase rapidly over next years [26]. Other ordinarily used radionuclides in PET are ^{11}C, ^{15}O and ^{13}N. All of them have in common that are the building blocks of most of the organic molecules in the human body [27]. This means that the radiolabelling process to manufacture the radiopharmaceutical requires a minimal molecular structural modification.

Another PET huge advantage over SPECT is its higher sensitivity derived from the knowledge of the photons' direction. This peculiarity removes the need of collimators, essential in SPECT to restrict possible photon directions, which usually absorb 99% of the γ rays, also determining a higher efficiency and a smaller quantity of radiopharmaceutical administered to the patient since a smaller portion of it is not misspent [27].

On the other hand, the setting up of a PET facility has high capital costs so it is unlikely that this technique will be widely used worldwide soon, especially in less developed countries [26]. SPECT have also lower operating costs due to the employment of more easily available long-lived radionuclides [16].

1.3 Radiopharmaceutical therapy

When a radioactive nucleus is used for radiopharmaceutical therapy (RPT), decay emissions able to cause a lethal cellular damage by depositing the maximum amount of their energy in a short distance are required. These ionizing radiations, in fact, can cause a damage to a cell through a direct or an indirect action, as can be seen in figure 1.9. A direct damage is caused when the radiation directly interacts with the critical targets in the cells starting the chain of processes leading to the biological effect. This scenario is more probable in case of densely ionizing radiations. However, also the indirect action can occur. In this case, the radiation interacts with other parts of the cells. Since a cell is mainly made of water (about 80%), typically free radicals are generated by radiolysis of water and can diffuse and damage the cell DNA.

The exposure to radiation causes a variety of different possible lesions to the DNA:

- Single Strand Break (SSB). Only one of the two strands of the DNA is damaged (figure 1.10 (a)).

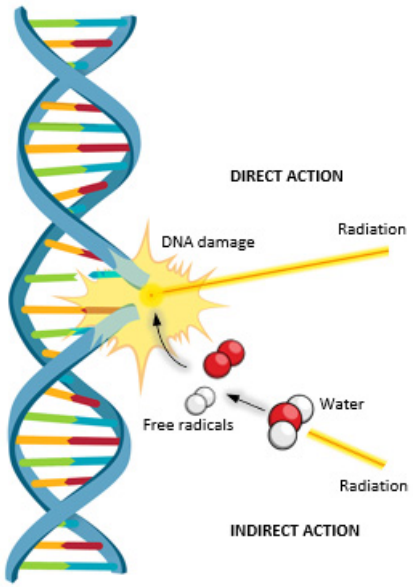

Figure 1.9: Direct and indirect actions of ionizing radiation causing damage to the DNA of a cell.

- Double Strand Break (DSB). Both the strands of the DNA are damaged and the two lesions are near to each other, namely within 4 nm, corresponding to about 10 base pairs [28] (figure 1.10 (b)).
- Base damage. A base undergoes a modification, for example an oxidation (figure 1.10 (c)) or a deamination, which can indirectly lead to a SSB or a DSB.
- Crosslink. It is an interaction between the DNA and a protein (figure 1.10 (d)) but it can also be a DNA-DNA crosslink. In any case, it can also bring to a SSB or a DSB.

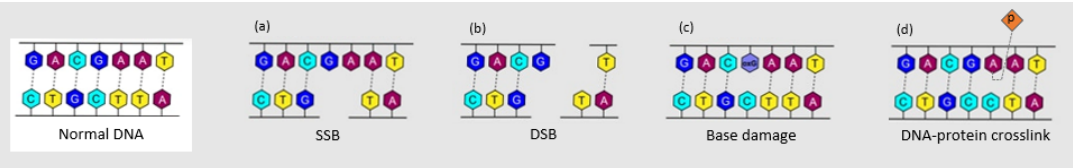

Figure 1.10: Different possible DNA damages caused by radioactive emissions compared to the normal structure of the DNA. (a) Single Strand Break (SSB). (b) Double Strand Break (DSB). (c) damage to a base. (d) crosslink between DNA and a protein.

However, the DNA has some mechanisms to repair the damage when it is detected by the DNA checkpoints. Since each base of the DNA can couple only to its corresponding base, if the lesion leaves one of the two strands undamaged it can be used as a template by the DNA to restore its broken part. This is in

most cases except for the DSB. The DSB repair is a more complex process and is more error-prone, but only one DSB cannot cause the cell carcinogenesis or death [29]. Cell death is more correlated to the number of DSBs occurring in a short distance, namely within one or two helical turns. Furthermore, the DSBs are the rarest: a dose of 1 or 2 Gy generally causes more than 1000 base damages in the DNA of a cell, about 1000 SSBs and only about 40 DSBs [30]. Naturally, radiations able to deposit a high amount of energy per unit length, known as high LET (Linear Energy Transfer) radiations, have a higher capability to generate DSBs in a shorter distance.

β^- particles belong to the category of radioactive emissions used for therapeutic purposes. Their range in tissue is of the order of $1 \div 5$ mm, depending on their end-point energy [31]. Actually, they were involved in the first radiopharmaceutical therapeutic application, the thyroid cancer treatment with the use of ^{131}I previously discussed in section 1.1. β^- particles are emitted in the β^- decay. It takes place when an excess of neutrons is recorded determining the transformation of a neutron to a proton with the emission of an electron and an anti-neutrino.

The widespread availability is one of the reasons of the largely employment of β^- emitters in RPT. Yttrium-90 is a widely used generator-produced radiometal that decays with a half-life of 64.05 h [7] via a pure β^- emission. Its lack of γ emission reduces the radiation dose to patients. Its variety of employments started with ovarian cancer and subsequently focused on haematological cancers, such as lymphoma. Lymphoma cells express a large amount of the protein called CD20 antigen. Against this protein the antibody anti-CD20 is used as agent to treat lymphoma in the classical immunotherapy technique. With the advent of the nuclear medicine, the anti-CD20 antibody started to be radiolabelled with ^{90}Y to combine the therapeutic effect of antibody itself with the benefit of β^- irradiation of tumour cells. Another reason why the β^- emission is the most frequently used type of radiation for RPT is that most of the β^- emitting radionuclides also emit photons with an energy in the range useful for imaging. This is the case of lutetium-177 which has also a half-life (6.6443 d [7]) compatible with the pharmacokinetics of both antibodies and peptides. It can be used to assess tumour uptake and extension but also for treatment, making it a theranostic radionuclide (see section 1.4). To this category belongs also ^{47}Sc, but, differently than others, it is not included in clinical routine procedures yet.

A high LET radiation always important for RPT is the α particle. It is

essentially a helium nucleus emitted when an unstable nucleus changes to another element. Depending on their emission energy, α particles can travel from 50 to 100 μm in tissue, much less than β^- particles [31]. A comparison of the ranges in several materials, including bone, muscle, and water, can be seen in figure 1.11. This is due to the fact that the amount of energy that α particles deposit per unit path length is 400 times greater than that deposited by electrons. This means that they have a higher possibility to cause DNA DSBs. However, radiopharmaceuticals radiolabelled with α emitters show a problematic linked to the recoil effect. This causes the release of part of the daughter nuclei from the radiopharmaceutical and so, it is particularly accentuated in α decay chains. It constitutes an issue because the uncontrolled circulation and deposition of the daughters may damage healthy tissues and induce radiological poisoning [32]. Novel methods to minimize the release of daughter nuclei are currently under development [33, 34].

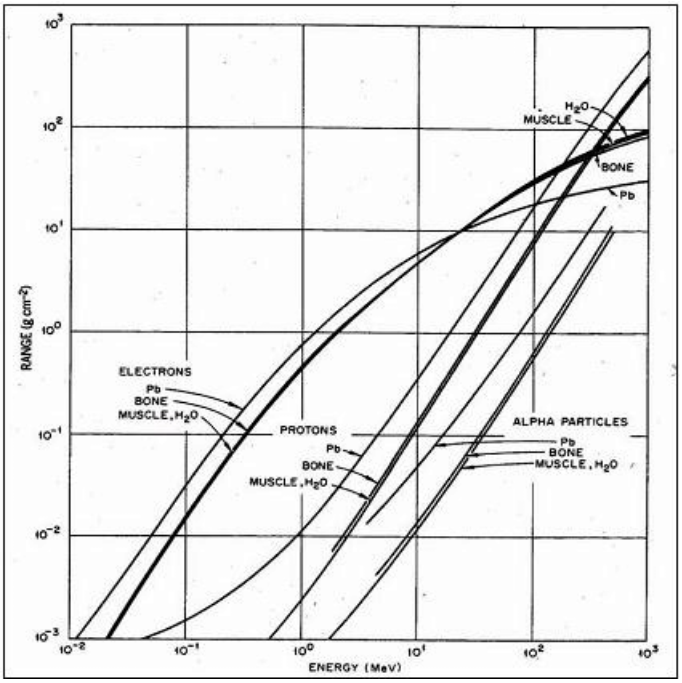

Figure 1.11: Comparison of α, proton, and electron ranges in different elements, including human body components [35]. It can be seen that α particles have always a shorter range.

The first radiopharmaceutical radiolabelled with an α emitter was approved by FDA in 2013. It was Xofigo, a radium-223 dichloride agent by the pharmaceutical company Bayer (Leverkusen, Germany). This important event reinforced the interest in RPT, especially in that with α emitters.

For many decades RPT has been considered as an oncological treatment tech-

nique of last resort. In fact, it was available only in small clinical trials or few institutions which deal with compassionate care in Europe and fewer institutions in the USA and rest of the world. Only recently its efficacy against primary tumours and metastases has been recognised. Thanks also to the FDA approval of many β^- and one α emitters, RPT started to be considered an economically and logistically viable treatment modality. It also presents a lot of advantages in comparison to more conventional therapeutic methods. Among them, RPT shows efficacy with minimal toxicity, responses to radiopharmaceuticals are manifested in $1 \div 5$ injections, side effects in patients are less severe or they are not observed at all, and it is non-invasive. Moreover, the majority of radionuclides used can also emit photons suitable for imaging, allowing the visualization of the biodistribution of the therapeutic agent and so to assess its targeting efficacy [31].

Besides, therapeutic radiopharmaceuticals have also some important non-oncological applications, for example in the field of rheumatoid arthritis and polyarthritis.

1.4 Radiotheranostics

Radiotheranostics is the combination of molecular imaging (mainly PET and SPECT) with RPT. This approach requires the administration of a radionuclide emitting a diagnostic radiation, such as γ or β^+ particles, to assess the tumour localization and extension but also to verify the targeting capability of the radiopharmaceutical before switching to the therapeutic counterpart, constituted by a compound radiolabelled with a β^- or α particles emitter. There are some possible molecule-radionuclide combinations to perform theranostic medical procedures:

- **1 molecule, 1 radioisotope**. The radiopharmaceutical is radiolabelled with a nucleus emitting both a diagnostic and a therapeutic kind of radiation. This is the case, for example, of the already mentioned ^{177}Lu but also of ^{47}Sc;

- **1 molecule, 2 radioisotopes**. The radiopharmaceutical is radiolabelled with two different radioactive isotopes of the same element (real theranostic pair), one with a diagnostic emission and the other with a therapeutic emission. An example is the couple ^{123}I/^{131}I, initially proposed in 1930s and so, constituting the first approach to radiotheranostics [36, 37]. An other example could be the combination of ^{44}Sc/^{47}Sc;

- **1 molecule, 2 radionuclides**. The radiopharmaceutical is radiolabelled with two different radionuclides from two different elements (theranostic pair), one with a radioactive emission for diagnosis and the other for therapy. A widely used pair is $^{68}Ga/^{177}Lu$, as can be seen in figure 1.12;
- **2 molecules, 2 radionuclides**. Two different radiopharmaceuticals are used in combination to perform both diagnosis and treatment. The two vector molecules have to be quite similar so that the biodistribution during diagnostic imaging reflects the biodistribution of the drug during treatment. An example is reported in figure 1.12 for the case of Leukaemia.

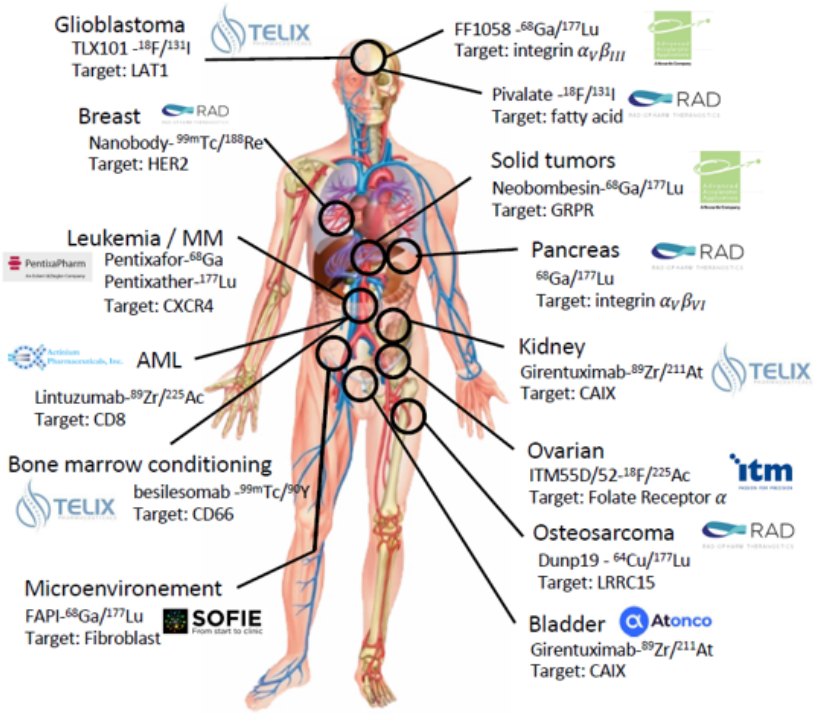

Figure 1.12: Some examples of radionuclide and radiopharmaceutical already available pairs for radiotheranostic applications. Courtesy of Prof. Mickaël Bourgeois.

The main credit of radiotheranostics is to provide a transition from conventional medicine to personalized medicine [38]. The traditional therapeutic approach takes into account just the clinical picture of a patient, prescribing the same kind of treatment to all patients showing the same disease and attempting several other strategies if the previous did not work. However, there are some differences between humans, meaning various responses to therapies. Some differences are more evident, like age, sex, weight, but also genetic characteristics and biological processes play an important role in patients' response to a treatment. The personalized medicine, instead, aims to select patients most likely

responding to a treatment and predict their response. This is possible through theranostics. Diagnosis with a radiopharmaceutical can be used as test, namely companion test, to analyse the pharmacodynamics, other than visualizing the tumour, and eventually to plan a treatment based on the uniqueness of every individual. This concept can be summarized with the statement "the right drug for the right patient at the right time".

The potential of radiotheranostics is still underestimated but something is changing [39]. The approval of many radiopharmaceuticals by FDA and the positive outcomes from many preclinical and clinical trials with innovative radiopharmaceuticals is fostering the scientific and clinical research in this direction. The next step challenge is to establish a reliable production network ensuring a global supply of theranostic agents to support the increasing demand of diagnostic and therapeutic radionuclides.

1.4.1 ^{47}Sc as theranostic radionuclide

^{47}Sc is an emerging theranostic radionuclide not routinely used in nuclear medicine yet, even if it meets all the requirements needed for a nuclear medicine radionuclide [40]. In fact, thanks to its decay emissions, summarized in table 1.1, it can be used for diagnosis, since its γ ray can be detected through SPECT camera, and for therapy of small-medium sized tumours through its β^- particle. Therefore, ^{47}Sc can be labelled in radiopharmaceuticals in 1 molecule-1 radioisotope combination to exploit the SPECT imaging to calibrate the therapeutic dose upon the patient response and to follow the uptake of the radiopharmaceutical.

Table 1.1: Decay characteristics of the theranostic ^{47}Sc. Data are from the NuDat 3.0 database [7].

Isotope	Half-life	γ emission energy (intensity)	β^- emission energy (intensity)
^{47}**Sc**	3.3492 d	159.381 keV (68.3%)	142.6 keV (68.4%) 203.9 keV (31.6%)

Besides, it has the potentiality to be used in a very appealing 1 molecule-2 radioisotopes configuration because there are two β^+ emitter scandium isotopes, namely ^{43}Sc and ^{44g}Sc (see table 1.2), suitable for PET imaging that can constitute a matched theranostic pair together with ^{47}Sc. Between them, ^{43}Sc has the most favourable radiation characteristics (its lower energy γ emission may affect less the patient safety and the PET image quality) but it has less possible

production routes compared to ^{44g}Sc. ^{44g}Sc has also the advantage to have a metastable state with a longer half-life (58.61 h for ^{44m}Sc) for which an in-vivo generator configuration has been evaluated [41].

Table 1.2: Decay characteristics of the β^+ emitters ^{43}Sc and ^{44g}Sc, useful for PET exams in theranostic applications with ^{47}Sc [7].

Isotope	Half-life	γ emission energy (intensity)	β^+ emission energy (intensity)
^{43}**Sc**	3.891 h	372.9 keV (22.5%)	344.46 keV (17.2%) 508.10 keV (70.9%)
^{44g}**Sc**	4.0420 h	1157.022 keV (99.8867%)	630.2 keV (94.278%)

From a chemical point of view, scandium is present in compounds in trivalent state, similarly to lanthanides like lutetium or yttrium. Therefore, ligands developed for lanthanides, widely used in clinic yet, should be available also as chelators of Sc. Some studies on possible chelators have shown that scandium and lanthanides have a comparable performance in terms of stability. These studies, together with radiolabelling studies and preclinical and clinical trials regarding scandium isotopes, are collected in [41]. Most of these experiments have been performed with ^{44g}Sc, which can be considered the scandium isotope in the most advanced stage of development.

^{47}Sc medical application was already proposed many years ago [42] and it was recently remarked in an IAEA Coordinated Research Project dedicated to emerging medical radionuclides [4, 43]. ^{47}Sc shows some advantages with respect to its competitor ^{177}Lu: the product can be more easily recovered from the target after irradiation and it can be produced in other facilities than reactors. The latter is particularly important since some aging reactors ensuring part of the world supply are going to be closed. It can be also noted that there is not a ^{177}Lu ($T_{1/2}$= 6.6443 d [7]) isotope suitable for PET imaging to have a more desirable 1 molecule-2 radioisotopes theranostic pair. In fact, it is commonly used in combination with ^{68}Ga, as can be seen in figure 1.12. Moreover, the shorter but not too short ^{47}Sc half-life ($T_{1/2}$= 3.3492 d) could encourage its use with small molecules that have a relatively faster pharmacokinetic profile. On the other hand, the production route of ^{47}Sc still has to be optimized. Some possible reactions have been individuated by the scientific community and are presented in section 2.6, but the quantity of pure ^{47}Sc produced is not sufficiently high for the routine use of this radionuclide. This is also the reason why ^{47}Sc has been employed in only few preclinical studies up to now [41]. It is the aim of this work

to investigate some possible production routes for ^{47}Sc with proton beams.

Chapter 2

Production of medical radionuclides

Soon after the discovery of radioactivity by Henry Becquerel, Marie Curie and Pierre Curie in 1896, proposals of its applications in life science were not long to coming [44]. Unfortunately, natural occurring radionuclides have usually very long half-lives, which are not useful in nuclear medicine. The half-life is critical for the dose administered to a patient and, when it is too long, the majority of the radiation dose is going to be not necessarily delivered. However, in 1934 the artificial radioactivity was discovered by Irène Curie and Frédéric Joliot [45]. Some radionuclides started to be produced, in very small amount, irradiating some light mass materials with α particles emitted from known sources, such as ^{210}Po [44].

The real revolution in the field of radionuclides production arrived later in '30s, related to two important events. The first one was the realisation, soon after the discovery of the neutron in 1932, of the first neutron source by Enrico Fermi and his collaborators [46, 47]. This kind of source was used for the production of medically interesting radionuclides. This fact fostered the realization of nuclear reactors, after the discovery of the fission in 1938 [48]. Already from 1945 a large number of radionuclides, mainly β^- emitters, were available thanks to nuclear reactors. The second important event occurred in 1932, when Lawrence and Livingston invented a device able to accelerate charged particles like protons, deuterons and later α particles, the cyclotron [49]. Thanks to this invention, few short-lived β^+ emitting radionuclides were already available in the '30s. Unfortunately, the cyclotron technology was quickly mainly employed in fundamental nuclear physics field. Only from 1960s their employment in medical applications resumed [44].

These two technologies, reactor and cyclotron, are effectively the main options

for the medical radionuclides production even today. They have to be considered as complementary and not competitive.

2.1 Nuclear reactors

As of June 2021, there are 223 research nuclear reactors in the world, dislocated in 53 countries [50]. A large portion of them is involved somehow in the radionuclides production but only about 10 medium power research reactors are dedicated to the large-scale production for world supply.

There are several nuclear processes that can be triggered by neutrons interacting with target material.

Fission. The fission's goal is to split a nucleus in two smaller parts. Usually, the neutron is used to make the original nucleus unstable so that it will break. The two new smaller nuclei have statistically unequal mass numbers, ranging from 70 to 160 [51]. In figure 2.1 there is an example of the mass distribution of the produced nuclei: one or both of them can be of medical interest.

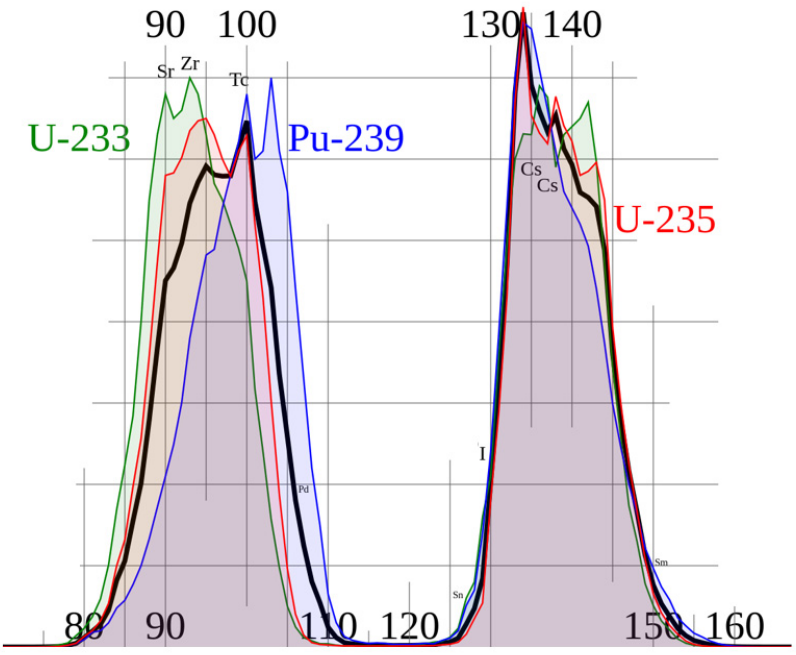

Figure 2.1: Typical mass distributions for some nuclides and for a combination of them (black line). ^{235}U and ^{239}Pu are generally used for the production of medical radionuclides at nuclear reactors via fission reactions. Modified from [52].

Together with fission fragments, usually, also γ rays and 2 to 5 fast neutrons are emitted. Fast neutrons have to be thermalised using moderator materials

with low atomic weight, like water or heavy water. Once moderated, neutrons can be used to activate subsequent fissions or another kind of production reaction.

Charged particles emission. In a nuclear reactor the nuclear reactions (n,p) and, less commonly, (n,α) are used to produce radionuclides. Usually, a certain threshold for the reaction has to be overcome so only the fast part of the neutron spectrum is effective (above 1 MeV). For this reason, such reactions are exploited with light mass nuclei for which the charged particle emission is favoured over neutron emission. For example, ^{14}C and ^{32}P are produced with high specific activity and high yield through (n,p) reaction [44].

Radiative capture. Most neutron activation reactions result in the emission of a γ ray, the (n,γ) reaction. This nuclear process is often characterized by a low specific activity since large part of the target remains unchanged and so the amount of radioactivity per unit mass is small. In fact, usually, the final product is an isotope of the target element so it cannot be chemically separated. To overcome this problem, a possible solution is to exploit this kind of reaction to produce the parent nuclei of a generator system.

2.2 Generator systems

In some cases, the medical radionuclides are not produced directly through nuclear reactions, but are obtained as decay products of their parents, in what are called *generator systems*. Specifically, elution is made periodically to extract the daughter radionuclide from the produced parent exploiting their different chemical properties. Several elution are possible because the parent nucleus replenishes the daughter by decay. The amount of activity available at a given time depends on many factors, such as the initial amount of activity of the parent, the parent half-life, the daughter half-life, and the elution efficiency.

In a generator system, the half-life of the parent must be longer than the half-life of the daughter. Only in this case the parent can continue producing the medical radionuclide of interest. When the parent has a half-life considerably longer than its daughter (more than 100 times) the generator system is defined as in a secular equilibrium. In secular equilibrium the activities of parent and daughter are the same after about 5÷6 half-lives of the daughter since the last elution. When the parent's half-life is slightly longer than the daughter's one (in the order of 10 times) the transient equilibrium occurs. In this case the equilibrium is obtained after about 16 half-lives of the daughter, but it does

not correspond to the maximum activity of the nucleus of interest. Instead, the daughter maximum activity is reached after only 4 half-lives from the previous elution.

In the case in which the parent radioactive nucleus has a shorter half-life than the daughter radionuclide, or the two are comparable, it is not called generator system anymore, but *precursor system*. The elution is made only once when the parent is completely decayed.

The nuclear medicine gold standard, ^{99m}Tc (6.0072 h half-life [7]), is obtained thanks to a generator system. Its parent radionuclide is ^{99}Mo (65.924 h half-life [7]) which is currently produced in nuclear reactors through a (n,γ) reaction on ^{98}Mo targets or in the fission of ^{235}U. After production, ^{99}Mo is loaded onto a column by absorption. From there, a normal saline is used as eluent to remove ^{99m}Tc which is less tightly bound to the alumina column thanks to its different chemical properties. Particular attention should be given to the presence of ^{99}Tc. Both ^{99m}Tc and partially ^{99}Mo decay in ^{99}Tc. This ^{99}Tc will be a competitor of ^{99m}Tc during the radiolabelling of a radiopharmaceutical due to their equal chemistry. To guarantee an adequate labelling efficiency, the elution has to be done frequently so that the quantity of ^{99}Tc is reduced.

Even if in most cases the parent of a generator system is produced in nuclear reactors, sometimes also charged particle accelerators are used, as for the cases of ^{82}Sr/^{82}Rb or ^{44}Ti/^{44}Sc generator systems, for example [53].

2.3 Cyclotrons

There are more than 1500 cyclotron facilities around the world [54]. About 1300 of them, located in 95 countries, are catalogued by IAEA in an interactive map and database [109]. Most of them are partly or fully utilised for medical radionuclides production.

The task of a cyclotron is to provide a high energy and high intensity charged particle beam on the target. Most frequently the beam is made up of protons, but also deuterons, tritons or α particles beams can be provided, even if less frequently. In the cyclotron, the acceleration of the beam is possible inside two electrodes, called Dees for their semi-circular shape, to which a high voltage is applied with a high frequency oscillator. The two Dees are separated by a gap, as can be seen in figure 2.2. When charged particles are introduced from the centre of the cyclotron in the first Dee, the voltage is inverted so that the particles are

rejected from the Dee and attracted by the other Dee across the gap. The circular trajectory is ensured by the perpendicular magnetic field generated between the two magnets. At the end of the trajectory, the particles have reached the desired energy and are directed through the target [51].

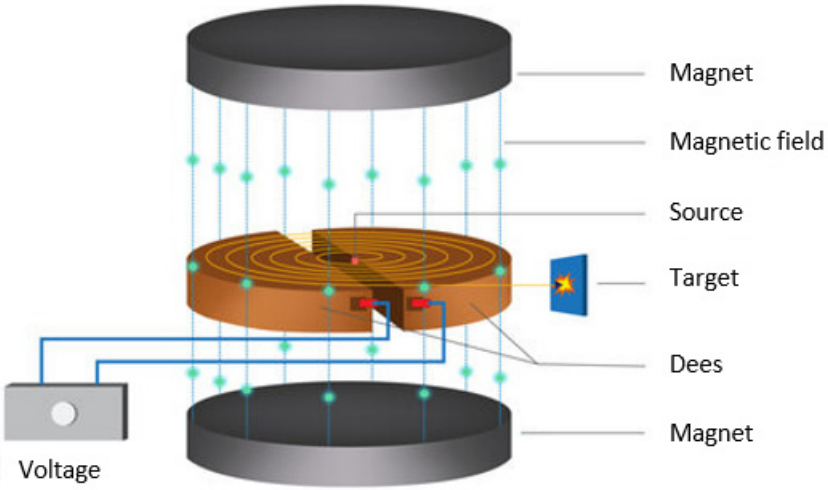

Figure 2.2: Scheme of the inner part of a cyclotron.

Typically, cyclotrons are rated according to their maximum achievable beam energy. An example of this classification, dating back to 2013, is reported in [56]. Most of the available cyclotrons have low maximum energy (E≤20 MeV). They are mainly deployed in hospital environments (medical cyclotrons) for the production of standard PET radionuclides, namely ^{11}C, ^{13}N, ^{15}O and ^{18}F. However, some of them are also dedicated to the research on novel radionuclides, like ^{64}Cu or ^{67}Ga [44]. Higher energy cyclotrons are able to produce many more radionuclides, including SPECT ones, however they are less diffused.

At the moment, there are only 7 facilities owning a cyclotron able to deliver a 70 MeV proton beam, dedicated to medical radioisotopes research and production. As can be noted in figure 2.3, one of them is from Best Cyclotron Systems Inc. (BCSI) and is installed at INFN-LNL.

There are three special considerations to do when using charged particle beams for radionuclides production: the energy loss in the matter, the heat generation and the changing of cross-sections (probability to produce a nucleus) with energy [44].

Energy loss. When traversing a medium, a charged particle losses part of its energy via excitation and ionization of the surrounding material atoms until it comes to rest. This phenomenon depends on the charge and energy of the

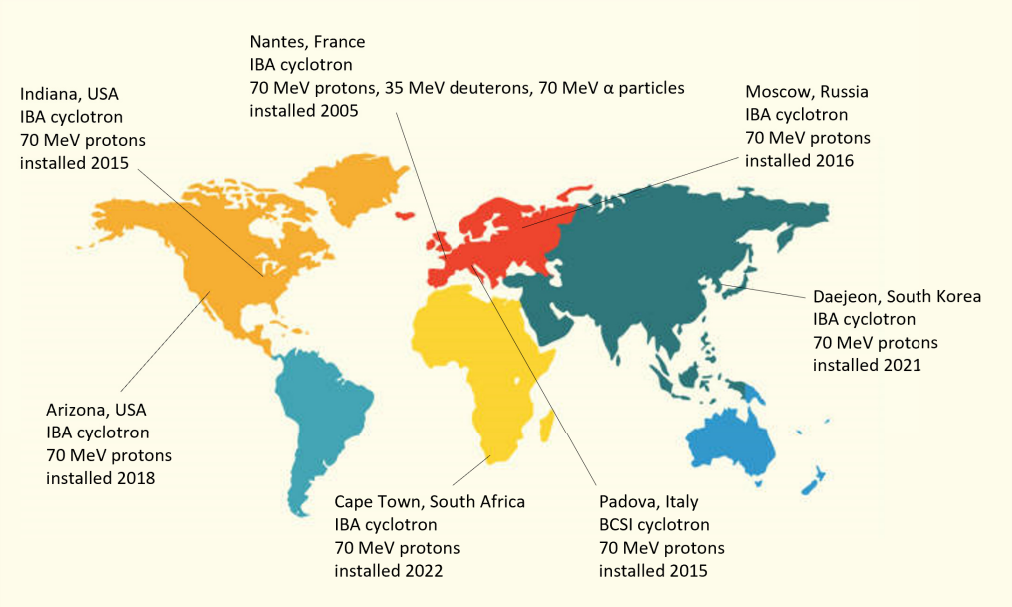

Figure 2.3: The worldwide distribution of the 7 available cyclotrons able to deliver a 70 MeV proton beam (status at 2022).

incident particle: in fact, while the energy of the particle decreases, its stopping power, the average energy dissipated per unit path length by the radiation in the medium, increases. In addition, protons, for example, have a longer average path length in a medium than α particles or heavy ions. However, also the kind of medium material is important: higher is its mass number, higher is the stopping power. Moreover, the energy degradation is higher in solids than in liquids or gases (due to the difference in density and thus in number of nuclei for a given volume). This is an aspect that should be considered and accurately calculated when managing a production process.

Heat generation in target. The particle energy loss translates into heat generation in the medium traversed. This constitutes one of the main limitations in a radionuclide production process, where the beam current can reach up to 1 mA. An efficient cooling system is mandatory in radionuclides production to avoid target damage and break. The liquid (water or other liquid) cooling system is the most commonly used in medical radionuclide production because of its higher heat dissipation efficiency with respect to gaseous ones. However, a combination of the two different cooling systems, gaseous in front and liquid behind the target, is also diffused at cyclotron facilities. Sometimes, the cooling system is also combined with the rotation of the target, to further distribute the beam deposited powder, or the beam wobbling [57].

Changing cross-section. The cross-section of charged particle induced

reactions is really sensitive to the incident energy. The latter changes in the target due to the energy loss in the medium. To evaluate the amount of activity that is going to be produced in a certain target, it is important to know the excitation functions as a function of the incident energy so that the yield can be obtained.

The main advantage of the production at nuclear reactors is that the cross-sections are very high and can be considered constant along the target. So, large samples can be irradiated for a reasonable long time to obtain very high yields. Concerning cyclotrons, instead, the main advantage is the possibility to easily produce β^+ emitting radionuclides of the biological elements like carbon, nitrogen, oxygen and fluorine, widely used for the study of organs functioning.

Since the number of cyclotrons is abundantly higher and some old research reactors are going to be dismissed, most of the worldwide interest is presently focused on the development of cyclotron production. However, improvement in the radionuclides production at reactors is also continuing [44].

2.4 Linear accelerators

Besides the use of nuclear reactors and cyclotrons, in recent years, linacs (linear accelerators) have been proposed as an alternative radionuclides' production method. Differently from cyclotrons, linacs do not bend the particles trajectory in a circular pathway through a magnetic field, but they accelerate the beam in a straight line thanks to a series of cavities to which an alternate voltage is applied. For this reason, linacs are usually less compact instruments than other charged particle accelerators.

Ion linear accelerators can be a valid alternative in case high energy protons, not available in standard medical cyclotrons, are necessary. For example, at the Brookhaven National Laboratory (BNL) the proton beam of up to 200 MeV energy delivered by the linac is used for medical radionuclides production other than for fundamental physics research. Ion linacs have been developed also in compact low-energy version for the production of the PET radionuclide ^{18}F. An example of this is the 7 MeV proton linear accelerator, PULSAR 7, developed by ACCSys (Pleasanton, CA, USA). Their main advantage is that the complex and heavy magnets system is not needed [58].

Probably, the most important application of linacs in medical radionuclides production is related to electron linear accelerators. Actually, electron beams

can also be provided by rhodotrons up to 40 MeV, but they are mainly used in industial applications, and less extensively in radioisotope production, like ^{99}Mo for the ^{99}Mo/^{99m}Tc generator system [59]. 30 MeV or higher energy electrons (at Argonne National Laboratory (ANL), for example, there is a 55 MeV electron linac), accelerated in linacs, are used to produce Bremsstrahlung radiation by interactions with a high Z material, called converter. Hard photons, then, through photonuclear reactions (γ,n) and (γ,p), produce radionuclides of interest with a yield depending on electron beam flux, target size, irradiation time and reaction cross-sections. The database of the latter is currently really poor. Anyway, in the few data available, it shows that generally the (γ,p) reaction is weaker than the (γ,n) one due to its higher cross-section threshold and lower cross-section peaks [44]. On the other hand, (γ,p) reactions lead to high specific activity radionuclides [60].

Different radionuclides have been proposed for a production at the electron linacs both standard and new, such as ^{47}Sc via the ^{48}Ti(γ,p) reaction. Among them there is ^{99}Mo for the ^{99}Mo/^{99m}Tc generator system. Electron beams of 32$\div$42 MeV are optimum for the ^{100}Mo(γ,n)^{99}Mo reaction. An alternative production route is the photofission. In this case, the electrons are directed on a tantalum convertor to generate a fast neutron beam that, after thermalization, is used to generate fission of ^{235}U during which the ^{99}Mo production takes place. At the ANL this production via photonuclear reaction has been demonstrated to be possible with a high yield [60].

2.5 Targetry

When investigating a possible production route of a medical radionuclide, the main goal is that to optimize the production by maximizing the yield while maintaining an acceptable radionuclidic purity (i.e., the ratio of the radioactivity of the radionuclide of interest to the total radioactivity, expressed as a percentage). Those are the two main aspects to counterbalance. Different parameters can be tuned to achieve the purpose. Irradiation time is one of those parameters influencing the yield of the radionuclide of interest and of its contaminants, according to each radionuclide half-life. Beam current can also be adjusted to maximize the production yield, with limits imposed by the machine performance and the cooling system. The beam energy is another factor that can lead to a higher yield, but particular attention has to be paid to possible production of impurities

that can affect the radionuclidic purity.

The other important component that can contribute to the achievement of the scope is the choice of the target. The use of an isotopic enriched material as target material can improve the yield and usually also the radionuclidic purity. Sometimes, only using enriched material a product that meets the criteria for medical applications in humans can be obtained. Given its expensive nature, the use of enriched material should be accompanied by a recycling process, in order to recover the material which can be employed in new targets manufacturing.

In medical radionuclides production, targets in all the three phases - solid, liquid and gas - can be irradiated. The recycling process is usually more efficient for gaseous and, with slightly higher losses, for liquids. The recycling of solid targets, instead, is commonly based on wet chemistry [56]. For this reason, at least few percent of the original material amount are normally lost.

For the production of novel radionuclides, solid targets are often used, most frequently realized with electrodeposition or powder pressing techniques. This kind of targets has a more complex separation chemistry and requires more manual handling, resulting in a higher radiation hazard for personnel. Automatization of the delivery line with pneumatic systems and the use of hot cells are some of the employed expedients. Solid targets are the only ones that can be used in nuclear reactors and in cyclotrons with internal target configuration [44]. Since it is necessary to avoid the melting of the target during irradiation, a proper and efficient cooling system is necessary to absorb the heat generated by the beam in the target. An aspect that can contribute to the reduction of the target heating is related to its position with respect to the beam. In slanted targets configuration, the beam is not perpendicular to the target, but arrives from some small angle. This positioning allows the projection of the beam diameter on wider surface portion having, in this way, a lower heat power per unit area. Moreover, the possibility of a rotating target to spread the heat power deposition over the surface can be considered [56].

Liquid targets are usually metal chambers of few millilitres volume with an entrance window for the beam. For the production of radiometals, a variant has been developed, called solution targets. In this case the target material is dissolved in an aqueous solution in form of salt. This allows to benefit of the advantages of a liquid target (simple handling, fast or non-existent dissolution, easy recycling) in the production of metallic radionuclides that usually requires a solid target. The main disadvantage is the radiolysis happening when irradiating

aqueous solutions. Ions and free radicals of hydrogen, oxygen, and hydroxyl groups are created, which lead to gas evolution in the target that has to be controlled [61]. This aspect is the reason why liquid targets cannot be used in nuclear reactors and in cyclotrons with an internal configuration. Some solutions have been proposed [62], but the technology is not yet mature. On the other hand, targets filled with H_2O and $H_2\,^{18}O$ are widely used for the production of ^{13}N and ^{18}F, respectively, at hospital cyclotrons.

In early '70s, gas targets were actually flow targets: the target older was a relatively long tube through which a stream of target gas was made to flow. The pressure inside the target was adjusted to have enough target nuclei bombarded by the beam. The activated gas was continuously directed to the laboratory area for the chemical processing before the use in patients [44]. This type of target found application especially in the production of short-lived positron emitters radionuclides that led to a rapid development of more efficient targets, able to provide higher amounts of radioactivity. Nowadays, gas targets are pressurised vessels containing few millilitres of a gas target. Sometimes the shape is conic to follow the gradual increase of the beam diameter due to the beam straggling while minimizing the chamber volume to reduce the quantity of enriched gas used [56]. Some gas targets, for example ^{124}Xe targets, have been also used in research reactors contained in some special aluminium capsules [63].

Generally, both liquid and gas targets are simpler recycled and chemically processed, and have more easily automatable operation and processing than solid targets. However, the yield is usually lower than in solid targets due to lower density, in case of gas targets, and boiling and bubble formation, for liquids. For each production route, all the target possibilities should be considered for the final aim of maximizing the production minimizing the radioisotope contaminants production. Sometimes, also the in-house development of an optimized targetry system can be the right choice for an improved production performance.

2.6 ^{47}Sc production routes with reactors and accelerators

Scandium-47 was identified, as also some of its radioisotopes, as promising for nuclear medicine applications already in late 1990s, but it was set aside for about 20 years. Despite its revaluation, its production in huge quantities with a high radionuclidic purity remains a crucial issue. Up to now, some production routes

have been evaluated considering different beam types and target materials [41,64]. They are summarized in table 2.1.

Table 2.1: Main ^{47}Sc production routes investigated both at nuclear reactors and particle accelerators.

Irradiation site	Nuclear reaction
Nuclear reactors	^{47}Ti(n,p)^{47}Sc ^{46}Ca(n,γ)^{47}Ca $\rightarrow$ ^{47}Sc
Charged particle accelerators	^{48}Ti(p,2p)^{47}Sc ^{50}Ti(p,α)^{47}Sc ^{48}Ca(p,2n)^{47}Sc ^{nat}V(p,αp)^{47}Sc ^{44}Ca(α,p)^{47}Sc
Electron linacs	^{48}Ti(γ,p)^{47}Sc ^{48}Ca(γ,n)^{47}Ca$\rightarrow$ ^{47}Sc

The two neutron activation reactions have been deeply investigated and compared in [65]. The production via the ^{47}Ti(n,p)^{47}Sc reaction needs fast neutrons ($E_n > 1$ MeV) which are delivered by a limited number of facilities in the world. This is the first disadvantage concerning such method. The second more influential disadvantage, making this route not feasible, is the high amount of ^{46}Sc always co-produced also using the easily available enriched target material (^{47}Ti natural abundance 7.44%). The presence of ^{46}Sc constitutes a problem since its β^- and high energy γ emissions (see table 2.2) cause an unnecessary radiation dose to patients and complications for the eventual storage in therapy wards. The alternative ^{46}Ca(n,γ)^{47}Ca $\rightarrow$ ^{47}Sc reaction, instead, requires thermal neutrons (E_n about 0.025 eV) that are more widely available in nuclear reactors. In this way, a 'pseudo-generator' system is created (^{47}Ca $T_{1/2}$= 4.536 d vs. ^{47}Sc $T_{1/2}$= 3.3492 d) allowing about three repeated elution of the daughter ^{47}Sc from the parent ^{47}Ca. The radionuclidic purity of the post-elution product is really high, close to 100%. Moreover, when compared to the fast neutron activation production route, a yield considerably higher can be obtained using enriched materials. Unfortunately, the enrichment in ^{46}Ca commercially available reaches a maximum of 30% due to the extremely low natural abundance of ^{46}Ca (0.004%). Thereby, by choosing the optimal irradiation time and waiting for a proper post-irradiation time before starting the separation, it is possible to produce up to about 2 GBq of ^{47}Sc activity by irradiating enriched ^{46}Ca targets [41]. However, a recovery system for the target must be developed to face the production cost through this method.

Table 2.2: Decay characteristics of the main co-produced contaminants ^{46}Sc and ^{48}Sc in the production of ^{47}Sc [7].

Isotope	Half-life	γ emission energy (intensity)	β^- emission mean energy (intensity)
^{46}**Sc**	83.79 d	889.277 keV (99.9840%) 1120.545 keV (99.9870%)	111.8 keV (99.9964%) 580.8 keV (0.0036%)
^{48}**Sc**	43.71 h	175.526 keV (7.47%) 983.526 keV (100%) 1037.522 keV (97.5%) 1312.120 keV (100%)	158.6 keV (9.88%) 227.3 keV (90.12%)

An alternative to the nuclear reactors is the use of the more widespread cyclotrons. The production yield via the ^{48}Ti(p,2p)^{47}Sc reaction was evaluated in the medium to high energy range (48 MeV $<$ E$_p$ $<$150 MeV) using $^{48}TiO_2$ targets [42]. Even though the use of enriched material is relatively cheap, due to the ^{48}Ti high natural abundance (73.72%), the co-production of ^{46}Sc was too high to declare this as a valid production route [41]. The production via the ^{50}Ti(p,α)^{47}Sc nuclear reaction was recently investigated in the energy range below 18 MeV using enriched oxide targets [66]. A saturation yield of 0.2 MBq/μAh with a high radionuclidic purity of 99.5% at the End of Bombardment (EoB) is indicated as the maximum achievable one when using an 800 μm thick target with an incident proton beam of 17.75 MeV. The high cost of the enriched material (natural abundance 5.18%) constitutes a significant limit. The cyclotron production with the ^{48}Ca(p,2n)^{47}Sc reaction was investigated up to 24 MeV [67, 68]. GBq activity levels can be reached considering also the indirect production coming from ^{48}Ca(p,pn)^{47}Ca $\rightarrow$ ^{47}Sc. Unfortunately, the radionuclidic purity is quite low at EoB (85%) with a maximum of about 92% after one ^{47}Sc half-life (80.38 h) due to the abundant production of ^{48}Sc (decay characteristics reported in table 2.2) whose threshold energy is around 3 MeV. Also in this case, the cost of the enriched material is quite prohibitive due to the 0.187% low natural abundance of ^{48}Ca. Another possible production route involves the natural vanadium targets and was deeply investigated at the INFN-LNL, in the context of the PASTA (Production with Accelerator of Sc-47 for Theranostic Applications) project [69, 70]. The advantage deriving from the use of this material is a cheap and almost monoisotopic target since natural abundances are 99.75% of ^{51}V and 0.25% of ^{50}V. This aspect contributes to the high radionuclidic purity achievable, largely above 99% at EoB. The only disadvantage of this method is the low ^{47}Sc yield [41]. The ^{44}Ca(α,p)^{47}Sc yield is always really low as well as the radionuclidic purity. The

only advantage is the small quantity of material needed since the α particles range is short. Deuteron activation has also been proposed for ^{47}Sc production [40], but no studies are available up to now, so it is not discussed here.

In the end, photonuclear reactions are also possible for the production of ^{47}Sc at linacs. The production through the ^{48}Ti(γ,p)^{47}Sc reaction was investigated using natural titanium targets since the ^{48}Ti abundance is naturally high (73.72%) [71, 72]. With an irradiation time of some hours up to few hundreds MBq of ^{47}Sc activity can be produced, but the maximum radionuclidic purity is slightly higher than 90%, which is reached 5.85 days after the EoB, due to the presence of both ^{46}Sc and ^{48}Sc. The use of enriched material, available at a reasonable cost, is suggested to improve the radionuclidic purity even if a significant increase of the yield is not expected. The ^{48}Ca(γ,n)^{47}Ca $\rightarrow$ ^{47}Sc reaction at electron linacs has been considered as an alternative for the 'pseudo-generator' system production [73]. Studies with natural Ca targets, the only published up to now, pointed out a low activity of few tens of MBq/g with the co-production of several Ca-radioisotopes leading to the suggestion of highly enriched targets use. The lack of cross-section values has also been underlined as a main problem for a more precise determination of the yields. In fact, a full knowledge of the cross-section trend is indispensable for the estimation of irradiation parameters and yields evaluations.

2.7 The LARAMED program

The proton-induced production cross-section measurements of ^{47}Sc using different targets, that is the topic of this thesis work, is one of the aims of the LARAMED program at the LNL, one of the four major research centres of the INFN. At the LNL, in 2016, a 70p model cyclotron manufactured by BCSI (BEST Theratronics, Canada) was commissioned in the building dedicated to the SPES (Selective Production of Exotic Species) project, as can be seen in figure 2.4, which is currently under completion.

The SPES project, organized in four stages (α, β, γ and δ), consists in providing high-intensity and high-quality radioactive beams of neutron-rich nuclei to perform basic research in nuclear structure and reaction dynamics (SPES β stage), but also in fostering the multidisciplinary applications research, going from radionuclides production (SPES γ stage) to neutron-based studies through secondary beams (SPES δ stage). This ambitious scientific program relies on the

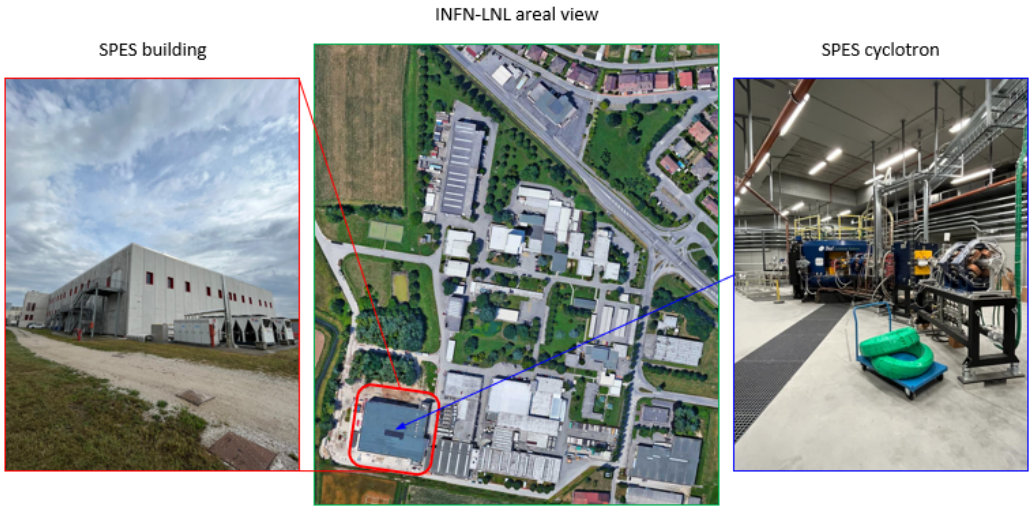

Figure 2.4: Areal view of the INFN-LNL (in the centre) where are indicated the positions of the SPES building (in red, picture on the left) and of the core of the project, the cyclotron (in blue, picture on the right).

dual-beam operational cyclotron able to deliver a proton beam with a tunable energy between 35 and 70 MeV and a maximum current of 750 μA (actually 500 μm are allowed at each port). The acquisition, installation, and commissioning of the high-performance cyclotron, together with the infrastructure completion, constitute the SPES α stage, which is almost concluded.

It is precisely in the γ phase that LARAMED takes place, as well as the ISOLPHARM (ISOL technique for radioPHARMaceuticals) project, with which joins the "Radioisotopi per la Medicina e la Fisica Applicata" LNL research division [5, 74]. While ISOLPHARM is aimed at producing medical radionuclides with the ISOL technique, LARAMED goal is to exploit the proton direct activation to develop and optimize production methods of standard and new emerging medical radionuclides [6, 75, 76]. LARAMED is an award-winning government funded (MIUR) interdisciplinary project granted within the so-called PREMIUM PROJECTS in 2012 and 2016. Its objectives are achieved through several projects, listed in table 2.3, from the LARAMED start in 2012 up to now. Research activities reported in this Ph.D. thesis were performed in the framework of PASTA and REMIX, the two projects dealing with ^{47}Sc possible production routes at proton accelerators. PASTA was a grant project funded by CSN5 (National Scientific Commission 5) of the INFN through the "Bando Giovani Ricercatrici e Ricercatori N.18203" for the years 2017-2018, while REMIX was a three-years project funded by INFN-CSN5 for the years 2021-2023. In these two projects, the proton-induced cross-sections were measured to estimate

the produced activity of ^{47}Sc, but also that of co-produced contaminants since they can contribute to the dose administered to a patient. That dose delivered to a patient was estimated through dosimetric evaluations. In the PASTA project, the proton beam, with an energy up to 70 MeV, was directed on ^{nat}V and enriched ^{48}Ti targets while, in the REMIX project, nuclear reactions on enriched ^{49}Ti and ^{50}Ti were investigated.

The production of the medical promising terbium radioisotopes is also a topic of the REMIX project, but it is not discussed in this thesis.

Table 2.3: Completed and ongoing satellite projects in the LARAMED framework.

Project (activity years)	**Project name and topic**
APOTEMA (2012-2014) TECHN-OSP (2015-2017)	Accelerator-driven Production Of TEchnetium/ Molybdenum for medical Applications TECHNetium for hOSPitals
IAEA CRP (2011-2015)	Coordinated Research Project on "Alternative, non HEU-based ^{99m}Tc/^{99}Mo supply"
COME (2016)	COpper MEasurement (^{67}Cu)
PASTA (2017-2018)	Production with Accelerator of ^{47}Sc for Theranostic Applications
IAEA CRP (2016-2019)	Coordinated Research project on "Radiopharmaceutical Labelled with New Emerging Radionuclides (^{67}Cu, ^{186}Re, ^{47}Sc)"
TERABIO (2016-2019)	High Power Target concepts R&D
E_PLATE (2018-2019)	Electrostatic Powder pLating for Accelerator TargEts
METRICS (2018-2021)	Multimodal pET/mRi Imaging with Cycloytron-produced $^{52/51}$Mn and stable paramagnetic Mn iSotopes
REMIX (2021-2023)	Research on Emerging Medical radIonuclides from the X-sections (^{47}Sc and ^{1xx}Tb)
TOTEM (2021-2022)	magneTron sputtering cyclotrOn TargEt Manufacturing
STarDiS (2023)	Solid Target Dissolution System
CUPRUM_TTD (2023-2025)	^{67,64,61}CU PRoduction and Use in Medicine_Target Technology Development

Part of the SPES building will be dedicated to the LARAMED interdisciplinary activities, as shown in figure 2.5, when the building will be completed.

At the underground floor of the SPES building (on the left in figure 2.5), where the new cyclotron is located, the LARAMED section consists of four bunkers organized in two parts:

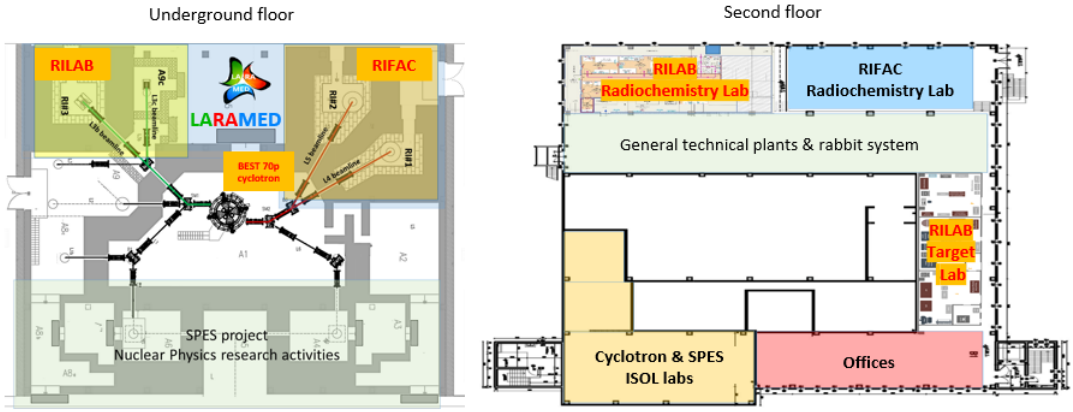

Figure 2.5: Layout of the SPES building. On the left: underground level where the cyclotron is installed and the two parts of LARAMED, RILAB and RIFAC are highlighted. On the right: second floor where LARAMED radiochemistry and targeting laboratories are located.

- **RIFAC (RadioIsotope FACtory)**. It comprises the bunkers RI#1 and RI#2 that will be used, after the establishment of an agreement with a private company, for the massive production of radionuclides then distributed to hospitals.

- **RILAB (RadioIsotopes LABoratory)**. This includes the RI#3 and A9c bunkers which are dedicated to research purposes. In RI#3 limited amounts of novel radionuclides will be produced using high beam currents (300 μA) to be employed in preclinical studies, for example. In A9c low currents (100 nA) will be used for nuclear physics experiments like new medical radionuclides cross-section measurements.

At the second floor (on the right in figure 2.5), the LARAMED area consists of complementary laboratories organized in:

- **RIFAC Laboratory**. It will be used for the preparation of radionuclides and/or radiopharmaceuticals intended for hospitals and clinical centres distribution. This part is not designed yet.

- **RILAB Target Laboratory**. This area will be used for solid targets manufacturing, exploiting both standard and innovative techniques. Targets will be employed in RI#3 and A9c bunkers for irradiation runs dedicated to nuclear physics and radionuclides production research activities.

- **RILAB Radiochemistry Laboratory**. In this laboratory, designed to manage radioactive materials, all the post-irradiation processes take place,

such as targets processing, chemical separation, and purification of the radionuclide of interest, and quality controls of the products.

When the infrastructure will be completed, the RILAB laboratories will be equipped with all the instruments needed for the LARAMED activities. Part of these instruments, like the hot cells for example, have already been purchased and installed in the laboratories [6]. In the meanwhile, the projects are carried on thanks to the multiple LARAMED collaborations with national and international laboratories and hospitals.

Chapter 3

Cross-section measurements at cyclotrons: theory and experiments

The knowledge of the reaction cross-sections is the first fundamental step towards the standardization of the production of novel medical radionuclides. These data are important for [77]:

- determining the ideal energy range for the production of the radionuclide of interest;
- calculating the expected Thick Target Yield (TTY) of the radionuclide to be produced;
- estimating the yields also of the radionuclidic impurities eventually co-produced, given the target thickness and enrichment.

The purity of the final product is the key point when individuating a possible production route. It is critical because the presence of contaminant radionuclides in the final product leads to an additional dose administration which can be potentially dangerous for a patient. It can be responsible of an extra dose also to the operators working in the nuclear medicine hospital section. Moreover, when talking about a radionuclide suitable for imaging, the presence of contaminants can affect the quality of the image. A high purity is obtained maximizing the yield of the desired radionuclide while minimizing that of radioactive impurities. The choice of the projectile energy range can contribute to the achievement of this aim. At low projectile energies the number of open reaction channels is typically low but, with increasing incident energy, several competing reactions set in. The knowledge of the reactions' cross-section trends is essential to determine

in which energy interval a high production probability of the promising medical radionuclide occurs simultaneously to a low production probability of the isotopic contaminants. The use of properly enriched target materials can help to suppress the amount of isotopic impurities, whereas the non-isotopic impurities raise fewer worries since they can be chemically separated.

3.1 The activation method formalism

A typical nuclear reaction is referred to as A(b,c)D, meaning that a target containing nuclei A is bombarded by a beam of particles b causing the production of residual nuclei D and light particles c. The cross-section of a nuclear reaction can be defined as its probability to occur, and it is expressed as a surface. In nuclear physics, its unit is the *barn* (b) even if it is not in the International System of Units. The barn corresponds to the geometrical cross-section of the uranium nucleus, equal to 10^{-28} m^2 [78]. Usually, probabilities are smaller than the geometrical cross-section of a nucleus, so they are in the range of millibarns [78].

Assuming that the beam size is smaller than the target area, the cross-section σ (cm^2) of the reaction is determined by the number of reactions taking place N_{reac} (1/s) [79]:

$$\sigma = \frac{N_{reac}}{N_A \cdot \phi_b} \tag{3.1}$$

where N_A (atoms/cm^2) is the surface density of the target supposed to be homogeneous and ϕ_b (1/s) is the current of the beam of particles b supposed to be constant. Those two parameters are usually known while N_{reac} should be derived. There are two possibilities: the detection of the light particles c or the estimation of the number of produced residual nuclei N_D. The latter is particularly easy when the residual nuclei D are radioactive so that they can be detected thanks to their decay radiation. This is the basis of the *activation method* for cross-section measurements [80]. If the produced radioactive residual nuclei are characterized by a decay constant λ (1/s) and the beam current ϕ_b can be considered constant throughout the whole irradiation time t_i (s), the number of residual nuclei N_D still present at the end of the irradiation is [80]:

$$N_D = N_{reac} \cdot \frac{1 - e^{-\lambda t_i}}{\lambda} = \sigma \cdot N_A \cdot \phi_b \cdot \frac{1 - e^{-\lambda t_i}}{\lambda} \tag{3.2}$$

where the exponential term accounts for the decay of the reaction product

during the irradiation.

If the decay of the residual nuclei is observed for a measuring time t_m (s), the number of decays N_{decays} that can be detected during this time is [79]:

$$N_{decays} = N_D \cdot e^{-\lambda t_c} \cdot (1 - e^{-\lambda t_m}) \tag{3.3}$$

where t_c (s) is the cooling time elapsed between the end of the irradiation and the beginning of the decay radiation measurement.

Combining the equations 3.2 and 3.3, it is possible to obtain the formula to calculate the cross-section for a radionuclide, as a function of the energy, with the activation method:

$$\sigma\,(E) = \frac{N_{decays}}{N_A \cdot \phi_b} \cdot \frac{\lambda}{(1 - e^{-\lambda t_i}) \cdot e^{-\lambda t_c} \cdot (1 - e^{-\lambda t_m})}. \tag{3.4}$$

The activation experiments conducted in this Ph.D. work can be ideally divided into three phases: the experiment preparation, the irradiation of the sample to produce the radionuclide of interest and its contaminants, and the measurement of the decay radiation emitted by the products, which are described in sections 3.2, 3.3 and 3.4 of this chapter, respectively. In the latter phase, γ rays coming from the de-excitation of the produced radioactive nuclei are detected with a HPGe (High Purity Germanium) detector. The peak area C, given by the number of counted γ rays with approximately the same energy, is related to the total number of decays by:

$$C = N_{decays} \cdot \epsilon \cdot I \tag{3.5}$$

where ϵ is the detector efficiency at a given γ energy (*i.e.* the ratio between the number of events in the γ peak and the number of γ rays emitted) and I is the intensity of the specific nuclear transition (*i.e.* the ratio between the number of γ rays emitted and the number of decays occurring). After this consideration, the cross-section formula becomes:

$$\sigma\,(E) = \frac{C}{\epsilon \cdot I \cdot N_A \cdot \phi_b} \cdot \frac{\lambda}{(1 - e^{-\lambda t_i}) \cdot e^{-\lambda t_c} \cdot (1 - e^{-\lambda t_m})} \tag{3.6}$$

where it is important to remember that σ is a quantity depending on the energy of the incident beam.

According to the notation proposed by N. Otuka et al. [81,82], the exponential terms in equation 3.6 can be briefly indicated as a time factor f so that the cross-

section formula can be written as:

$$\sigma_x = \frac{C_x}{\epsilon_x I_x N_x \phi f_x} \tag{3.7}$$

where the subscript x indicates that the quantities are related to the production of the radionuclide of interest or to its detected γ emission characteristics (as in the case of ϵ_x which varies with the γ energy while remaining a detector intrinsic characteristic). As can be noted, the beam flux ϕ is the only quantity completely independent from the nuclear reaction considered. If a direct measurement of ϕ is not possible or reliable, it can be deducted from a reference nuclear reaction used as beam monitor. In this case, the cross-section becomes [81]:

$$\sigma_x = \sigma_r \frac{C_x N_r \epsilon_r I_r f_r}{C_r N_x \epsilon_x I_x f_x} \tag{3.8}$$

where, this time, the subscript r specifies which are the quantities referred to the reference monitor reaction.

If no correlation between the quantities involved in the cross-section formula can be assumed, an uncertainty given by the quadratic sum of the errors can be associated to the equation 3.8 [81]:

$$\left(\frac{\Delta\sigma_x}{\sigma_x}\right)^2 = \sum_q \left(\frac{\Delta q_x}{q_x}\right)^2 + \sum_q \left(\frac{\Delta q_r}{q_r}\right)^2 + \left(\frac{\Delta\sigma_r}{\sigma_r}\right)^2 \tag{3.9}$$

where q represents in general all quantities C, N, ϵ, I and f. The quantity f needs a particular consideration since it includes the decay constant λ which is related to the cross-section through an exponential function and so its uncertainty cannot be incorporated simply in the form of quadratic factor $\left(\frac{\Delta\lambda}{\lambda}\right)^2$. Instead, the following formula should be used [81]:

$$\left(\frac{\Delta f}{f}\right)^2 = s_{f\lambda}^2 \cdot \left(\frac{\Delta\lambda}{\lambda}\right)^2 \tag{3.10}$$

valid both for the investigated and monitor reactions, where

$$s_{f\lambda} = \frac{\lambda}{f} \cdot \frac{\partial f}{\partial \lambda} = \left(\frac{\lambda t_i e^{-\lambda t_i}}{1 - e^{-\lambda t_i}} - \lambda t_c + \frac{\lambda t_m e^{-\lambda t_m}}{1 - e^{-\lambda t_m}} - 1\right) \tag{3.11}$$

and

$$\frac{\Delta\lambda}{\lambda} = \frac{\Delta t_{1/2}}{t_{1/2}} \tag{3.12}$$

while the uncertainties on t_i, t_c and t_m are considered negligible: the order of their relative uncertainty is always 10^{-3} at most.

3.1.1 The $^{44g/m}$Sc case

In some specific cases, a variation of the cross-section formula 3.7 should be considered. This is necessary when the number of counts from two γ peaks have to be combined to obtain the cross-section value of interest, like in the case of ^{44g}Sc. In fact, this radionuclide, encountered during both PASTA and REMIX experiments, can be observed only through its γ line at 1157 keV. However, to this γ line contribute: the decay emission of ^{44g}Sc directly produced during the bombardment, the decay emission of ^{44g}Sc coming from the isomeric transition of its metastable state, and the decay emission of ^{44m}Sc. The decay scheme is reported in figure 3.1.

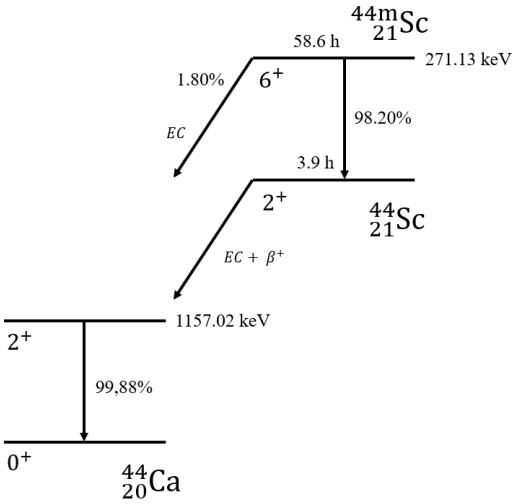

Figure 3.1: Decay scheme of ^{44g}Sc and ^{44m}Sc with the contributions to the 1157 keV γ peak formation.

While the metastable state cross-section can be easily calculated starting from the number of counts of its unshared 271.241 keV γline through the formula 3.8, the ground state production cross-section can be obtained as [81]:

$$\sigma_g = \frac{1}{N\phi I_{1157,g} f_g} \cdot \left[\frac{C_{1157}}{\epsilon_{1157}} - \frac{C_{271} I_{1157,m}}{\epsilon_{271} I_{271}} \right.$$

$$\left. - \frac{C_{271} b_{IT} I_{1157,g}}{\epsilon_{271} I_{271} f_m} \cdot \frac{\lambda_m \lambda_g}{\lambda_m - \lambda_g} \left(\frac{f_g}{\lambda_g} - \frac{f_m}{\lambda_m} \right) \right] \equiv \alpha \left(\beta - \gamma - \delta \right) \tag{3.13}$$

where the term briefly indicated as γ subtract to the general term β the contribution of the metastable state to the peak, while the δ term is for taking into account the ground state originated from the isomeric transition. The quantity b_{IT} is the branching ratio of the isomeric transition.

The uncertainty to associate to this cross-section is slightly more complex due to the higher number of parameters involved and can be expressed as [81]:

$$\left(\frac{\Delta\sigma_g}{\sigma_g}\right)^2 = \sum_k s_k^2 \left(\frac{\Delta x_k}{x_k}\right)^2 \tag{3.14}$$

where the so-called sensitivity coefficients s_k are defined as $s_k = \left(\frac{x_k}{\sigma_g}\right)\left(\frac{\partial\sigma_g}{\partial x_k}\right)$. Assuming that the parameters are independent at a given energy, the sensitivity coefficients specifically become:

$$\begin{aligned}
&\left(\frac{N}{\sigma_g}\right)\left(\frac{\partial\sigma_g}{\partial N}\right) = 1 \\
&\left(\frac{\phi}{\sigma_g}\right)\left(\frac{\partial\sigma_g}{\partial \phi}\right) = 1 \\
&\left(\frac{\epsilon_{1157}}{\sigma_g}\right)\left(\frac{\partial\sigma_g}{\partial \epsilon_{1157}}\right) = -\frac{\alpha\beta}{\sigma_g} \\
&\left(\frac{\epsilon_{271}}{\sigma_g}\right)\left(\frac{\partial\sigma_g}{\partial \epsilon_{271}}\right) = \frac{\alpha(\gamma+\delta)}{\sigma_g} \\
&\left(\frac{C_{1157}}{\sigma_g}\right)\left(\frac{\partial\sigma_g}{\partial C_{1157}}\right) = \frac{\alpha\beta}{\sigma_g} \\
&\left(\frac{C_{271}}{\sigma_g}\right)\left(\frac{\partial\sigma_g}{\partial C_{271}}\right) = -\frac{\alpha(\gamma+\delta)}{\sigma_g} \\
&\left(\frac{I_{1157,g}}{\sigma_g}\right)\left(\frac{\partial\sigma_g}{\partial I_{1157,g}}\right) = -\frac{\alpha(\beta-\gamma)}{\sigma_g} \\
&\left(\frac{I_{1157,m}}{\sigma_g}\right)\left(\frac{\partial\sigma_g}{\partial I_{1157,m}}\right) = -\frac{\alpha\gamma}{\sigma_g} \\
&\left(\frac{I_{271}}{\sigma_g}\right)\left(\frac{\partial\sigma_g}{\partial I_{271}}\right) = \frac{\alpha(\gamma+\delta)}{\sigma_g} \\
&\left(\frac{b_{IT}}{\sigma_g}\right)\left(\frac{\partial\sigma_g}{\partial b_{IT}}\right) = -\frac{\alpha\delta}{\sigma_g}.
\end{aligned} \tag{3.15}$$

This modified cross-section formula, applied to the case of ^{44g}Sc here, can be in principle applied to every other situation where the metastable state, with a longer half-life, contribute to the same γ line emitted also by the ground state. In this thesis work, this type of decay interference was ecountered only between

^{44m}Sc and ^{44g}Sc.

3.1.2 The Thick Target Yield

The obtained cross-section values can be used to calculate the expected TTY. It corresponds to an integration of the measured excitation function over the energy range covered by the thickness of the target [77]:

$$TTY = \frac{N_{Avogadro} \cdot P}{M} \cdot \phi \cdot \left(1 - e^{-\lambda t_i}\right) \int_{E_i}^{E_o} \left(\frac{dE}{d\left(\rho x\right)}\right)^{-1} \sigma\left(E\right) dE \tag{3.16}$$

where P is the level of enrichment of the target, M is the mass number of the target element, E_i and E_o are the energies impinging on and exiting from the target respectively, and $\frac{dE}{d(\rho x)}$ is the stopping power which varies through the material, as it is for the cross-section, because of the change of projectile energy when crossing a thick target.

In equation 3.16, the term $\left(1 - e^{-\lambda t_i}\right)$ is called saturation factor and gives information about the produced fraction of the radionuclide of interest. Its trend as a function of the irradiation time, quantified in radionuclide half-lives, is reported in figure 3.2. It can be seen that with an irradiation time equal to one half-life the saturation factor value is 50%, for two half-lives is 75% and so on.

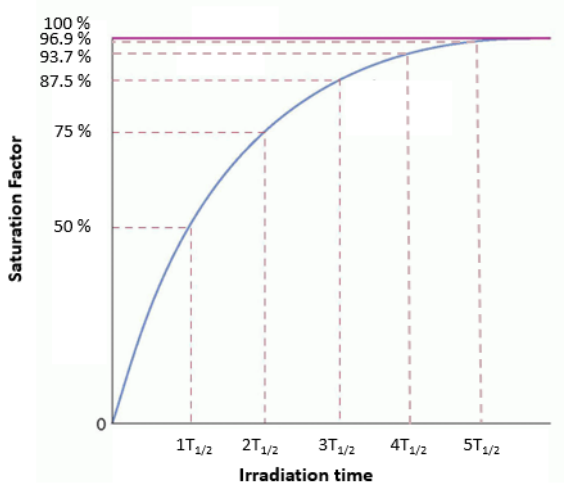

Figure 3.2: Saturation factor as a function of irradiation time expressed in terms of half-lives of the considered radionuclide.

If the radionuclide to be produced has a short half-life, then a saturation factor close to 100% can be easily obtained, that corresponds nearly to an equilibrium between the two competing nuclear processes of production and decay

of the produced radionuclide. However, in most cases, it is not convenient to irradiate up to the saturation point because of the long time required. Therefore, a compromise is needed, and irradiation times are usually no more than three half-lives at which a saturation factor of almost 90% is reached. An example is exactly the case of ^{47}Sc whose half-life is 3.3492 d. So, to reach a saturation factor of almost 100% an irradiation time of at least 400 hours is necessary (more than 16 days) that is not cost-effective if considering the mean price per hour to run a proton beam.

The TTY calculated starting from excitation functions with equation 3.16 represents the maximum yield achievable. In a thick target yield experiment, the yield obtained is usually lower than the theoretical value calculated from cross-section trends. There are several reasons for this fact, such as possible inhomogeneity in the beam, radiation damage effects, loss of product as a result of high-power density effective at the target, etc. Basically, thick target yield experiments are the reflection of the particular irradiation conditions. This is why an accurate knowledge of activation functions and derived TTY is fundamental to define an effective production route.

3.2 Target preparation

The basic element for a cross-section experiment is the target. It should be thin enough to have a constant projectile energy inside it but, at the same time, it should be thick enough to produce considerable activity giving a good statistic.

The PASTA and REMIX projects focused on the use of ^{nat}V and enriched ^{48,49,50}Ti targets to produce the theranostic ^{47}Sc. Natural abundances of vanadium are reported in table 3.1. As can be seen, the amount of ^{50}V present in the natural material composition is really low (0.25%) allowing to consider the ^{nat}V as monoisotopic. For this reason, it was possible to use 20 μm thick metallic ^{nat}V foils, commercially available, to study the ^{nat}V(p,x)^{47}Sc nuclear cross-section. Cross-section measurements performed using this kind of target, aim of the PASTA project, was the topic of my master thesis [83]. The results obtained can also be found in dedicated publications [69, 70, 84, 85].

On the other hand, the natural abundances of titanium are less favourable. Among the isotopes composing ^{nat}Ti, reported in table 3.2, only ^{48}Ti, ^{49}Ti and ^{50}Ti can contribute to the production of ^{47}Sc with proton-induced nuclear reactions.

Table 3.1: Natural vanadium composition and isotopic abundances [7].

^{nat}V isotope	Abundance
^{50}V	0.25%
^{51}V	99.75%

Table 3.2: Natural titanium composition and isotopic abundances [7].

^{nat}Ti isotope	Abundance
^{46}Ti	8.25%
^{47}Ti	7.44%
^{48}Ti	73.72%
^{49}Ti	5.41%
^{50}Ti	5.18%

Several are the cross-section results available in literature regarding the proton-induced production of ^{47}Sc from ^{nat}Ti targets [86]. They assess that a final product pure enough for medical applications cannot be obtained with any beam energy interval. So, to achieve a pure ^{47}Sc production, the use of enriched material is required. Enriched ^{48}Ti, ^{49}Ti or ^{50}Ti metallic foils are not commercially available so enriched metallic powder was purchased for the PASTA and REMIX projects purposes. A specific R&D project, E_PLATE, funded by the INFN CSN5 for the years 2018-2019, was devoted to the manufacture of thin targets with the HIVIPP (HIgh energy VIbration Powders Plating) technique, starting from metallic powders [87, 88]. This method was firstly proposed by I. Sugai in 1997 [89]. An electric field, generated by a high voltage (>2 kV) applied to two opposite electrodes, one placed under the powder and one above, is exploited to cause the powder particles motion towards the electrodes. On each electrode, a 25 μm thick foil of ^{nat}Al is positioned where the accelerated particles are deposited. A quartz cylinder confines the powder and reduces the losses. The setup of the system can be seen in figure 3.3 (a). The deposition process is carried out in a vacuum chamber, as can be seen in figure 3.3 (b). With this technique two samples can be realized simultaneously and with a really low powder losses (<5%), that is an important aspect when working with expensive enriched materials.

The ^{48}Ti powder used in target manufacturing with HIVIPP technique was supplied by Trace Sciences International Inc. (Delaware, USA) with an enrichment of 99.32%. The metallic powders enriched in ^{49}Ti and in ^{50}Ti were purchased from Oak Ridge National Laboratory (Tennessee, USA), the only supplier in the world, with an enrichment of 96.25% and 83.10%, respectively. The percentages of each Ti-isotope contained in the enriched ^{48}Ti, ^{49}Ti and ^{50}Ti powders are

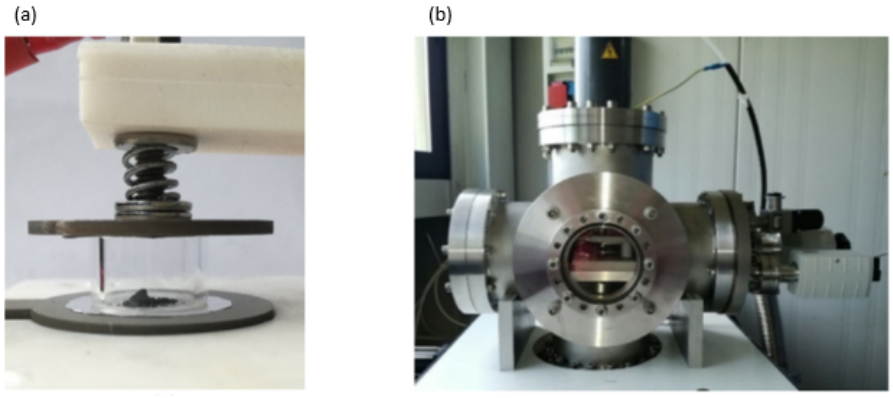

Figure 3.3: Photographs of the HIVIPP experimental system used for thin Ti target manufacturing (a) inserted in a vacuum chamber (b) [87].

reported in table 3.3.

Table 3.3: Ti-isotopes percentages present in the enriched ^{48}Ti, ^{49}Ti and ^{50}Ti powders used for thin targets manufacturing with HIVIPP technique. The values reported are given by the suppliers in the technical data sheets.

Enrichment	^{46}Ti (%)	^{47}Ti (%)	^{48}Ti (%)	^{49}Ti (%)	^{50}Ti (%)
^{48}Ti	0.17	0.21	**99.32**	0.18	0.12
^{49}Ti	0.22	0.22	2.71	**96.25**	0.60
^{50}Ti	1.69	1.29	12.51	1.41	**83.10**

Probably due to isotopic enrichment processes, the metallic powders enriched in ^{49}Ti and ^{50}Ti were in a sponge-like shape with a grains' diameter up to 3 mm, while the HIVIPP method requires a powder grain size less than 5 μm. To reduce the powder size, an additional step was introduced before deposition, consisting in cryomilling process [90]. A ball-milling process allows to diminish the powder size thanks to repeated collisions of the powder particles with the balls and the container walls. The cryogenic temperature is needed to counteract the adhesion of the particles to each other and to the container wall. Pictures of the working cryomill can be seen in figure 3.4. Only the right arm of the machine is a container for the material to be processed, while the left one is just for balance. The cryomilling process was previously optimized with ^{nat}Ti material [90], purchased in a sponge-like form from Alfa Aesar (Massachusetts, USA) with a 99.95% purity. HIVIPP deposition tests with treated ^{nat}Ti powder were also conducted before moving to enriched materials.

The Al foils used as substrate in HIVIPP depositions were provided by Goodfellow Cambridge Ltd. (UK) with a purity of 99%. A high purity is an important requirement to avoid unexpected contaminations in the γ spectra peaks. An

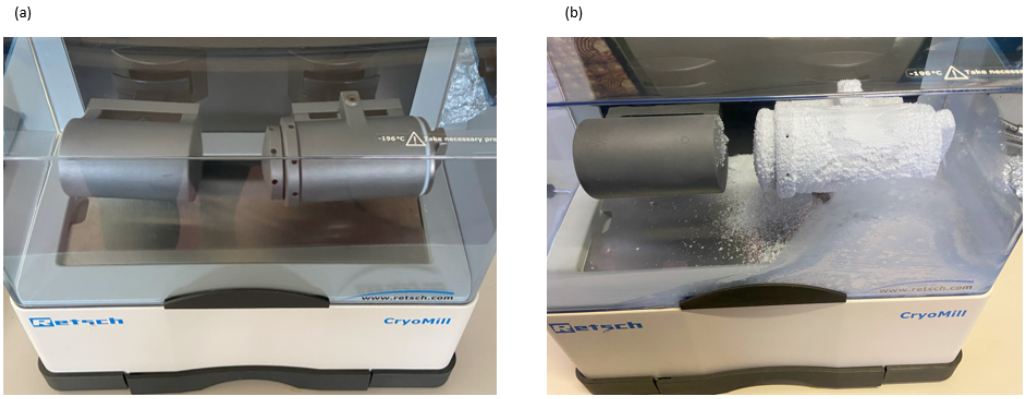

Figure 3.4: Photographs of the cryomill soon after the beginning (a) and after some minutes from the process start (b).

example of the realized targets can be seen in figure 3.5.

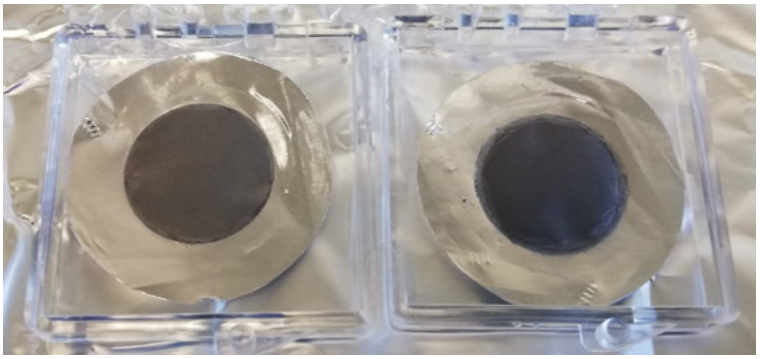

Figure 3.5: Photograph of the HIVIPP deposited powder enriched in ^{50}Ti. On the left, there is the target deposited at the top electrode and, on the right, there is the corresponding bottom deposition.

The amount of material deposited on the Al substrate has to be accurately determined to evaluate the number of atoms per area of the target, a quantity needed for cross-section calculation. Weighting the Al substrate before and after the deposition was not a reliable method because of the presence of oxygen coming from the oxidation of metallic Ti. The amount of deposited Ti atoms, instead, was measured thanks to the Ion Beam Analysis non-destructive method, a very powerful method especially when the chemical element investigated is well separated in the spectrum from the other elements in the target and in the backing. The proton beam of 1 mm diameter at 1.8÷2 MeV and 10÷20 nA delivered by the LNL AN2000 accelerator was used to perform the Elastic Backscattering Spectrometry (EBS) [87]. Typically, in EBS, the energy of the incident particles is so high that the Coulomb barrier of the target nuclei is exceeded and so, the Rutherford's scattering approximation cannot be used [91], as it is in the case of

1.8-2 MeV protons on Al. The non-Rutherford cross-sections used to simulate the EBS spectra with the SimNRA 7.03 software [92] can be found in Ion Beam Analysis Nuclear Data Library (IBANDL) [93], while the stopping power values are from SRIM2003 [94]. An example of the spectra analysis is reported in figure 3.6 (b). The colourful continuous lines represent the elements contained in the samples: the red line is the Ti (^{49}Ti in this case) while the green line is the Al substrate. Some other elements are present in smaller quantities: tungsten (light blue line), iron (yellow line), carbon (brown line), nitrogen (dark green line) and oxygen (pink line) due to surface oxidation of titanium. The combination of all these contributions reproduces the experimental values (black squared points). From the analysis of all the acquired spectra, a Ti thickness ranging between 250 and 900 μg/cm^2 was observed, corresponding to 0.2÷2 μm assuming a bulk density of the material (equal to 4.5 g/cm^3 [95]).

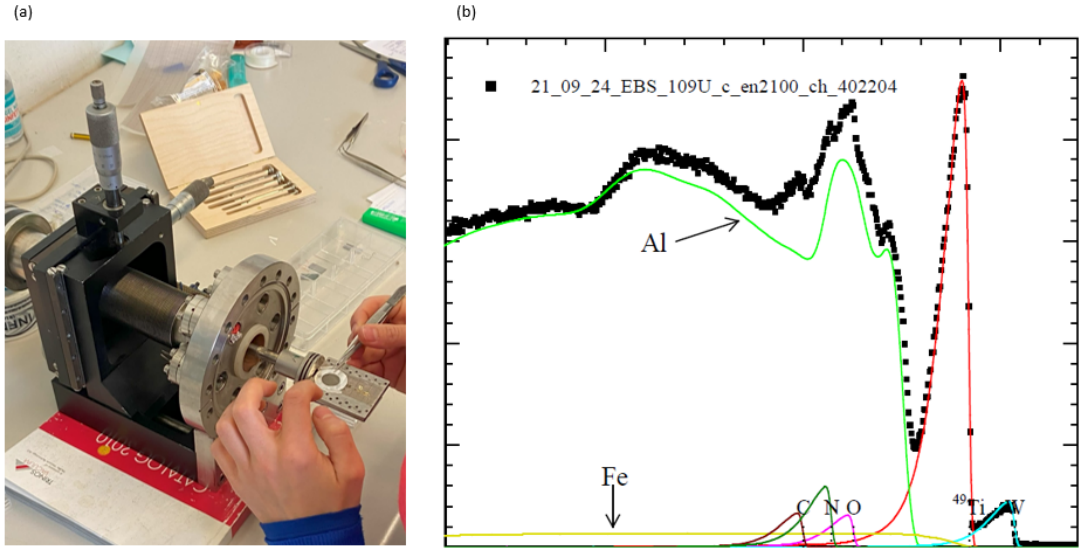

Figure 3.6: (a) Target positioning on the support to be inserted in the beam line. Graph paper, where the target is rested on in the photograph, helps in selecting the three points where the beam is going to hit, and that are going to be analysed. (b) EBS spectrum (counts vs. channel) analysis for a ^{49}Ti enriched target, corresponding to one of the three points. The colourful continuous lines represent the contribution of the elements simulated with the SimNRA software to reproduce the experimental black points.

The Ti deposited quantity evaluated with EBS analysis method is very precise but has the limit to be punctual since it is linked to the small area hit by the proton beam. To overcome this limit, several EBS results obtained for different small areas of the same sample were averaged. A full scan was performed only for few targets, to have a deeper check, while a representative series of three measurements was carried out for all the other samples: one measurement taken approximately in the centre and the other two at 3 mm far from the central one,

moving in opposite directions. A picture of the points selection process, where to perform measurements, can be seen in figure 3.6 (a). This procedure allowed to verify the homogeneity of the samples by comparing the results from the different points. The uniformity of some samples was also assessed by Scanning Electron Microscopy (SEM) analysis [90].

Most of the manufactured samples was irradiated for nuclear cross-section measurements. The non-activated samples were analysed with SEM technique, as can be seen in figure 3.7, by me during my stage[1] at the GIP ARRONAX (Groupement d'Intérêt Public Accélérateur pour la Recherche en Radiochimie et Oncologie à Nantes Atlantique) laboratory [96] (Saint-Herblain, Nantes, France) with the supervision of Dr. Etienne Nigron. The SEM used was the JSM 7100F by JEOL Ltd. (Tokyo, Japan). The acquired images showed that the homogeneity of the samples was unchanged after their transportation from the manufacturing place (LNL) to the irradiation site (GIP ARRONAX). Indeed, in the left side of figure 3.7 a regular pattern in the 100 μm scale can be appreciated. The irregularities in the 10 μm scale can be mainly associated to the oxidation of the Ti surface layer.

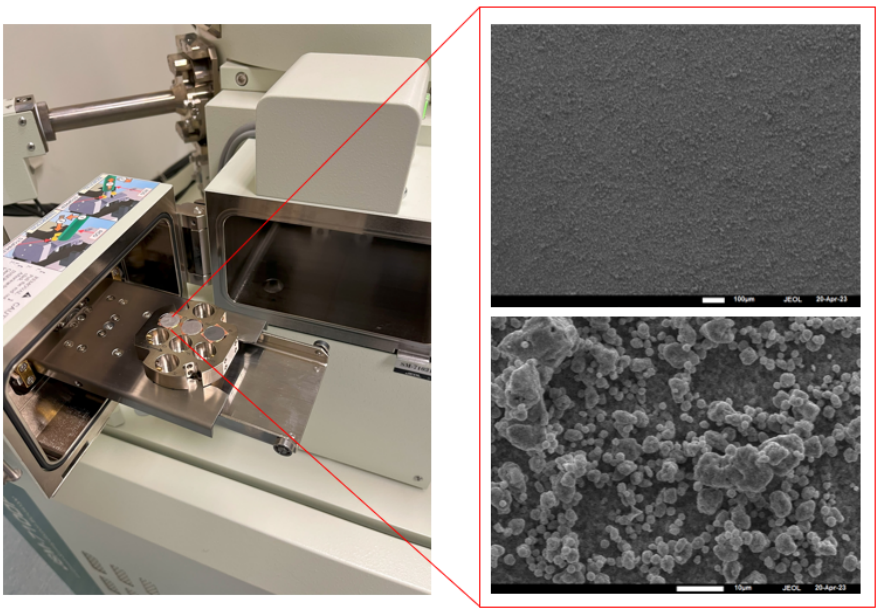

Figure 3.7: SEM analysis of three non-activated samples, one manufactured with ^{48}Ti powder, one with ^{49}Ti and one with ^{50}Ti. On the left, the samples older positioned to be inserted in the tool. On the right, the images acquired at two different scales (100 μm and 10 μm) for the ^{50}Ti sample. The results for the three targets were consistent.

The deposited samples were bombarded mainly at the GIP ARRONAX fa-

[1]Supported by the ERASMUS+ for traineeship program offered in partnership with Padova University.

cility and a small part of them at the Bern university hospital cyclotron laboratory [97].

3.2.1 Stacked-foils targets used at the GIP ARRONAX facility

To fit the target-holder used for the irradiation runs at the GIP ARRONAX facility (see figure 3.10), the depositions were cut to a diameter of 12 mm. The original depositions had a diameter of 14 mm. The cut allows to avoid the outer edge of the depositions that usually present some irregularities. The small difference between the deposition diameter and the cutting size allows to minimize as much as possible the waste of enriched material.

After the cutting process, the enriched Ti targets were arranged according to the so-called stacked-foils technique, consisting in a series of layers of different materials organized in a stack. Stacked-foils is a very useful technique since cross-section values at different energies can be obtained in each irradiation run thanks to the energy loss of the beam particles passing through the stack making the effective energy different at each foil. A typical configuration used during PASTA and REMIX experiments is reported in figure 3.8. The repeated foils sequence is composed by:

- the enriched ^{48}Ti, ^{49}Ti or ^{50}Ti metallic powder deposition on the ^{nat}Al substrate, where the reactions producing the radionuclide of interest and its contaminants take place;
- a 25 μm thick ^{nat}Ni foil in which the monitor reaction ^{nat}Ni(p,x)^{57}Ni occurs. This reaction is suggested as monitor by IAEA in the whole energy range considered [98] and its trend, reported in figure 3.9, can be found in [99];
- a 10 μm thick ^{nat}Al foil used to collect the produced ^{57}Ni nuclei whose kinetic energy allowed their transition from the Ni foil to the subsequent foil (*recoil effect*);
- some thick ^{nat}Al foils (usually 500 μm + 250 μm) used as beam energy degrader.

At the end of the stack, a 100 μm ^{nat}Al foil was inserted to give some strength, especially to thinner layers, and so to avoid their deformation.

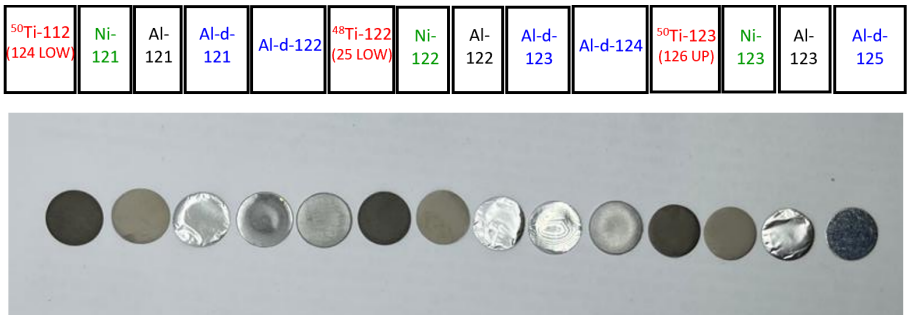

Figure 3.8: Configuration of the stacked-foils target irradiated in the 12^{th} experiment of the REMIX project. The repeated sequence of enriched Ti foil (names in red), ^{nat}Ni monitor foils (names in green), thin ^{nat}Al catcher foils (names in black) and thicker ^{nat}Al degrader foils (names in blue) can be seen.

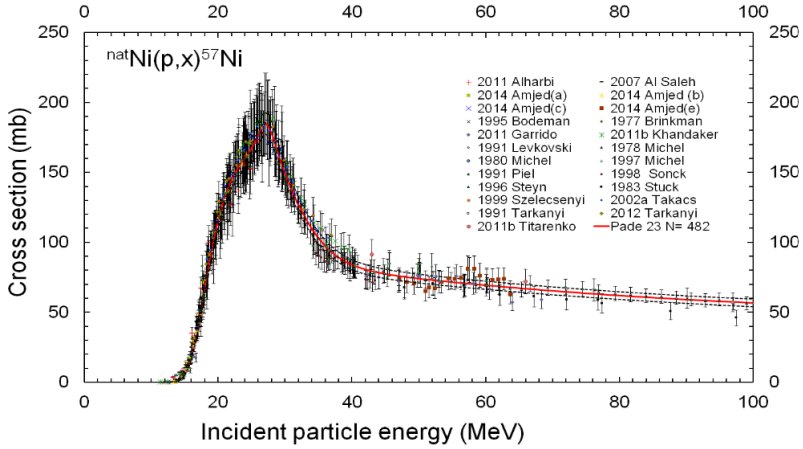

Figure 3.9: IAEA monitor reaction ^{nat}Ni(p,x)^{57}Ni used to derive the beam flux across the stacked-target [99].

As for the depositions, also the ^{nat}Ni and ^{nat}Al metallic foils, purchased from Goodfellow Cambridge Ltd. (UK) with a purity always higher than 99%, were cut to a diameter of 12 mm to fit the target-holder. Even if the metallic foils provider specified the thickness of the foils, it was checked after the cutting process by weighting and deriving the thickness assuming the bulk density. It turned out to be almost unchanged compared to what the provider declared.

The assembly process of the described foils sequence into the target-holder can be seen in figure 3.10. The dimension of the stack, in terms of number of foils, is surely limited by the target-holder structural properties (3 mm max. total thickness allowed), however a high number of foils is never recommended because of the excessive beam energy spread through the target.

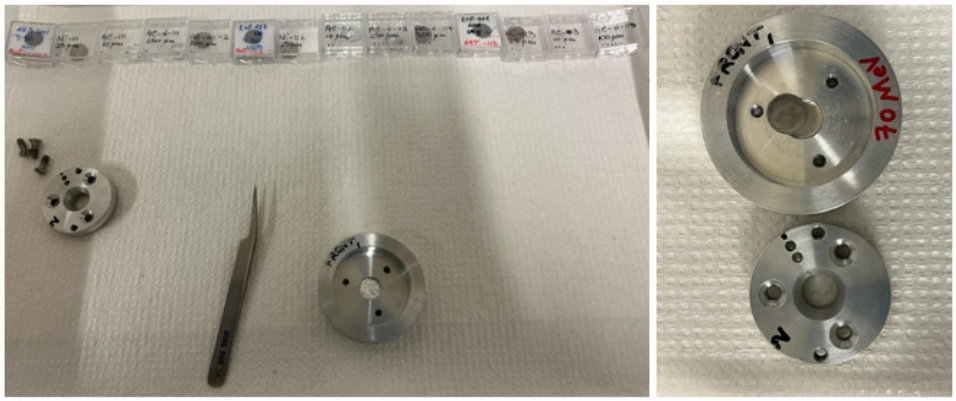

Figure 3.10: Stacked-foils target assembly in the target-holder used in the irradiation runs at the GIP ARRONAX laboratory.

3.2.2 Single target configuration used at the Bern cyclotron laboratory

The energy spread was not a problem in the irradiation runs performed at the Bern laboratory. In this case, each deposition was bombarded separately. The target-holder available was an aluminium capsule with a small cavity to host the target material, as can be seen in figure 3.11. To fit the hole, from one enriched Ti deposition (⌀ 14 mm), five targets with a diameter of 4 mm were cut, inserted in the capsule, and bombarded, one at a time.

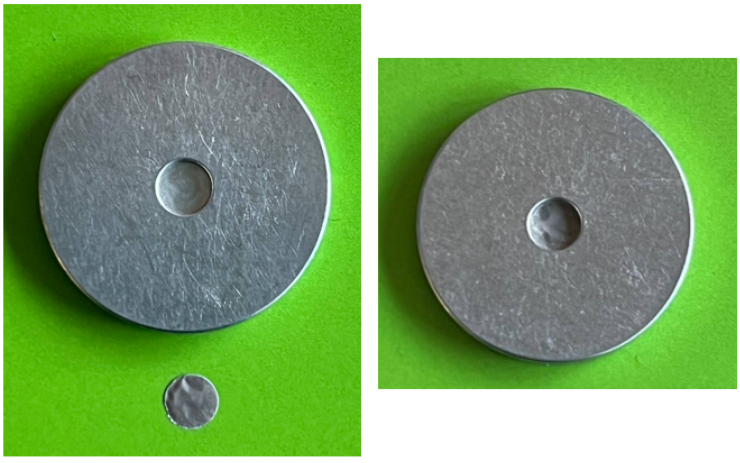

Figure 3.11: Single-foil target before and after its positioning in the target-holder available at the Bern university hospital laboratory.

To avoid eventual loss of material in the target station, the capsule containing the target was enveloped in an aluminium foil.

3.3 Target irradiation

After assembly, targets were bombarded with protons of different energies to induce nuclear reactions producing ^{47}Sc and its contaminants in the enriched Ti material. Since the SPES building at the INFN-LNL is currently under completion, irradiation runs were performed in collaboration with two operating laboratories: the GIP ARRONAX laboratory in Nantes, France, and the Bern university hospital laboratory in Switzerland.

3.3.1 Irradiation runs at the GIP ARRONAX facility

The stacked-foils targets were bombarded with the proton beam delivered by the IBA Cyclone 70 XP, the core of the ARRONAX laboratory (figure 3.12) [96]. The proton beam (negative ions) can be extracted from 30 up to 70 MeV, in dual beam extraction modality, with up to 350 μA current at each port. This cyclotron is able to provide also deuteron and α beams, not used in the context of this thesis work. The experiments for the purposes of the PASTA and REMIX projects were carried out in a bunker dedicated to scientific research, the bunker AX in figure 3.12, and in particular with the beam line A3, the first one in the bunker from the bottom of the figure.

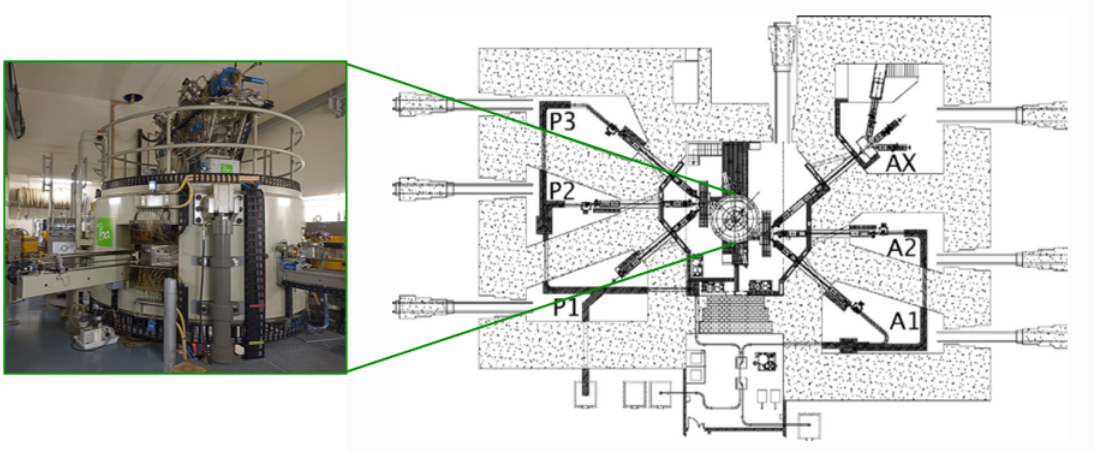

Figure 3.12: Schematic view of GIP ARRONAX facility [96]. In the centre there is the cyclotron that can be seen in the photograph. AX is the bunker at disposal for cross-section measurements.

Before each activation experiment start, the alignment of the movable target station with the beam axis was carried out getting help from a laser system pointing towards the centre of the beam, as can be seen in figure 3.13 (a). All the elements, namely the collimator support, the target mounted on the target

station, and the beam stopper consisting in a cube made of aluminium, were positioned centred along the line individuated by the laser.

Before positioning the collimator and the target, the beam setup, in terms of beam size and energy, was conducted by the cyclotron experts. For this purpose, an alumina layer was positioned in place of the target, in the target station, to visualize the most intense part of the beam. The image of the beam observed from the control room during the setup can be seen in figure 3.13 (b).

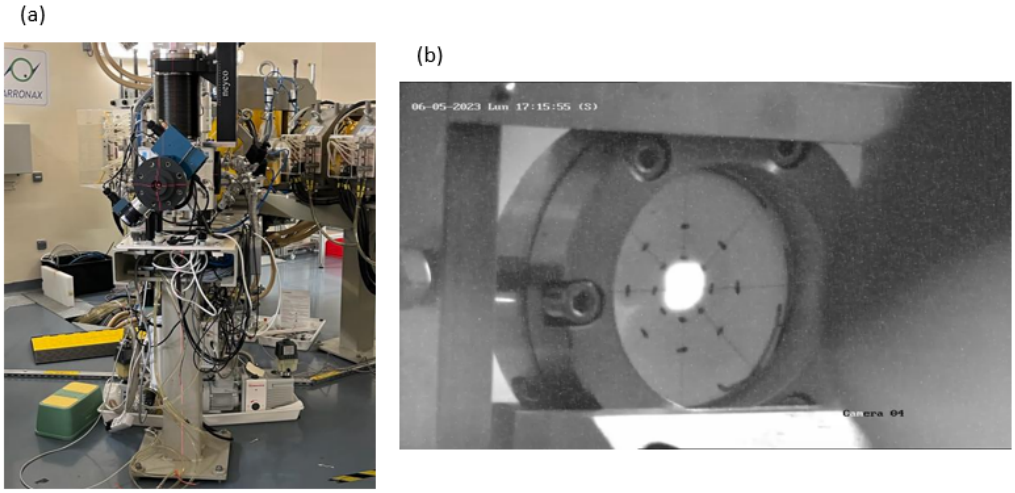

Figure 3.13: (a) Laser system used to align the beam, the collimator, the target and the beam stopper. (b) Photograph of the shaped beam as seen by the cyclotron experts at the end of the setup.

At the end of the beam setup, the alumina was substituted by the stacked-foils target and the graphite collimator (⌀ 9 mm) was inserted to improve the beam shape and simultaneously reduce as much as possible the activation of the target holder.

The entire system was also equipped with a Faraday cup to monitor the beam current during the irradiation and the charge collected. These information were collected on a screen outside the bunker, as can be seen in figure 3.14, together with an image of the target to visually check its mechanical status.

Considering the half-life of ^{47}Sc ($T_{1/2}$=3.3492 d), irradiation time of three half-lives were impractical and, above all, unnecessary for cross-section measurements. Irradiation time in the range 50÷90 minutes allowed to have enough statistics, with a beam current ranging from 80 to 130 nA.

During my Ph.D., I designed and bombarded 12 stacked-foils targets for a total of 37 enriched Ti depositions: 16 depositions of ^{50}Ti, 14 depositions of ^{49}Ti, and 7 depositions of ^{48}Ti enriched powder. 7 more ^{48}Ti depositions were previ-

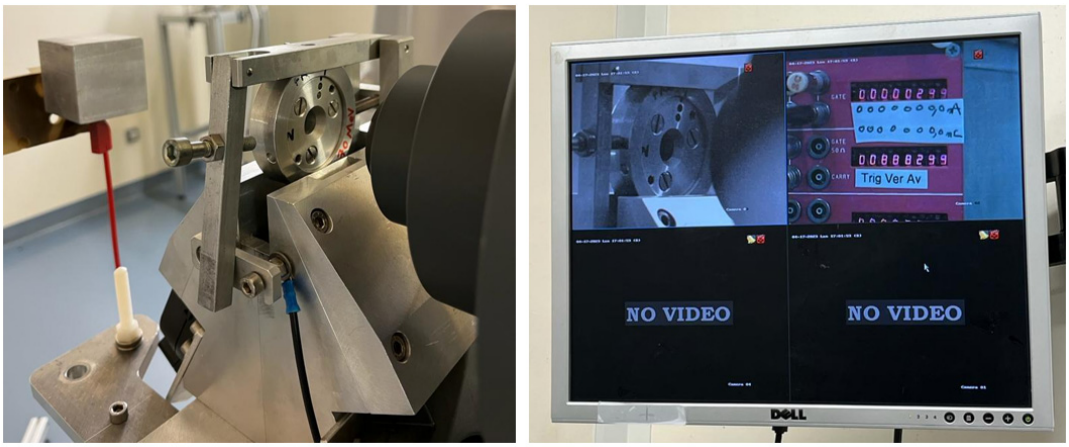

Figure 3.14: Target positioned in the bunker on the left and how it is viewed on the monitor outside the bunker on the right. On the screen there are also the beam characteristics: instantaneous current and collected charge.

ously irradiated by my Ph.D. co-supervisors Dr. Gaia Pupillo and Dr. Liliana Mou, however, I was involved since the data analysis concerning these targets. All the irradiation runs are summarised in table 3.4, where the ones in which I participated to the conception and performance (REMIX experiments) are separated from the ones in which I only worked on data analysis (PASTA experiments). As can be noted, bombardment of ^{48}Ti samples, that should be concluded with the end of the PASTA project, started again during the REMIX project. This is due to the composition of the ^{50}Ti enriched powder, that can be seen in table 3.3. In fact, a high amount of ^{48}Ti (12.51%) is contained in the ^{50}Ti enriched powder, and a smaller quantity (2.71%) also in the ^{49}Ti enriched powder. Cross-section measurements at high energies, up to 70 MeV, have been performed with ^{49}Ti and ^{50}Ti depositions, while during the PASTA project only the energy range up to 40 MeV was covered with the ^{48}Ti cross-section trends. For this reason, some enriched ^{48}Ti depositions were inserted again in stacked-foils targets bombarded at high energies for the REMIX project. In this way, corrections for the contribution of ^{48}Ti in ^{49}Ti and ^{50}Ti cross-sections were possible during data analysis. Actually, corrections to the ^{50}Ti cross-sections for the contribution due to the presence of ^{49}Ti in the ^{50}Ti enriched powder were also made.

The basic idea of the correction for the presence of isotopic contaminants in the enriched target is to consider the calculated cross-section as the result of all the contributions:

Table 3.4: Parameters used in the irradiation runs at the ARRONAX facility. The experiments designed and performed by me (REMIX ones) are separated from the ones whose I only performed data analysis (PASTA).

Irradiation run name and date (dd/mm/yyyy)	Proton energy (MeV)	Irradiation time (min)	Mean current (nA)	Number and type of Ti targets
PASTA-4 10/10/2017	34.0	90	120	n°1 ^{48}Ti dep.
PASTA-5 22/11/2017	40.0	50	130	n°4 ^{48}Ti dep.
PASTA-6 17/04/2018	34.0	90	100	n°2 ^{48}Ti dep.
REMIX-1 26/10/2021	70.0	60	110	n°3 ^{49}Ti dep.
REMIX-2 26/10/2021	40.0	90	110	n°3 ^{49}Ti dep.
REMIX-3 01/03/2022	50.0	90	110	n°3 ^{49}Ti dep.
REMIX-4 01/03/2022	58.0	75	110	n°3 ^{49}Ti dep.
REMIX-5 07/06/2022	45.0	90	100	n°3 ^{50}Ti dep.
REMIX-6 07/06/2022	54.0	60	125	n°3 ^{50}Ti dep.
REMIX-7 21/02/2023	70.0	60	80	n°1 ^{48}Ti dep. n°2 ^{50}Ti dep.
REMIX-8 21/02/2023	56.0	60	100	n°2 ^{48}Ti dep. n°1 ^{50}Ti dep.
REMIX-9 17/04/2023	45.0	60	120	n°2 ^{48}Ti dep. n°1 ^{49}Ti dep.
REMIX-10 23/05/2023	30.7	60	120	n°1 ^{48}Ti dep. n°3 ^{50}Ti dep.
REMIX-11 05/06/2023	36.7	60	115	n°1 ^{49}Ti dep. n°2 ^{50}Ti dep.
REMIX-12 23/05/2023	62.0	60	120	n°1 ^{48}Ti dep. n°2 ^{50}Ti dep.

$$\sigma\left({}^{enr}Ti(p,x)\right) = \eta_{50}\cdot\sigma\left({}^{50}Ti(p,x)\right) + \eta_{49}\cdot\sigma\left({}^{49}Ti(p,x)\right) + \eta_{48}\cdot\sigma\left({}^{48}Ti(p,x)\right)$$

$$+ \eta_{47}\cdot\sigma\left({}^{47}Ti(p,x)\right) + \eta_{46}\cdot\sigma\left({}^{46}Ti(p,x)\right) \tag{3.17}$$

where η_i is the fraction of the i-th isotope contained in the target. For fractions lower than 1% the contribution of the corresponding isotope was considered negligible. Sometimes, also fractions slightly higher than 1% resulted not particularly relevant, like the presence of 2.71% of ^{48}Ti in enriched ^{49}Ti targets for the ^{47}Sc cross-section since the variation was inside the uncertainty. In other cases, however, they are significant, like the presence of ^{46}Ti in enriched ^{50}Ti for the ^{44}Sc cross-section trends. This impact on the results will be described in detail

in chapter 4 where the obtained nuclear cross-sections will be presented.

At the end of each irradiation run, a proper cooling time to decrease the activity in the bunker was waited. Then the stacked-foils target was recovered and dismounted: the thicker Al foils used as beam energy degraders and target support were collected in a lead shield; the thinner ^{nat}Al, ^{nat}Ni and enriched Ti foils were measured with the detectors described in section 3.4.

3.3.2 Irradiation runs at the Bern cyclotron laboratory

The single foil configuration was used in the irradiation runs performed at the Bern medical cyclotron laboratory, which features the IBA Cyclone 18/18 high current cyclotron able to provide an 18 MeV proton beam with a current ranging from few pA up to 150 μA. The laboratory is complemented by two bunkers: one for PET tracer production and the other one dedicated to multidisciplinary research. The second bunker, that can be seen in figure 3.15 (a), was used for the REMIX experiments, where the proton beam is delivered by means of a 6 m long Beam Transfer Line (BTL) characterized by an extracted beam energy of 18.3 $\pm$ 0.3 MeV. To have a different beam energy impinging on the target, aluminium discs were used, positioned in front of the target, to decrease the energy. The energy value impinging on the target was then deduced through SRIM-2013 simulations [100].

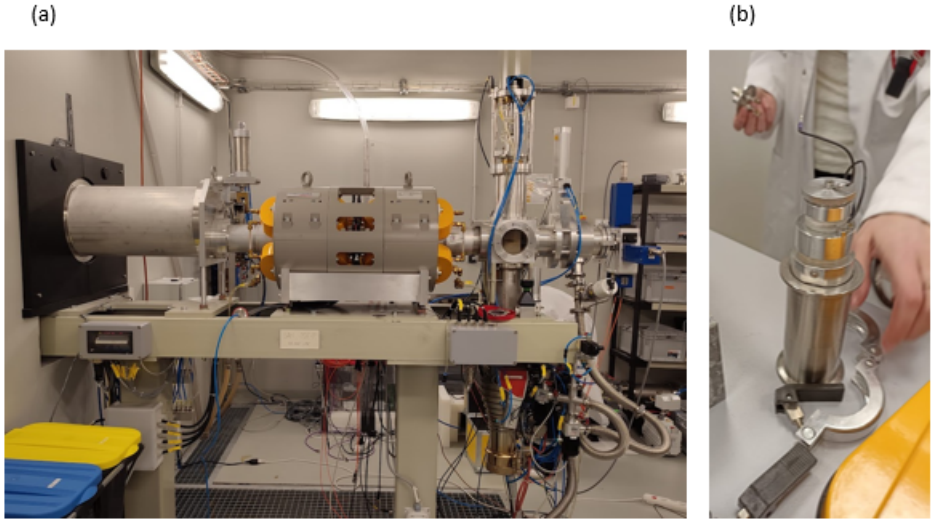

Figure 3.15: (a) The end of the BTL used at the Bern cyclotron hospital for research activities. (b) Target station in which the capsule with the target inside is inserted. This part is then hooked to the end of the BTL.

The BTL was equipped with specific detectors, developed by the research

group working in the laboratory, able to measure the beam position and its shape on-line [100]. In this way, the flatness of the proton surface density was controlled during the whole experiment. The main advantage of this technique is that the uniformity in thickness of the targets is not required. This was favourable also for the deposition realized at the INFN-LNL since its uniformity was tested in three points and then cut in five targets, thus each target uniformity was not evaluated. Moreover, a collimator of 6 mm diameter selected only the central part of the beam and the diameter of the targets was 4 mm. This constituted a further assurance of the beam flatness.

Capsule containing the target was inserted in an ad hoc target station developed always by the Bern laboratory group, that can be seen in figure 3.15 (b). This target station allows to measure the current on the target in real time. An electron suppressing ring is integrated in the target station to reject secondary electrons, assuring a realistic measurement of the beam current [101]. This is the reason why the use of a monitor foil was not necessary.

At the Bern cyclotron five ^{50}Ti targets were activated, to measure the promising low energy region of the cross-section trend. In fact, for energies up to 18.3 MeV, ^{47}Sc should be almost the only isotope produced, given by the ^{50}Ti(p,α)^{47}Sc reaction which has a threshold energy of about 2.3 MeV [102]. Only when reaching approximately 18 MeV, considerable amount of the main contaminant ^{46}Sc begins to be produced via the ^{50}Ti(p,α+n)^{46}Sc reaction ($E_{th} \cong 13.1$ MeV [102]). However, the significant ^{48}Ti presence in the enriched ^{50}Ti powder should not be forgotten. The threshold for the ^{48}Ti(p,2p)^{47}Sc reaction is $E_{th} \cong 11.7$ MeV [102]. Consequently, also one ^{48}Ti deposition was bombarded to correct the ^{50}Ti cross-section value corresponding to the higher proton energy used (18.2 MeV). The reasoning for the correction was similar to the one expressed in the formula 3.17 except that this time, since we were considering the ^{47}Sc production in the low energy region, only ^{48}Ti had an open channel for the reaction and not ^{49}Ti. Thus, the formula for the cross-section correction becomes:

$$\sigma\left({}^{enr50}Ti(p,x)^{47}Sc\right) = \eta_{50} \cdot \sigma\left({}^{50}Ti(p,\alpha)^{47}Sc\right) + \eta_{48} \cdot \sigma\left({}^{48}Ti(p,2p)^{47}Sc\right) \quad (3.18)$$

and, similarly, for the ^{46}Sc production at the higher energy value considered in the experimental runs, 18.2 MeV. However, in this case, the contribution came only from the ^{49}Ti contained in the target:

$$\sigma\left({}^{enr50}Ti(p,x)^{46}Sc\right) = \eta_{50}\cdot\sigma\left({}^{50}Ti(p,\alpha n)^{46}Sc\right) + \eta_{49}\cdot\sigma\left({}^{49}Ti(p,\alpha)^{46}Sc\right) \quad (3.19)$$

where the value used for $\sigma\left({}^{49}Ti(p,\alpha)^{46}Sc\right)$ was the one reported by Dellepiane *et al.* [66].

A resume of the experiments carried out at the Bern university hospital laboratory is reported in table 3.5, where also irradiation parameters are specified.

Table 3.5: Irradiation parameters used in the irradiation runs at the Bern cyclotron laboratory in the context of the REMIX project.

Irradiation run name and date (dd/mm/yyyy)	Proton energy (MeV)	Irradiation time (min)	Mean current (nA)	Enrichment of the irradiated target
REMIX-B48 14/02/2023	18.2	53	30	^{48}Ti
REMIX-B5 14/02/2023	18.2	50	32	^{50}Ti
REMIX-B2 14/02/2023	12.3	60	34	^{50}Ti
REMIX-B3 15/02/2023	14.5	52	35	^{50}Ti
REMIX-B4 15/02/2023	16.0	42	40	^{50}Ti
REMIX-B1 15/02/2023	10.0	57	38	^{50}Ti

The uncertainty associated to the proton energy impinging on the target was always 0.4 MeV.

The study of the ^{50}Ti(p,α)^{47}Sc reaction cross-section was already faced by the research group operating at the Bern laboratory [66]. However, their results showed a certain discrepancy with the only other data set available in literature [103], as can be seen in figure 3.16. A new set of cross-section values seemed to be the opportunity to validate one group result or the other or neither of them. Anyway, we repeated the measurements using a different kind of target. In fact, Dellepiane and her colleagues used an oxide powder, TiO_2, directly deposited in the capsule used for the irradiation runs by evaporation. In the experiments described in this thesis, on the other hand, it was used metallic powder deposited on Al supports through the HIVIPP technique and characterized by EBS analysis. Also, the enrichment of the two powders was different: the characteristics of the one used by the Bern group can be found in [66].

Given the considerably lower quantity of material used in our kind of target, some preliminary activation tests were made using ^{nat}Ti depositions. In this way, we ascertained that irradiation runs of about 40÷60 minutes with a current in the range 30÷40 nA were suitable to activate the target and have a reasonable

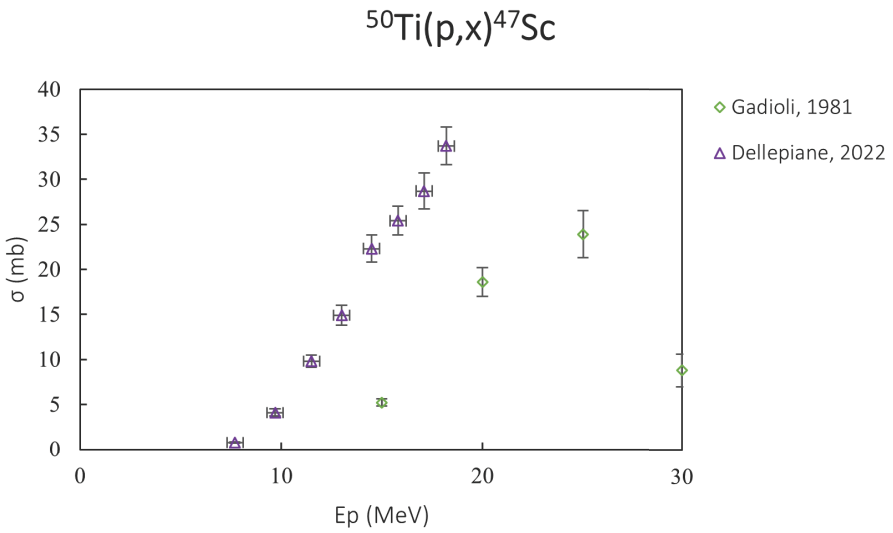

Figure 3.16: Graph showing the discrepancy between the results obtained by Dellepiane et al. (2022) and the previous literature data by Gadioli et al. (1981).

statistic.

Also in this case, at the end of each irradiation run a proper cooling time was waited, allowing the decrease of the activity in the bunker before collecting the bombarded target.

3.4 Detection of the produced nuclei

The radioactive products of the nuclear reactions occurred in the target almost always undergo a β decay, with very few exceptions. The β decay, independently of the type (β^-, β^+ or electron capture), usually leaves the daughter nucleus in an excited state. The de-excitation can cause a γ emission.

The detection of the γ rays coming from the de-excitation of the daughter nuclei is undeniably advantageous with respect to detecting the β particle emitted in the decay of the parent nuclei, due to the lower self-absorption of γ rays in the target and to the well-defined transition energy in opposition to the continuous β spectrum. Therefore, γ detection is preferred in the overwhelming majority of cases. HPGe detectors are the instruments usually used to detect γ rays due to their excellent energy resolution that allows to discriminate different radionuclides γ peaks in the target spectra [80]. Indeed, n-type HPGe detectors were used in the Ph.D. activities described in this thesis. The advantage of the n-type detectors over the p-type ones is the higher efficiency in the low energy range of the emitted γ rays.

3.4.1 γ spectroscopy at the GIP ARRONAX facility

In each irradiation run, soon after the recovery and dismounting of the stacked-foils target, a first short γ acquisition of each activated enriched Ti sample was performed (about 15÷30 min long). In this way, the products with a short half-life could be measured. Hereafter, during the day, longer γ spectrometry measurements (1÷3 h) for each enriched Ti target were repeated each day after the EoB, up to five days after the EoB, to follow the decay of the produced radionuclides and hence to check for the presence of eventual interferences in the γ peaks or of decay chains. The latter was the case of the mentioned ^{44m}Sc decaying in ^{44g}Sc, which is simultaneously also directly produced. On the other hand, an interference has been encountered in the 984 keV and 1312 keV γ peaks which are both emitted by ^{48}Sc and by ^{48}V, two often produced contaminants, as can be seen from table 3.6. Fortunately, ^{48}Sc has also a highly intense γ emission at 1038 keV with which the ^{48}Sc contribution to the 984 keV and 1312 keV γ lines was removed and the ^{48}V activity could be derived. The long-lived ^{48}V ($T_{1/2}$= 15.974 d) was also measured free from any interference (^{48}Sc $T_{1/2}$= 43.71 h) about 1÷2.5 month after the EoB in a further really long acquisition (usually 24÷72 h). In these later γ spectra also ^{46}Sc was detected ($T_{1/2}$= 83.79 d). The presence of low activity products was checked out with long measurements (8÷12 h) performed in the nights following the EoB. ^{nat}Ni and thin ^{nat}Al foils underwent a γ spectrometry acquisition (45÷60 min) only once, 1 or 2 days after the EoB, to detect the ^{57}Ni ($T_{1/2}$= 35.60 h) activity produced through the ^{nat}Ni(p,x)^{57}Ni monitor reaction and eventually transferred to the following ^{nat}Al layer. A list of the γ rays emitted and their characteristics is reported in table 3.6. They were used to identify the produced radionuclides in the γ spectra.

For each produced radionuclide, activity at the EoB was determined for each γ spectrum of the same foil and a mean value was then calculated. Any correlation between uncertainties was assessed negligible considering the large errors involved (7÷15% uncertainty on the target thickness, 4÷5% uncertainty on the monitor cross-section, on average <1% and at most 2% reduction due to uncertainties correlation).

Two n-type CANBERRA HPGe detectors (CANBERRA PACKARD Central Europe GmbH, Schwardorf, Austria), each coupled to ORTEC DSPEC Pro electronics (ORTEC/AMETEK, Oak Ridge National Laboratory, USA) and cooled by liquid nitrogen, were used for the γ spectroscopy measurements at the GIP ARRONAX facility, which can be seen in figures 3.17 and 3.18. In those figures

Table 3.6: Characteristics of the γ rays emitted by the produced radionuclides from NuDat 3.0 database [7]. The italic numbers are the uncertainties.

Radionuclide	Half-life	γ emission energy (keV)	γ emission intensity (%)
^{43}Sc	3.891 h *12*	372.9	22.5
^{44m}Sc	58.61 h *10*	271.251	86.72
^{44g}Sc	4.0420 h *25*	1157.022	99.8867 *30*
^{46}Sc	83.79 d *4*	889.277	99.9840 *10*
^{47}Sc	**3.3492 d *6***	**159.381**	**68.3 *4***
^{48}Sc	43.71 h *9*	1037.522	97.5 *20*
^{48}V	15.974 d	983.525 1312.105	99.98 *4* 98.2 *3*
^{57}Ni	35.60 h *6*	1377.63	81.7 *24*

the positioning of the targets is also visible: it is at 19 cm from the detector surface in figure 3.17 and at 25 cm in figure 3.18. The distance allowed to contain the dead time of the detector at typically about 3% and, however, always below than 10%. The deposition was always placed with the enriched Ti surface facing the detector and the support upwards, to avoid the γ absorption by the Al substrate. All the layers coming from the same stacked-foils target were always measured with the same detector. The acquired γ spectra were analysed with the jRadView_09_2018 software developed at the INFN-LNL.

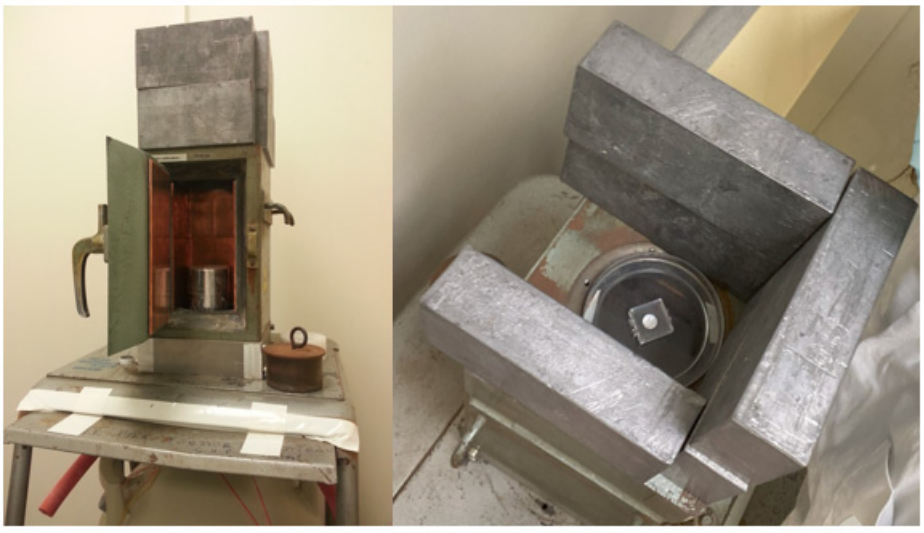

Figure 3.17: First HPGe detector used for measurements: front and top view. Positioning of the target is at 19 cm far from the detector surface, shielded by lead blocks.

The detectors were calibrated in energy and efficiency. While energy calibration is periodically checked by GIP ARRONAX staff, I performed the efficiency

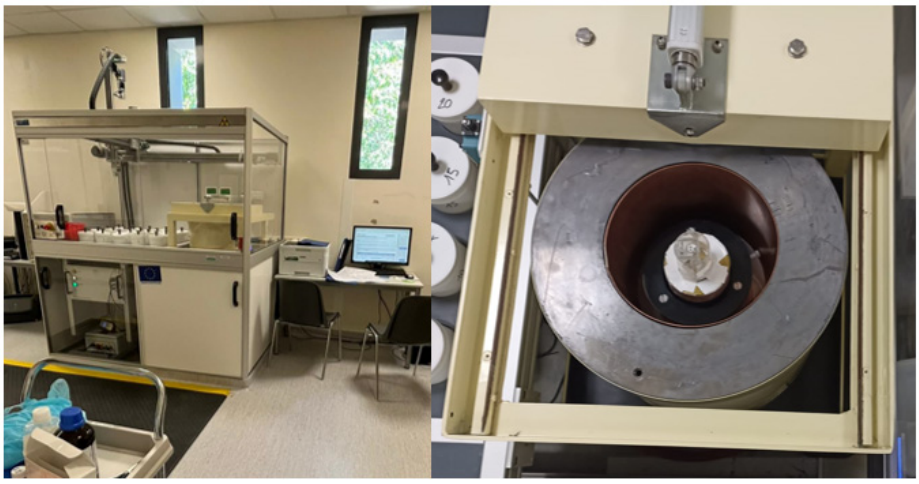

Figure 3.18: Second HPGe detector used for measurements: front and top view. The detector is actually inside the structure developed at ARRONAX for automated measurements. Positioning of the target is at 25 cm far from the detector surface. A computer controlled enclosing lead structure shields the detector from the background.

calibration for the measurements' configurations used in PASTA and REMIX experiments in November 2021. The multi γ emitting ^{152}Eu was used in combination to the single low-energy γ emitting ^{241}Am to extend the calibration energy range. The two point-like sources, purchased from CERCA-LEA (AREVA CERCA-LEA, France), can be seen in figure 3.19. In figure 3.20 the efficiency calibration curves obtained for the two detectors are reported: the left curve is referred to the HPGe detector in figure 3.17 while the right one belongs to the HPGe detector in figure 3.18. An error of 5% was associated to the detector efficiency values extracted from these curves and used in cross-section calculations.

Figure 3.19: ^{152}Eu and ^{241}Am point-like sources used for the efficiency calibration of the HPGe detectors.

To the cross-section values obtained for each Ti bombarded deposition a beam energy value should be associated. This was estimated with SRIM-2013 Monte Carlo code [104]. Known the initial beam energy, the thickness of Kapton foil preserving the beam line vacuum, the distance between the end of beam line

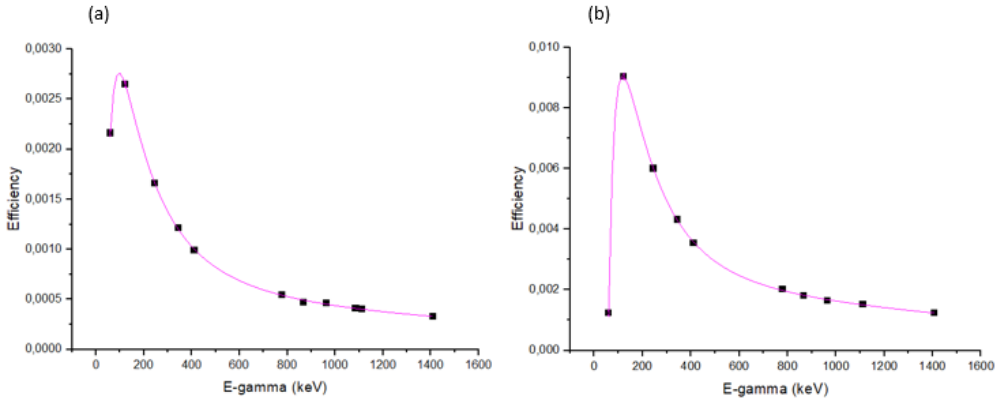

Figure 3.20: (a) Efficiency calibration curve corresponding to the detector in figure 3.17. (b) Efficiency calibration curve corresponding to the detector in figure 3.18.

and the stacked-foils target, and the thickness and composition of all the foils contained, the beam energy loss through the target could be simulated. SRIM returns also a graphic description of the simulation, reported here in figure 3.21 for the case of the REMIX-9 experiment. Those simulations also confirmed the assumption that the energy in the thin Ti depositions remains almost constant.

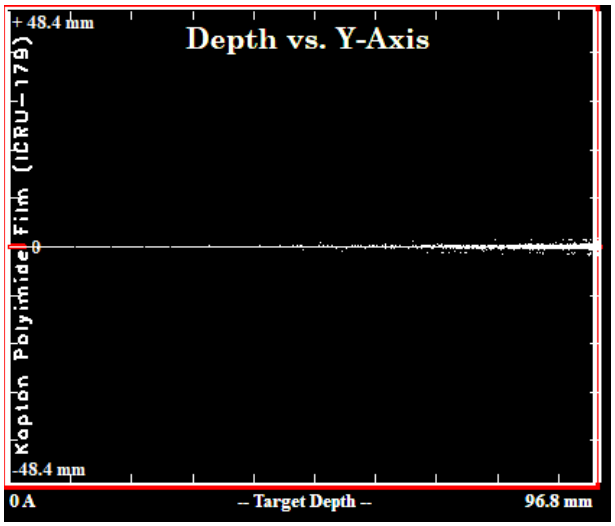

Figure 3.21: SRIM-2013 simulation to evaluate the proton beam energy loss and straggling through the target during the irradiation run of the experiment REMIX-9.

SRIM simulations were also used to estimate the energy uncertainty given by two components: the intrinsic uncertainty on the extracted beam energy suggested by the cyclotron manufacturer (IBA) as 0.5 MeV, and the straggling of the protons crossing all the materials (Kapton foil, air, target layers), as is represented in figure 3.21. The combination of these two effects caused an uncertainty in the energy, dE, between ± 0.54 and ± 0.89 MeV.

3.4.2 γ spectroscopy at the Bern cyclotron laboratory

At the Bern hospital facility each deposition was activated separately and only production of longer-lived radionuclides was expected, namely ^{47}Sc and in some cases ^{46}Sc. Hence, only one long (2÷17 h) γ spectroscopy measurement was performed for each target in the same day of the irradiation run or the day after. For the target in which the production of ^{46}Sc occurred, a γ acquisition was repeated about one month after the EoB, with a duration of many days since we were near the threshold energy of the nuclear reaction.

Targets were positioned at a distance of 10 cm in the n-type CANBERRA HPGe detector available at the Bern laboratory. The support used to maintain that distance can be seen in figure 3.22 (a). From this photograph it can also be noted that the deposition was measured as it was bombarded: in the aluminium capsule enveloped with the aluminium foil since at the low energies involved Al is not activated so it did not interfere in the γ spectra. In figure 3.22 (b) there is the shielding surrounding the detector, in which the support with the target placed on it was inserted. The 10 cm configuration was typically used by the Bern group, so the energy and efficiency calibrations were already performed using a multi-peak source. The activity of the source was known with a precision of about 1%, resulting in an uncertainty associated to the efficiency of 2÷3% [66].

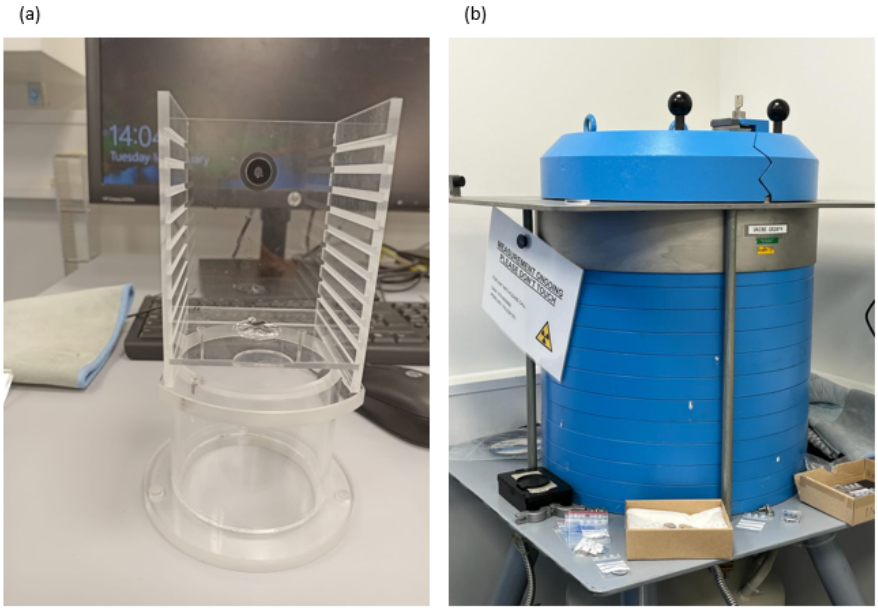

Figure 3.22: (a) Support used to place the target at the already calibrated distance of 10 cm from the detector surface. (b) Detector shielding in which the support with the target is inserted.

γ spectra analysis was performed using the InterSpec software released by GammaSpectacular (Bee Research Pty Ltd trading as Gammaspectacular.com, Sydney, Australia).

Chapter 4

Production cross-sections of ^{47}Sc and contaminant radionuclides

The analysis of the cross-section trends is the first step towards the optimization of the irradiation parameters to improve the purity of a final product. Cross-section values, measured and calculated in this thesis work as described in chapter 3, are here presented and discussed to eventually individuate a possible energy range in which the production of ^{47}Sc is high while the presence of contaminants is minimized. The results are compared to the literature data [86,105,106], which, when available, are generally scarce. Also, theoretical curves reproducing the expected cross-section trends are reported together with experimental results. Theoretical estimations were obtained with TALYS 1.96 software [107], run with default parameters. The only inputs were beam energy and particle type, and target composition. A collaboration with the experts in TALYS code, Dr. Luciano Canton and Dr. Francesca Barbaro, is carried on to improve the microscopic description of nuclear reactions implemented in TALYS, operating both on optical models and nuclear density levels [84]. All the possible combinations are evaluated to individuate which parameters better describe the experimental data. The results of this massive investigation are a topic of the Dr. Francesca Barbaro's Ph.D. thesis [108]. It is worth to underline its importance since an appropriate reproduction of experimental data is relevant to predict, using the optimized parameters, the production cross-sections of both stable and unmeasurable Sc-isotopes: in this case, the former is represented by ^{45}Sc, the only stable Sc-isotope, while an example of the latter is ^{49}Sc which emits only low intensity γ rays hardly detectable (E_γ= 1622.6 keV (0.010%), 1761.9 keV (0.050%), $T_{1/2}$= 57.18 m [7]). The knowledge of undetectable isotopes is important to characterize

the final product, through the following quantities:

- **Specific activity (SA)**. It is the activity of a radioisotope divided by the mass of the target to which contribute both stable and unstable nuclei contained. It is usually expressed as $\frac{Ci\ (or\ Bq)}{mol\ (or\ g)}$ and it should be as high as possible meaning that there will not be competition in some chemical processes like, for example, the labelling procedures [78].

- **Isotopic purity (IP)**. It is the ratio of a radioisotope over all its isotopes, both radioactive and not, expressed as a percentage.

- **Radionuclidic purity (RNP)**. It is defined as the ratio, in percentage, between the activity of the radionuclide of interest and the total activity of all the radionuclides produced. When those radionuclides are isotopes of the same element RNP coincides with radioisotopic purity.

It is important to specify that all these quantities depend on time, so they change with it. They are of particular importance in radiopharmacy and radiochemistry to determine the efficiency of a radiolabelling process and with consequences on the dose delivered to a patient [109]. Besides, they are helpful to individuate if there are optimal irradiation parameters for a large-scale production of a medical radionuclide for which a high purity is required. To achieve this goal, all the co-produced contaminants have to be considered. This is why all of them are presented and discussed here. Among them, non-isotopic contaminants raise less worries since they can be separated chemically, usually with a really high efficiency [110]. For isotopic contaminants with a half-life considerably shorter that the radionuclide of interest, a proper cooling time can be waited to let them decay. When isotopic contaminants with longer half-life are co-produced (and a mass separation set up is not available), the only solution is to try to avoid their production as much as possible. This can be achieved by evaluating and comparing the cross-sections as a function of the beam energy. In the case of ^{47}Sc ($T_{1/2}$=3.3492 d [7]), the main contaminant to avoid is ^{46}Sc. Its half-life is 83.79 d [7], considerably longer than the ^{47}Sc one, thus particular attention is paid to the ^{46}Sc co-production. It should be stated that, in this work, with ^{46}Sc is meant its cumulative cross-section since this radionuclide has a very fast decaying metastable state, ^{46m}Sc ($T_{1/2}$= 18.75 s [7]), undetectable in offline measurements, which undergoes an isomeric transition in 100% of cases. In the results, presented and discussed in the following sections 4.1, 4.2, and 4.3, the obtained ^{47}Sc and ^{46}Sc cross-section trends are always compared.

4.1 Experimental cross-sections for proton beams on ^{48}Ti targets

In the context of the PASTA project the production of ^{47}Sc using proton beams on enriched ^{48}Ti targets has been investigated up to 45 MeV. The energy interval was then expanded up to 70 MeV during the REMIX project. Only two old sets of data were already available in literature: one by E. Gadioli et al. dating back to 1981 [103], and the other by V. N. Levkovski published in 1991 [111]. E. Gadioli et al., in their experiments, used targets made up of enriched $^{48}TiO_2$ powder mixed with CuO powder to exploit ^{63}Cu(p,n)^{63}Zn, for the 7÷20 MeV energy range, and ^{65}Cu(p,pn)^{64}Cu, between 25 MeV and 85 MeV, as monitor reactions. Nowadays, those two reactions are not recommended by IAEA to monitor the beam flux and energy [99]. V. N. Levkovski used the ^{nat}Mo(p,x)^{96}Tc reaction as monitor whose cross-section values were previously measured by him in a separate experiment. His monitor reaction values are always higher, of about 20% on average, than that suggested by IAEA at present. Consequently, his results have to be multiplied by a factor 0.8 to normalize his data [112]. To indicate that the normalization has been performed, an asterisk is used in the legend of figures 4.2, 4.3, 4.5, 4.7, 4.13, 4.15, and 4.17.

Giving such few literature data, CSN5 of the INFN decided to fund additional experiments on the ^{48}Ti(p,x)^{47}Sc nuclear reaction with PASTA and REMIX projects. The results, presented in this thesis, have been also recently published in [113]. The monitor reaction exploited in this work was ^{nat}Ni(p,x)^{57}Ni. Its cross-section as a function of energy is tabulated by IAEA, with a step of 0.1 MeV [99]. The values corresponding to the beam energy in the monitor foils were extrapolated and are here reported in table 4.1.

The ^{47}Sc and its contaminants cross-sections presented in table 4.2 are obtained thanks to the values reported in table 4.1, except for the value at the lowest energy, 18.2 MeV, which was measured at the Bern cyclotron laboratory where a precise measure of the beam flux was possible, and the monitor was not needed, as explained in chapter 3. At this energy, the production of ^{48}V was expected but it was not possible to measure its activity due to the presence of some residual activity from a previous irradiation of the same target.

Only one of the monitor foils (the one bombarded with protons of 39.31 MeV) was used to evaluate the beam flux in two close ^{48}Ti foils in the same stack, whose irradiation energies were 39.63 MeV and 37.56 MeV. All the other ^{48}Ti foils had

Table 4.1: Beam energy in the monitor foils and corresponding cross-section values of the ^{nat}Ni(p,x)^{57}Ni monitor reaction used in calculations.

Beam energy in ^{nat}Ni foil E ± dE (MeV)	Monitor reaction cross-section $\sigma_r \pm d\sigma_r$ (mb)
22.42 ± 0.91	148.7 ± 6.3
26.30 ± 0.86	180.1 ± 7.5
29.01 ± 0.76	162.8 ± 6.8
31.33 ± 0.67	134.0 ± 5.6
33.13 ± 0.85	116.6 ± 4.9
35.63 ± 0.73	99.3 ± 4.2
39.31 ± 0.57	85.6 ± 3.6
42.22 ± 0.68	80.4 ± 3.5
44.59 ± 0.56	77.8 ± 3.4
51.26 ± 0.76	73.4 ± 3.1
53.48 ± 0.67	72.3 ± 3.1
59.73 ± 0.67	69.5 ± 3.0
67.88 ± 0.66	66.9 ± 2.9

their own monitor foil.

^{48}Ti(p,x)^{43}Sc cross-section

The threshold energy of this reaction is 24 MeV at which the ^{48}Ti(p,2nα)^{43}Sc channel opens, specifically. Other channels are then opened starting from 36 MeV. The measured production cross-section determined by those reaction channels are reported in figure 4.1 up to 70 MeV. In addition to experimental results obtained within this work and by Gadioli et al., the theoretical curve simulated using TALYS 1.96 software with default parameters is included for comparison.

A general good agreement can be noticed between the two sets of experimental data. Only at beam energies close to 70 MeV, where the curve shows a minimum, the discrepancy between the two experimental trends is about 25%. Although, the difference between the two points at about 45 MeV is only nearly 13%. The TALYS theoretical trend obtained with default parameters, instead, differs more significantly: it seems shifted towards lower energies and predicts a higher value for the peak than the observed one. Also, the rise after the minimum seems to be anticipated.

Table 4.2: Cross-section results for ^{48}Ti(p,x)^{43}Sc, ^{44m,g}Sc, ^{46}Sc, ^{47}Sc, ^{48}V reactions.

Beam energy in ^{48}Ti foil $E \pm dE$ (MeV)	Cross-section of ^{43}**Sc** $\sigma_x \pm d\sigma_x$ (mb)	Cross-section of ^{44g}**Sc** $\sigma_x \pm d\sigma_x$ (mb)	Cross-section of ^{44m}**Sc** $\sigma_x \pm d\sigma_x$ (mb)	Cross-section of ^{46}**Sc** $\sigma_x \pm d\sigma_x$ (mb)	Cross-section of ^{47}**Sc** $\sigma_x \pm d\sigma_x$ (mb)	Cross-section of ^{48}**V** $\sigma_x \pm d\sigma_x$ (mb)
18.2 ± 0.4					4.0 ± 0.3	
22.7 ± 0.9		11.5 ± 1.2	3.4 ± 0.3		11.9 ± 1.1	64.5 ± 5.7
26.7 ± 0.8		47.4 ± 9.4	13.9 ± 2.7		19.9 ± 3.9	41.9 ± 8.2
29.3 ± 0.8		49.9 ± 5.0	16.3 ± 1.6		24.1 ± 2.3	31.4 ± 3.0
31.5 ± 0.7		52.8 ± 5.2	19.9 ± 1.8	10.9 ± 2.2	28.1 ± 2.5	30.5 ± 2.7
33.0 ± 0.8		43.9 ± 4.2	17.3 ± 1.6	18.0 ± 2.0	23.9 ± 2.2	27.8 ± 2.5
35.5 ± 0.7	3.9 ± 0.6	34.8 ± 3.3	16.0 ± 1.4	39.3 ± 3.9	22.1 ± 2.0	25.6 ± 2.3
37.6 ± 0.7	8.3 ± 0.9	25.1 ± 2.5	12.6 ± 1.1	48.9 ± 4.8	22.4 ± 2.0	24.6 ± 2.2
39.6 ± 0.6	12.9 ± 1.2	18.5 ± 1.8	9.8 ± 0.9	63.7 ± 6.2	21.4 ± 1.9	23.7 ± 2.2
42.0 ± 0.7	16.2 ± 2.2	13.3 ± 1.9	6.9 ± 0.6	67.9 ± 6.2	20.6 ± 1.8	19.9 ± 1.7
44.8 ± 0.5	14.2 ± 2.3	10.4 ± 1.4	4.6 ± 0.5	75.0 ± 7.4	19.1 ± 1.8	19.0 ± 1.8
51.4 ± 0.8	11.0 ± 1.1	8.4 ± 0.8	4.0 ± 0.4	65.9 ± 6.0	19.5 ± 1.7	17.8 ± 1.6
53.6 ± 0.7	9.6 ± 1.2	8.4 ± 0.9	4.6 ± 0.4	63.7 ± 5.9	19.1 ± 1.7	17.9 ± 1.6
59.9 ± 0.7	6.5 ± 0.8	12.7 ± 1.3	8.1 ± 0.7	53.7 ± 5.1	18.7 ± 1.7	13.2 ± 1.2
68.0 ± 0.7	4.1 ± 0.6	25.7 ± 2.6	14.1 ± 1.3	48.2 ± 4.8	16.9 ± 1.5	10.1 ± 1.0

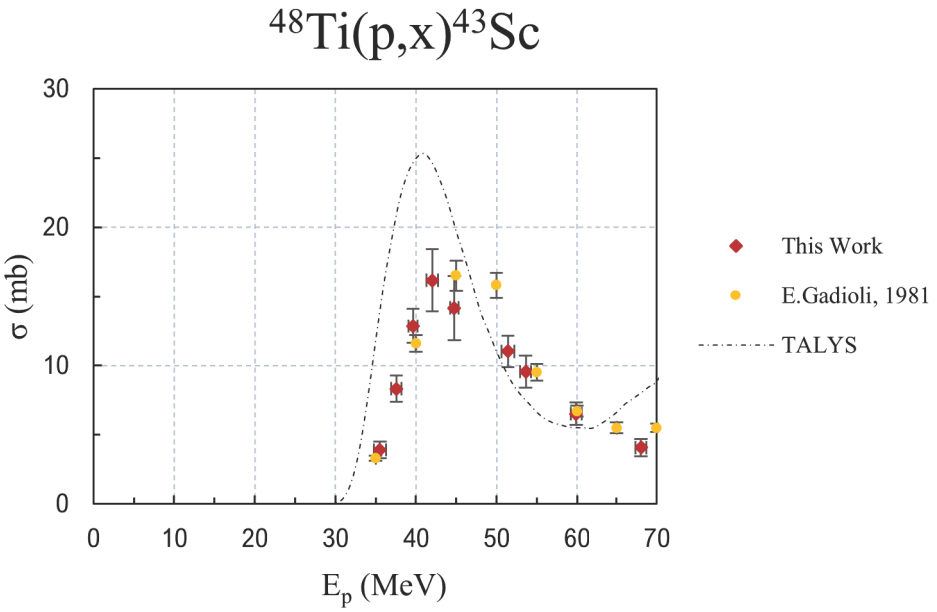

Figure 4.1: Cross-section trend of the ^{48}Ti(p,x)^{43}Sc reaction.

^{48}Ti(p,x)^{44m,g}Sc cross-sections

The threshold energy for the ^{48}Ti(p,x)^{44}Sc reaction is about 14 MeV. At this energy the channel (p,nα) is open producing both ^{44g}Sc and ^{44m}Sc, the latter decaying in ^{44g}Sc with a branching ratio of 98.80% while the remaining 1.20% goes into the stable ^{44}Ca. So, ^{44g}Sc is produced both directly and indirectly. The cross-section trend shown in figure 4.2 refers only to the directly produced one. In this case two old datasets were available in literature and are reported for comparison: one by Gadioli et al. (in yellow) and the other by Levkovski (in grey), corrected for the above mentioned 0.8 factor.

The experimental trend obtained in this thesis work is in a general accordance with the other results, however, especially in the energy range between 30 MeV and 50 MeV, the points by Gadioli et al. overestimate this work results of about 30% on average. On the other hand, the theoretical estimation properly reproduces the experimental trends up to 30 MeV, but it slightly underestimates the data up to 50 MeV, while overestimates the rise starting above 50 MeV.

In figure 4.3 the production cross-section obtained for ^{44m}Sc can be seen in comparison with the only available set by Levkovski which stops at 30 MeV.

Except for the lowest energy point of this work, which differs of about 40% from the Levkovski results, there is a quite good agreement between the two sets of data. This is not true for the TALYS default estimation which abundantly

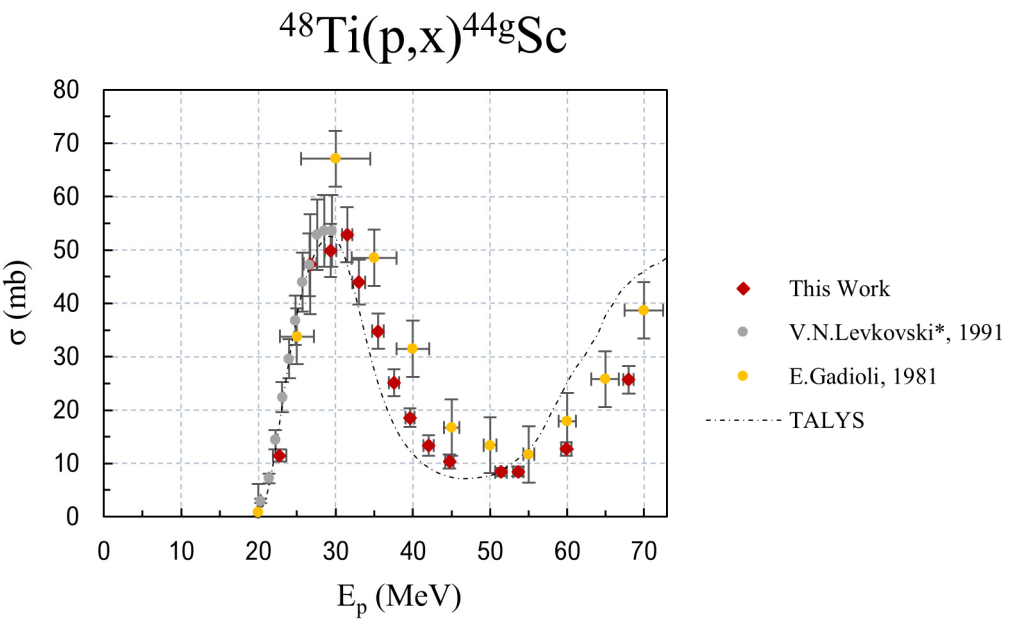

Figure 4.2: Cross-section trend of the ^{48}Ti(p,x)^{44g}Sc reaction.

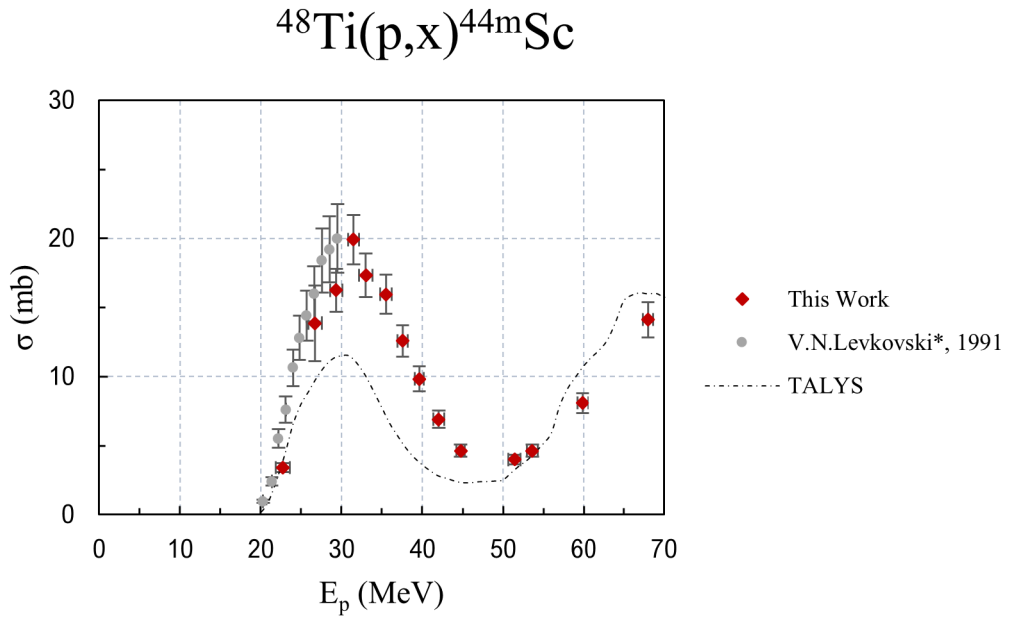

Figure 4.3: Cross-section trend of the ^{48}Ti(p,x)^{44m}Sc reaction.

underestimates the experimental data up to 50 MeV while slightly overestimates this thesis work outcomes above 50 MeV. The TALYS code deviation from experimental points is far more evident in this case than for ^{44g}Sc.

^{48}Ti(p,x)^{46}Sc cross-section

The reaction channels contributing to the production of ^{46}Sc are all opened in a short threshold energy range: at almost 15 MeV there is the threshold for the (p,^{3}He) channel, the (p,pd) channel starts at about 20 MeV and the contribution of the (p,n2p) channel has nearly 23 MeV threshold energy. Only Gadioli et al. measured this cross-section before, as reported in figure 4.4.

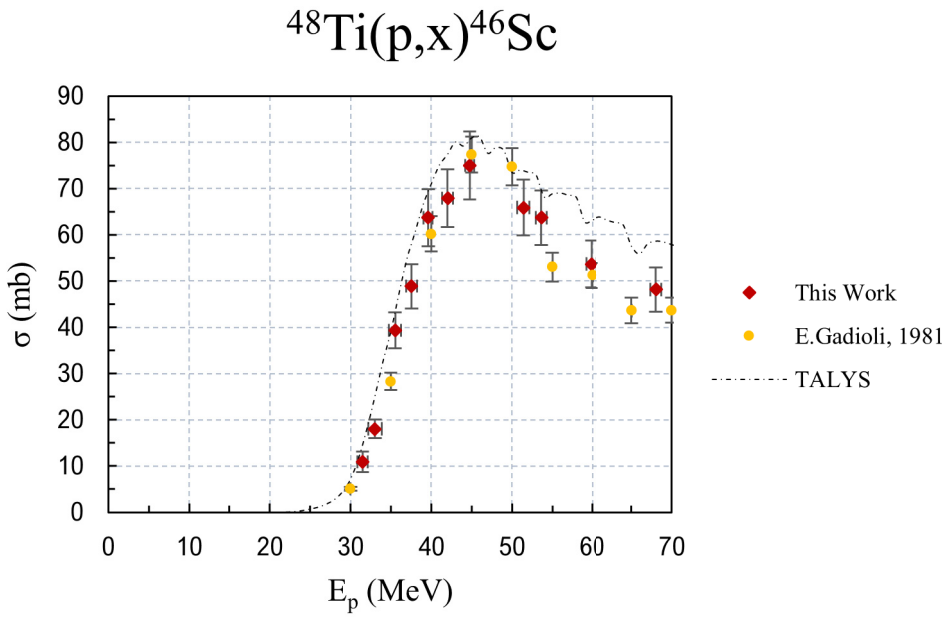

Figure 4.4: Cross-section trend of the ^{48}Ti(p,x)^{46}Sc reaction.

A good agreement can be observed between the experimental sets of data in the whole energy range investigated in this work. Also, the theoretical estimation shows a great correspondence with experimental points despite a slight overestimation above 50 MeV.

^{48}Ti(p,2p)^{47}Sc cross-section

The reaction ^{48}Ti(p,2p)^{47}Sc has its threshold energy slightly below 12 MeV. Its cross-section trend is reported in figure 4.5 together with the literature data by Gadioli et al. and Levkovski.

A good agreement can be seen between this work results and the previous literature data, even if in the energy range between 30 MeV and 50 MeV, similarly to the case of ^{44g}Sc production cross-section, Gadioli et al. results overestimation is about 20÷25%. Besides, the theoretical trend also overestimates the experi-

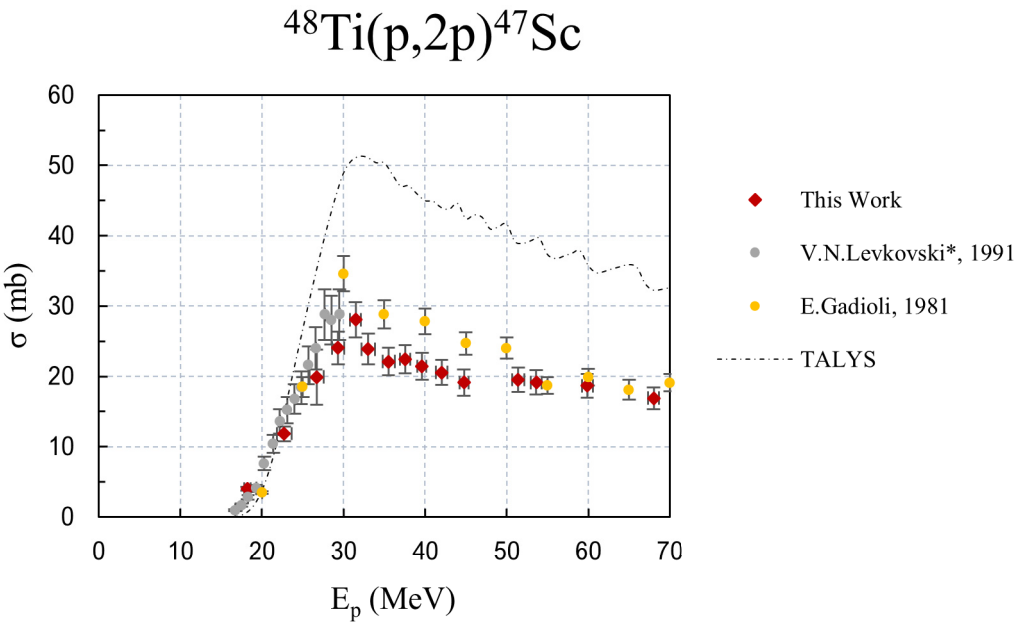

Figure 4.5: Cross-section trend of the ^{48}Ti(p,2p)^{47}Sc reaction.

mental data, in fact it approximately doubles the experimental values above 30 MeV beam energies.

TTY calculations for ^{48}Ti targets

Comparing the ^{47}Sc and ^{46}Sc cross-section trends, it is possible to observe that up to 30 MeV the isotope of interest can be produced without or with a low co-production of its main contaminant. However, in this energy region, ^{44g,m}Sc are already produced and their presence must be taken into account. In fact, even if the half-lives involved are shorter than ^{47}Sc one ($T_{1/2}$= 4.0420 h and 58.61 h respectively vs. $T_{1/2}$= 80.3808 h), they are not short enough to be neglected, particularly considering that ^{44g}Sc is continuously formed from ^{44m}Sc decay. The production yields of ^{47}Sc and its contaminants were then calculated to evaluate if the presence of isotopic contaminants is low enough to allow a clinical use of the final product. Considering the cross-section trends, the yields calculation was limited to the energy region below 40 MeV. Thus, TTYs were calculated in four energy intervals, namely 25÷15 MeV, 30÷15 MeV, 35÷15 MeV, and 40÷15 MeV, for the radionuclides ^{47}Sc, ^{44g}Sc, ^{44m}Sc, ^{46}Sc, and ^{43}Sc when produced. To perform those calculations, all the experimental cross-sections presented in figures 4.1÷4.5 were fitted with a polynomial function of the 5^{th} or 6^{th} order in the energy range of interest. An example of the polynomial fit for the ^{47}Sc experimental cross-section

values is reported in figure 4.6. The obtained fits constituted, together with the stopping powers extracted from SRIM-2013 [104], the element to be integrated in equation 3.16. The TTYs' calculations were performed assuming a beam current of 1 μA and irradiation times of 24 h and 80 h (approximately one ^{47}Sc half-life). The results regarding the activities produced at the EoB are listed in table 4.3.

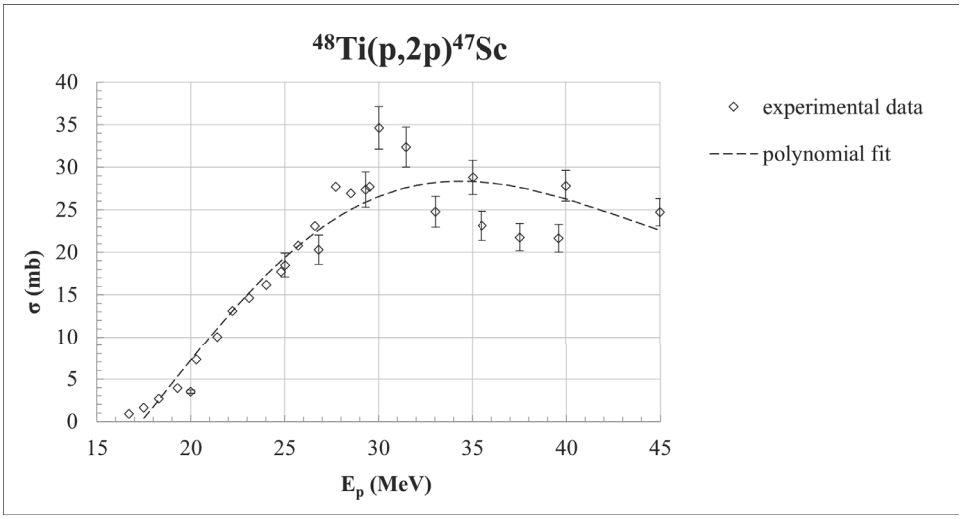

Figure 4.6: Polynomial fit of the 6^{th} order of the ^{48}Ti(p,2p)^{47}Sc experimental cross-section datasets.

Table 4.3: Calculated yields, from Sc-isotopes cross-sections using ^{48}Ti targets, considering different energy intervals and irradiation times and assuming 1 μA beam current.

$\mathbf{t_{irr}}$ **=24 h**				
TTY	15÷25 MeV Yield (MBq)	15÷30 MeV Yield (MBq)	15÷35 MeV Yield (MBq)	15÷40 MeV Yield (MBq)
^{47}Sc	73.4	198	364	556
^{46}Sc			4.8	19.4
^{44m}Sc	38.9	154	297	412
^{44g}Sc	447	1790	3270	4230
^{43}Sc			19.9	289
$\mathbf{t_{irr}}$ **=80 h**				
TTY	15÷25 MeV Yield (MBq)	15÷30 MeV Yield (MBq)	15÷35 MeV Yield (MBq)	15÷40 MeV Yield (MBq)
^{47}Sc	196	529	971	1480
^{46}Sc			15.8	64.1
^{44m}Sc	96.2	381	736	1020
^{44g}Sc	454	1820	3320	4300
^{43}Sc			20.2	293

Those TTYs calculated from experimental results were used to estimate the final product RNP at the EoB and its evolution with time to perform the dosimet-

ric evaluations described in chapter 5, which will allow to compare this production route for the medical radionuclide ^{47}Sc with the other ones.

^{48}Ti(p,n)^{48}V cross-section

The non-isotopic ^{47}Sc contaminant ^{48}V is produced via the (p,n) type reaction in ^{48}Ti targets with a threshold energy of almost 5 MeV. Differently from the previous nuclear reactions, the (p,n) channel was widely measured in the last century, as can be seen in figure 4.7 where, together with this work results, not only data by Gadioli et al. and Levkovski are reported, but also datasets by West et al. [114], Antropov et al. [115], and Tanaka and Furukuma [116].

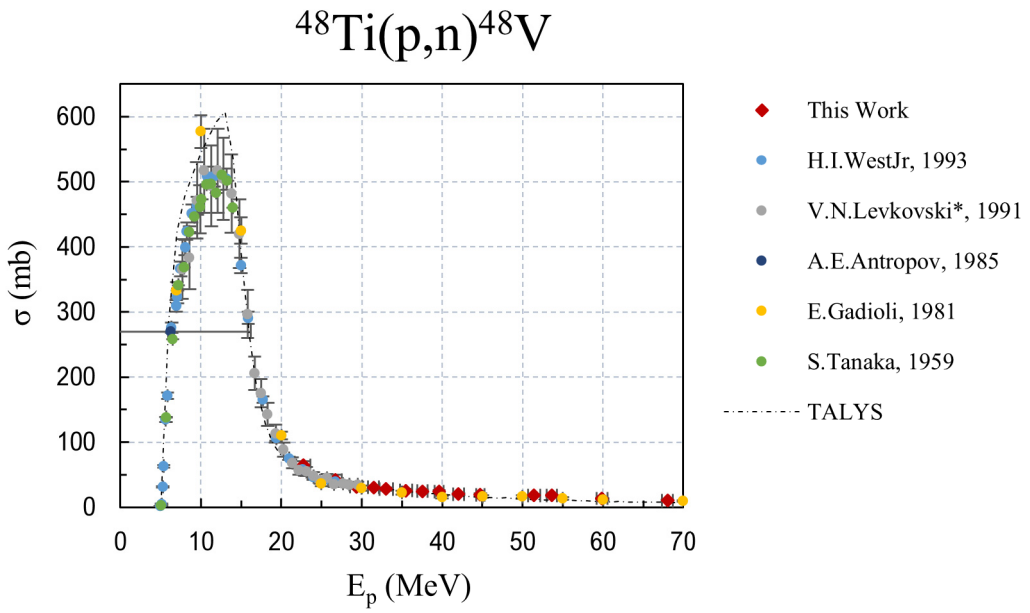

Figure 4.7: Cross-section trend of the ^{48}Ti(p,n)^{48}V reaction.

All the experimental data show a general good agreement in the cross-section trend and the theoretical prediction also reproduces these data very well, except for the overestimation of the peak.

Correction for ^{48}Ti presence in enriched ^{49}Ti and ^{50}Ti targets

All the experimental results here presented were used to correct the cross-section values obtained for the enriched ^{49}Ti and ^{50}Ti targets. It was necessary due to the presence of isotopic ^{48}Ti contamination in both ^{49}Ti and ^{50}Ti enriched powders employed in target manufacturing. For this purpose, cross-section experimental

data obtained for ^{48}Ti targets were fitted, and a *spline* weighed interpolation was chosen, as suggested in an IAEA TECDOC in case of independent measurements' sets with no crucial discrepancies [117]. The spline fit consists in the division of the available experimental points in smaller subsets to perform more independent polynomial fits, generally cubic, each in a subset. At the extremes of the subsets the continuous first and second derivatives constrains are applied to assure a smooth fitting curve. In the context of this thesis, the fit procedure was performed with the Scilab-2023.1.0 open-source software for numerical computation (Dassault Systèmes, Villacoublay, France) [118]. A spline weighed fit of the data was possible thanks to the interpolation function implemented in the software. The experimental cross-section points, and their uncertainties, were given as inputs together with the proton energies whose corresponding extrapolated cross-section values are required for the corrections. The extrapolated points were then printed by the software. In figure 4.8 there is the spline interpolation for ^{47}Sc as example: black dots are experimental points while the crosses along the green line (fitting curve) are the new points used for the corrections, in this case, of the results concerning the ^{49}Ti targets.

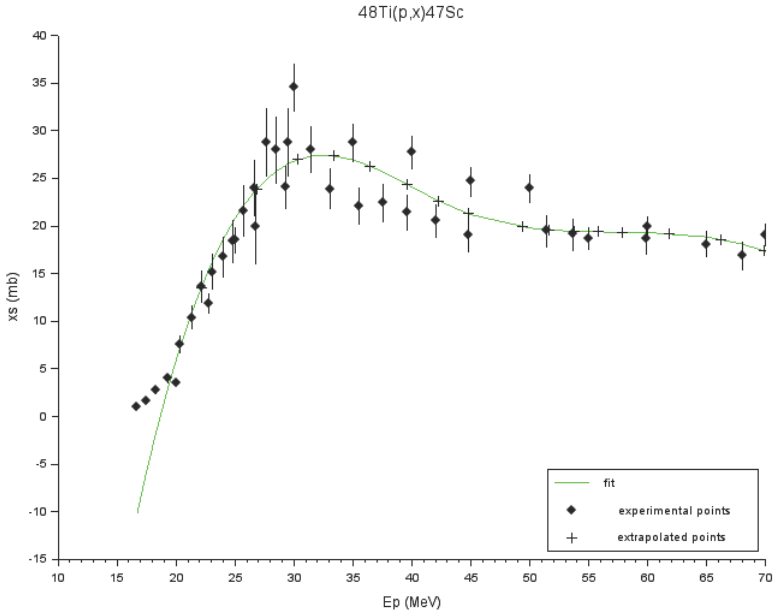

Figure 4.8: Spline weighed interpolation of the ^{48}Ti(p,2p)^{47}Sc experimental points. The green line is the fitting curve of the experimental points (black dots). The crosses are the extrapolated points for corrections.

The production cross-section threshold is not very well reproduced by the spline fitting. However, corrections in this low energy region are never needed in

this work, and, in any case, the cross-section values are fairly small to consider the corresponding corrections negligible.

4.2 Experimental cross-sections for proton beams on ^{49}Ti targets

Cross-section measurements for the proton-induced production of ^{47}Sc using enriched ^{49}Ti targets were never performed before. REMIX project results constituted a step forward also for the nuclear physics scientific community. Not only ^{47}Sc but also many of its contaminants were measured for the first time thanks to the research activities reported in this thesis. In the other cases, there are only few literature data. Few are the sets of data available for ^{48}V, in particular, only West Jr et al. [114] and Levkovski [111] published cross-section results on this nuclear reaction, and only up to 30 MeV. Levkovski, in addition, focused also on two Sc-isotopes, namely ^{46}Sc and ^{48}Sc.

The monitor reaction values used in the cross-section calculations are reported in table 4.4. They always belong to the ^{nat}Ni(p,x)^{57}Ni monitor reaction used to quantify the beam flux across the stacked-target.

Table 4.4: Beam energy in the monitor foils and corresponding cross-section values of the ^{nat}Ni(p,x)^{57}Ni monitor reaction used in calculations.

Beam energy in ^{nat}Ni foil E ± dE (MeV)	Monitor reaction cross-section $\sigma_r \pm d\sigma_r$ (mb)
29.98 ± 0.81	149.5 ± 6.2
33.92 ± 0.78	110.4 ± 4.7
36.78 ± 0.69	93.8 ± 4.0
39.45 ± 0.56	85.3 ± 3.6
42.22 ± 0.68	80.4 ± 3.5
44.54 ± 0.76	77.8 ± 3.4
47.02 ± 0.69	75.9 ± 3.3
49.39 ± 0.57	74.4 ± 3.2
53.20 ± 0.76	72.4 ± 3.1
55.41 ± 0.68	71.4 ± 3.1
57.46 ± 0.57	70.5 ± 3.0
66.10 ± 0.73	66.8 ± 2.9
67.87 ± 0.66	66.2 ± 2.9
69.64 ± 0.56	65.5 ± 2.8

Table 4.5: Cross-section results for ^{49}Ti(p,x)^{43}Sc, ^{43}K, ^{44m,g}Sc, ^{46}Sc, ^{47}Sc, ^{48}Sc, ^{48}V reactions corrected for the presence of ^{48}Ti in the targets.

Beam energy in ^{49}Ti foil $E \pm dE$ (MeV)	Cross-section of ^{43}**Sc** $\sigma_x \pm d\sigma_x$ (mb)	Cross-section of ^{43}**K** $\sigma_x \pm d\sigma_x$ (mb)	Cross-section of ^{44g}**Sc** $\sigma_x \pm d\sigma_x$ (mb)	Cross-section of ^{44m}**Sc** $\sigma_x \pm d\sigma_x$ (mb)	Cross-section of ^{46}**Sc** $\sigma_x \pm d\sigma_x$ (mb)	Cross-section of ^{47}**Sc** $\sigma_x \pm d\sigma_x$ (mb)	Cross-section of ^{48}**Sc** $\sigma_x \pm d\sigma_x$ (mb)	Cross-section of ^{48}**V** $\sigma_x \pm d\sigma_x$ (mb)
30.2 ± 0.8			0.7 ± 0.1	0.22 ± 0.03	4.9 ± 0.8	5.6 ± 0.7	9.5 ± 1.0	150.9± 19.0
34.1 ± 0.8			8.5 ± 1.2	6.6 ± 0.9	5.2 ± 0.8	17.3 ± 2.3	8.8 ± 1.0	78.4 ± 10.3
36.9 ± 0.7			13.1 ± 1.5	12.0 ± 1.3	5.6 ± 0.7	24.5 ± 2.6	7.9 ± 0.8	54.0 ± 5.6
39.6 ± 0.6			24.8 ± 3.3	16.5 ± 2.1	9.5 ± 1.4	34.0 ± 4.2	9.0 ± 0.9	49.7 ± 6.2
42.4 ± 0.7			26.4 ± 4.3	17.8 ± 2.3	12.9 ± 1.8	37.9 ± 4.9	8.9 ± 1.0	43.1 ± 5.6
44.7 ± 0.8	0.5 ± 0.1		24.3 ± 3.3	15.1 ± 1.9	22.1 ± 3.0	36.5 ± 4.6	8.5 ± 0.8	44.7 ± 5.7
47.2 ± 0.7	1.5 ± 0.3	0.07 ± 0.04	19.5 ± 2.3	12.9 ± 1.4	29.6 ± 3.3	34.0 ± 3.6	8.4 ± 0.9	36.5 ± 3.9
49.6 ± 0.6	3.3 ± 0.5	0.26 ± 0.06	17.0 ± 2.3	11.7 ± 1.6	39.4 ± 5.3	35.1 ± 4.7	9.6 ± 1.0	33.5 ± 4.5
53.4 ± 0.8	6.1 ± 1.0	1.0 ± 0.1	14.0 ± 1.9	10.9 ± 1.4	69.9 ± 9.2	40.0 ± 5.2	10.5 ± 1.1	35.7 ± 4.7
55.5 ± 0.7	9.0 ± 1.7	1.6 ± 0.2	11.7 ± 1.6	9.5 ± 1.2	80.8 ± 10.5	40.3 ± 5.1	11.3 ± 1.4	33.0 ± 4.3
57.6 ± 0.6	7.7 ± 1.1	1.9 ± 0.2	9.9 ± 1.3	7.6 ± 1.0	72.6 ± 9.7	36.1 ± 4.8	10.1 ± 1.1	31.4 ± 4.2
66.2 ± 0.7	4.1 ± 0.9	3.0 ± 0.3	8.3 ± 1.1	6.2 ± 0.8	61.9 ± 8.3	31.7 ± 4.1	10.2 ± 1.0	23.3 ± 3.2
68.0 ± 0.7	3.5 ± 0.8	3.3 ± 0.4	10.3 ± 1.6	6.6 ± 0.9	61.4 ± 8.3	33.1 ± 4.4	10.3 ± 1.1	24.0 ± 3.3
69.7 ± 0.6	3.5 ± 0.7	3.0 ± 0.3	9.6 ± 1.3	6.7 ± 0.9	55.3 ± 7.4	32.4 ± 4.1	10.7 ± 1.1	19.9 ± 2.7

The outcomes, presented in table 4.5, have been previously corrected for the 2.71% of ^{48}Ti contained in the targets and contributing to the cross-sections. The formula expressed in equation 3.17, discussed in section 3.3, is used for the corrections. The variation after the contributions' subtraction is generally within 3% meaning that the presence of ^{48}Ti in the targets is not so impactful. The uncertainty associated to the cross-section values is mostly in the range 10÷15% and so, the variation after correction is abundantly contained. However, for some energy values in some cross-section trends, this variation reaches even more than 10÷15%. This happens near the thresholds of the reactions and where the cross-section values for ^{49}Ti targets are low, determining a great influence of the ^{48}Ti contribution. The other low isotopic contaminations in the targets (0.22% both of ^{46}Ti and ^{47}Ti and 0.6% of ^{50}Ti) were ascertained to be irrelevant.

Instead, the results regarding ^{48}Sc and ^{43}K are not corrected for the contribution to the cross-section due to the ^{48}Ti presence. ^{48}Sc is not produced bombarding ^{48}Ti with protons, while ^{48}Ti(p,x)^{43}K reaction has a really low cross-section in the energy range considered, and indeed ^{43}K is not detected in the γ spectra of the ^{48}Ti targets. A previous literature dataset is available, but it is constituted by few points and a reliable spline interpolation fit was not possible. However, considering its low cross-section and the average low influence of ^{48}Ti presence in ^{49}Ti targets, the lack of correction for this radionuclide can be considered worthless. ^{43}K production when using ^{49}Ti targets was anyway considered since its presence was detected in the 617.490 keV (I= 79.2%) γ peak but it also has a γ emission at 372.760 keV (I= 86.80%) which inteferes with the ^{43}Sc γ line at 372.9 keV (I=22.5%). The latter is the only ^{43}Sc enough intense γ emission. Therefore, ^{43}K activity from the 617 keV γ peak was used to correct the 372 keV γ peak so that the ^{43}Sc activity could be obtained.

^{49}Ti(p,x)^{43}Sc and ^{49}Ti(p,x)^{43}K cross-sections

The first reaction channel having ^{43}Sc as product is (p,3nα), opened at a threshold energy of 32 MeV. A second channel, (p,n2t), has ^{43}Sc as final product and a threshold energy of 44 MeV. Then, there are many other reaction channels opened, with thresholds above 50 MeV, producing ^{43}Sc.

Concerning the reaction product ^{43}K, three channels are already open in a threshold energy interval between 22 and 30 MeV. Many other channels are then opened above 43 MeV threshold energy. Cross-section results regarding this radionuclide are presented here since its activity is used to correct the ^{43}Sc one.

No previous literature data are available both for ^{43}Sc and ^{43}K, as can be seen in figures 4.9 and 4.10.

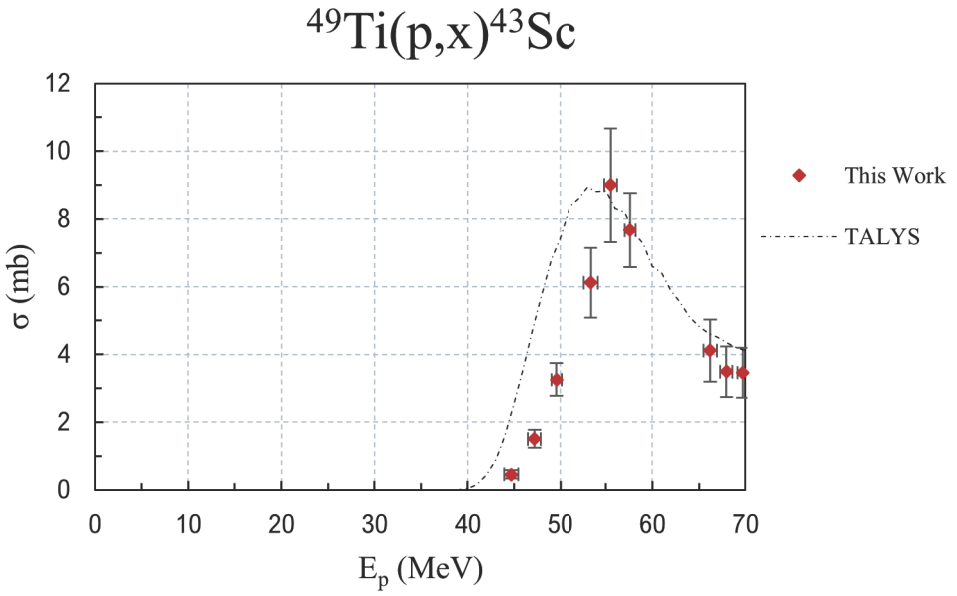

Figure 4.9: Cross-section trend of the ^{49}Ti(p,x)^{43}Sc reaction.

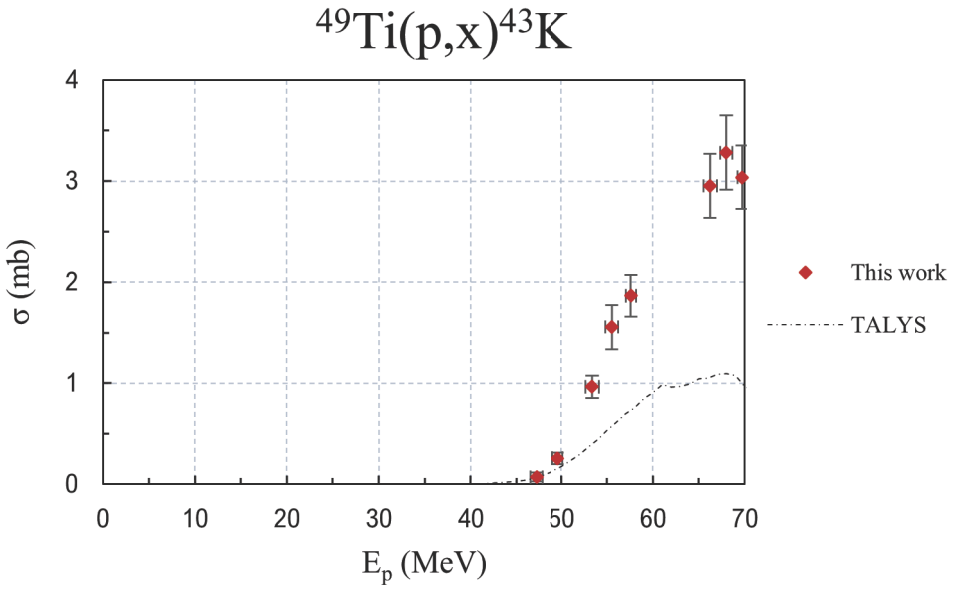

Figure 4.10: Cross-section trend of the ^{49}Ti(p,x)^{43}Sc reaction.

Only a comparison with theoretical simulations performed with the TALYS code is possible. TALYS well reproduces the experimental cross-section behaviour of ^{43}Sc but it seems to have an energy shift, less than 10 MeV, towards lower

energies. In the case of ^{43}K, instead, the theoretical curve is in accordance with experimental results only at the threshold, while it underestimates the outcomes of this thesis work up to about 60% when approaching the highest energy range investigated.

^{49}Ti(p,x)^{44m,g}Sc cross-sections

The first reaction channel for the production of ^{44m,g}Sc is (p,2nα) and opens at the threshold energy of 22 MeV. Subsequently, at 34 MeV, there is the threshold energy of the (p,2t) channel. Above 40 MeV, thresholds of many other reactions contributing to the ^{44}Sc production are encountered. The resulting cross-section trends are reported in figures 4.11 and 4.12.

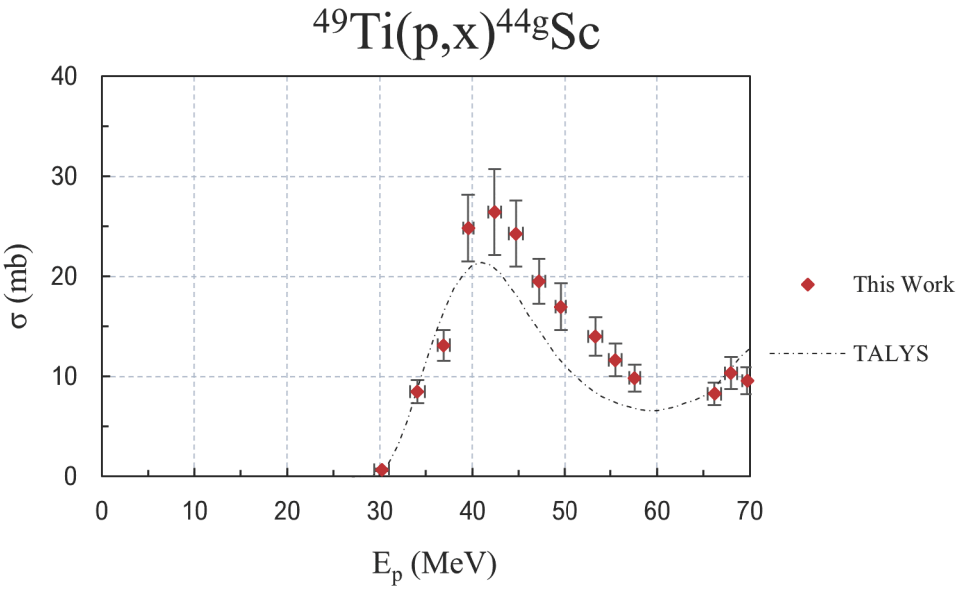

Figure 4.11: Cross-section trend of the ^{49}Ti(p,x)^{44g}Sc reaction.

The only possible comparison is with theoretical simulations performed with TALYS 1.96 software. Concerning the ^{44g}Sc cross-section, the theoretical curve, obtained keeping the default parameters in the code, reproduces quite well the experimental points. Only a slight underestimation, 20% on average, is observed in the middle energy region.

On the other hand, the theoretical trend simulating the production cross-section of ^{44m}Sc is widely in disagreement with the experimental values obtained in this work. The general trend is similar, however the values assumed by the theoretical curve are abundantly below the experimental cross-section data, with

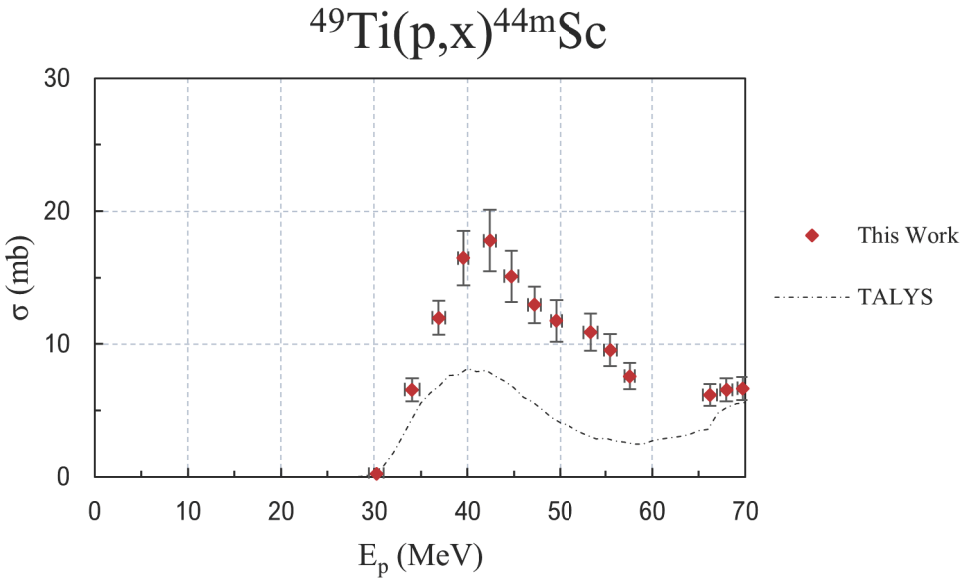

Figure 4.12: Cross-section trend of the ^{49}Ti(p,x)^{44m}Sc reaction.

a discrepancy higher than 50% at some energies.

The situation is analogous to the ^{48}Ti case: the TALYS code reproduces quite well the ^{44g}Sc experimental trend while, for the ^{44m}Sc, an underestimation of the experimental data occurs.

^{49}Ti(p,x)^{46}Sc cross-section

The production of ^{46}Sc starts quite soon since the reaction is a (p,α) with a threshold energy of almost 2 MeV. All the other channels involved in the ^{46}Sc production have a threshold energy included between 22 MeV and 30 MeV. No other channels contribute to the ^{49}Ti(p,x)^{46}Sc reaction up to 70 MeV. The contributions given by the (p,α) channel and by all the other channels can be clearly distinguished in figure 4.13: the first maximum is due to the (p,α) reaction and was previously measured by Levkovski and recently by Dellepiane et al. [66], the second rise is due to all the other channels and was measured in this thesis work for the first time.

The two low energy series of data show a general good accordance in the trend, even if a difference of about 30% can be observed for some beam energies. A comparison between those literature data and this work experimental results, reported in figure 4.13, is not possible since they refer to different energy ranges. Anyways, in principle they seem to describe the same trend.

The theoretical curve, instead, well interprets the experimental points be-

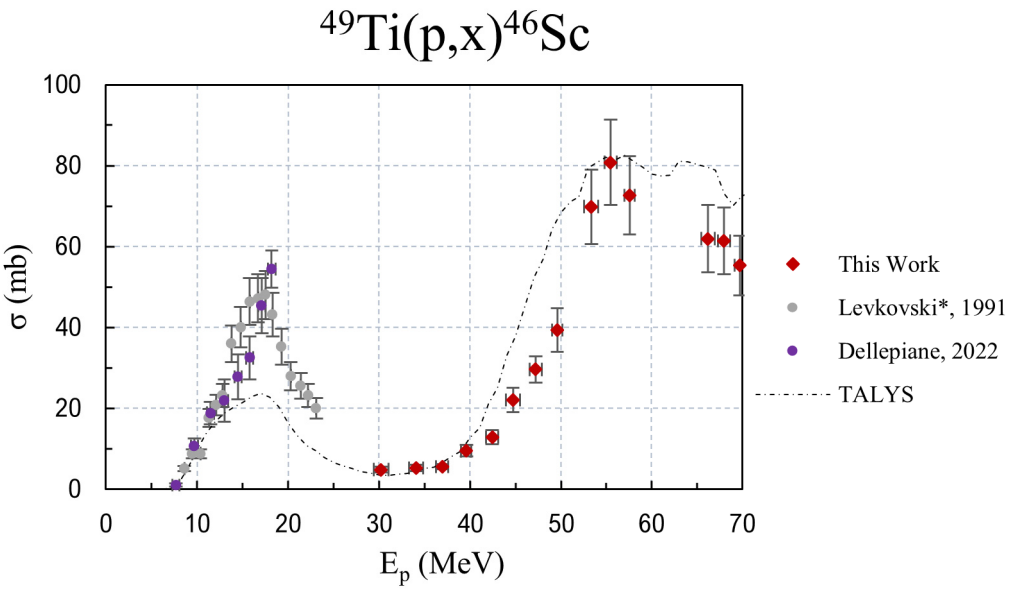

Figure 4.13: Cross-section trend of the ^{49}Ti(p,x)^{46}Sc reaction.

haviour but with some discrepancies in the values. In fact, the cross-section peak attributed to the (p,α) channel is underestimated: the theoretically predicted value at the maximum is about 50% less than the value measured by Levkovski. Moreover, the second rise given by all the other channels seems to be overestimated with discrepancies up to 40%. On the other hand, the minimum of the curve perfectly matches the data points.

^{49}Ti(p,x)^{47}Sc cross-section

Three are the possible channels producing ^{47}Sc, the radionuclide focus of this thesis when using enriched ^{49}Ti targets and all of them have quite low threshold energies:

- (p,^{3}He) is the first with a threshold energy of 12 MeV;
- (p,pd) is the second channel and has almost 18 MeV as threshold energy;
- (p,n2p) is the latter channel whose threshold energy is 20 MeV.

The result of these contributions, measured up to 70 MeV for the first time, is reported in figure 4.14. Similarly to the results obtained for the enriched ^{48}Ti targets, a wide theoretical overestimation of the experimental dataset is encountered. This difference is 50% on average.

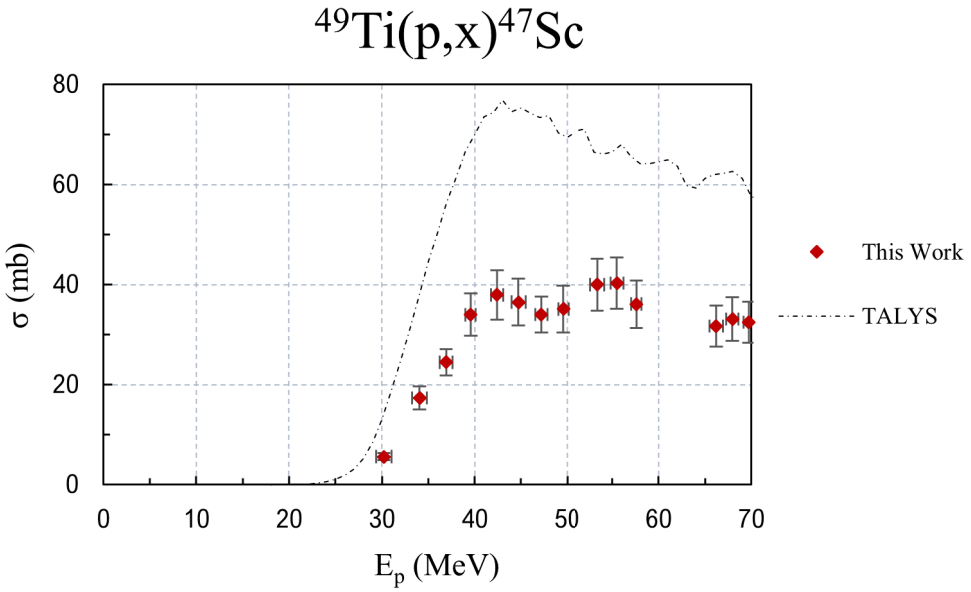

Figure 4.14: Cross-section trend of the ^{49}Ti(p,x)^{47}Sc reaction.

^{49}Ti(p,2p)^{48}Sc cross-section

The production of ^{48}Sc takes place in ^{49}Ti targets exclusively via the (p,2p) reaction channel opened at a threshold energy of 12 MeV. This reaction was measured in the past by Levkovski up to 30 MeV. In this work the cross-section was investigated from 30 MeV up to 70 MeV, as can be seen in figure 4.15.

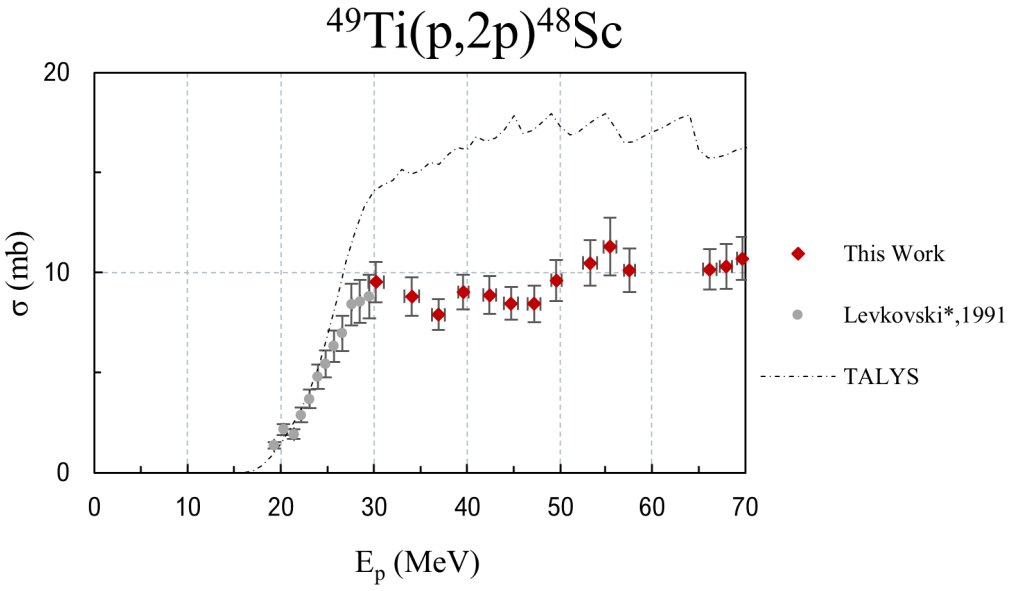

Figure 4.15: Cross-section trend of the ^{49}Ti(p,2p)^{48}Sc reaction.

The two mentioned datasets cover two different but close energy ranges: considering the correction by a factor of 0.8 needed for Levkovski's results, a compatibility can be noticed between the two experimental sets of data. Also in this case, TALYS overestimates the experimental data of approximately 40%.

Analysing all the Sc-isotopes proton-induced cross-sections for enriched ^{49}Ti targets it is immediately clear that an energy interval with the only ^{47}Sc production does not exist. ^{48}Sc and, more important, ^{46}Sc, the main contaminant, start to be produced even before ^{47}Sc. The only chance is to exploit the energy region where ^{46}Sc cross-section experiences its minimum. Unfortunately, in this energy region (30÷40/45 MeV) also the ^{44g,m}Sc starts to be produced. From figure 4.16 it can be better understood how ^{47}Sc is always produced simultaneously with many Sc-isotopes contaminants. Curves reported in this figure are the experimental data fits, obtained with the same spline interpolation method described in section 4.1, for all the possible Sc-isotopes produced using ^{49}Ti targets.

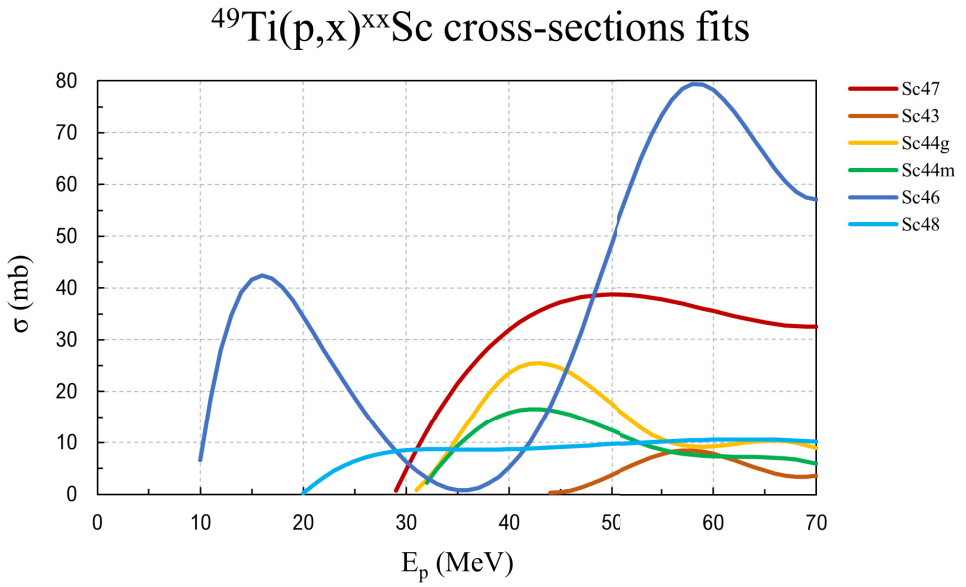

Figure 4.16: Comparison of the spline interpolations of the experimental cross-sections of ^{47}Sc (red line), ^{43}Sc (orange line), ^{44g}Sc (yellow line), ^{44m}Sc (green line), ^{46}Sc (blue line), and ^{48}Sc (light-blue line) to highlight the lack of a suitable energy range for a pure ^{47}Sc production.

Although a production pure enough for medical applications is not possible, the fact remains that these cross-sections represent a progress from a nuclear physics point of view since they were never measured before, at least in the energy range investigated in this work.

^{49}Ti(p,2n)^{48}V cross-section

For ^{48}V there is only one reaction channel responsible for its production. It is the (p,2n) which opens at the threshold energy of 13 MeV. Only two previous works presented some production cross-section data concerning this nuclear reaction: one is by Levkovski, and the other was performed by West Jr et al. Both the datasets coming from literature focused on the low energy region up to 30 MeV. As can be seen in figure 4.17, these two series of cross-section values are in agreement between each other, even if they present quite big uncertainties.

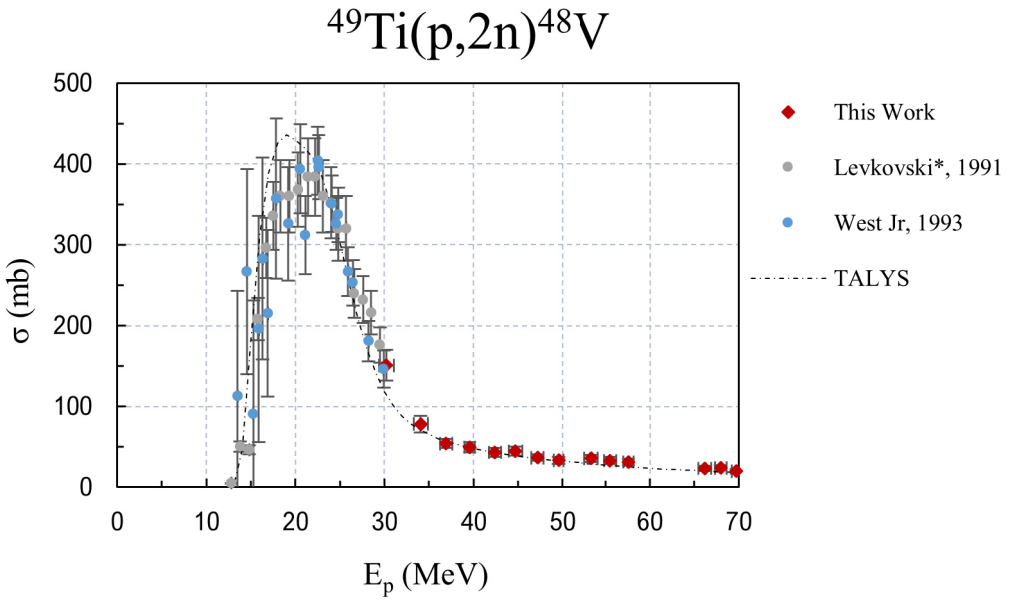

Figure 4.17: Cross-section trend of the ^{49}Ti(p,2n)^{48}V reaction.

These two old datasets seem to be compatible also with this work results, in fact, the only common beam energy, about 30 MeV, has corresponding cross-section values in agreement between each other. Moreover, the theoretical curve obtained using default parameters in the TALYS simulations is in a general accordance with the experimental results across all the energy region reported in figure 4.17.

4.3 Experimental cross-sections for proton beams on ^{50}Ti targets

It is important to remember that the enriched ^{50}Ti metallic powder used to manufacture the targets employed in the REMIX project experiments presents a strong

isotopic contamination, especially in ^{48}Ti (12.51%) and less in ^{46}Ti (1.69%), ^{47}Ti (1.29 %), and ^{49}Ti (1.41%). Considering the mean small variation obtained correcting the ^{49}Ti targets cross-sections for the 2.71% of ^{48}Ti contained, as first approximation the low contaminations of ^{46}Ti and ^{47}Ti in the target were considered irrelevant. Moreover, literature experimental data for ^{46,47}Ti(p,x) nuclear reactions are not available on EXFOR database [86]. However, ^{46}Ti and ^{47}Ti eventually contribute only to the production of ^{44m,g}Sc when using proton beams. Corrections for the low contaminant ^{49}Ti, instead, were performed. All the cross-sections regarding ^{49}Ti targets were fitted with the same spline interpolation method described in section 4.1, except for ^{43}K results. Production of ^{43}K in enriched ^{50}Ti targets was not considered so far because it is quite low, and so difficult to measure. Moreover, ^{43}Sc was not observed (E_{thres}= 44 MeV and low cross-section values), and the correction for the interference in the 372 keV γ peak was not needed. Corrections for all the other radioisotopes' cross-sections confirmed the expectation that they were not particularly influent considering the low percentage of ^{49}Ti. In fact, the cross-section values variations were included in the uncertainty bars. Different was the effect of the more abundant ^{48}Ti contamination which widely contributed to the enriched ^{50}Ti cross-sections. In summary, results concerning ^{50}Ti targets for energies between 22 MeV and 70 MeV, reported in table 4.6, are corrected for the presence of ^{48}Ti and ^{49}Ti in the targets and not for that of ^{46}Ti and ^{47}Ti. These results were obtained using the monitor reaction cross-section values reported in table 4.7, belonging to the IAEA recommended ^{nat}Ni(p,x)^{57}Ni nuclear reaction.

The case of values measured at the Bern cyclotron laboratory, below 22 MeV, was different. Up to 16 MeV only the ^{50}Ti(p,α)^{47}Sc reaction channel is open and corrections were not needed. At the highest energy available at the Bern hospital cyclotron, 18.2 MeV, also the presence of ^{48}Ti in the targets starts to be significant for ^{47}Sc production and thus the correction was needed. At the same energy, ^{46}Sc begins to be produced too, both by ^{50}Ti and ^{49}Ti. Corrections to derive the cross-section associate to ^{50}Ti were performed with formulas 3.18 and 3.19 described in section 3.3. As reminded already in section 4.1, those results did not need a monitor reaction since a precise measurement of the beam flux was possible.

Only few previous datasets are available in literature for the production cross-sections induced by protons on enriched ^{50}Ti targets. Actually, only Gadioli et al. measured most of the produced radionuclides, from 10 to 85 MeV [103]. The only other results available are the one concerning the ^{47}Sc and its main

Table 4.6: Cross-section results for ^{50}Ti(p,x)^{44m,g}Sc, ^{46}Sc, ^{47}Sc, ^{48}Sc, ^{48}V reactions.

Beam energy in ^{50}Ti foil $E \pm dE$ (MeV)	Cross-section of ^{44g}**Sc** $\sigma_x \pm d\sigma_x$ (mb)	Cross-section of ^{44m}**Sc** $\sigma_x \pm d\sigma_x$ (mb)	Cross-section of ^{46}**Sc** $\sigma_x \pm d\sigma_x$ (mb)	Cross-section of ^{47}**Sc** $\sigma_x \pm d\sigma_x$ (mb)	Cross-section of ^{48}**Sc** $\sigma_x \pm d\sigma_x$ (mb)	Cross-section of ^{48}**V** $\sigma_x \pm d\sigma_x$ (mb)
10.2 ± 0.4				6.1 ± 0.5		
12.3 ± 0.4				12.4 ± 1.0		
14.5 ± 0.4				22.0 ± 1.9		
16.0 ± 0.4				25.5 ± 2.1		
18.2 ± 0.4			0.4 ± 0.2	39.8 ± 3.4		
22.1 ± 0.9			18.1 ± 2.3	24.4 ± 2.6	0.04 ± 0.01	
26.9 ± 0.7	0.9 ± 0.1		56.3 ± 6.6	10.6 ± 1.2	0.43 ± 0.06	6.7 ± 0.8
30.3 ± 0.6	1.0 ± 0.1		62.2 ± 6.5	5.9 ± 0.6	1.0 ± 0.1	69.0 ± 6.8
33.4 ± 0.7	0.8 ± 0.1	0.32 ± 0.04	45.5 ± 5.8	3.7 ± 0.5	2.7 ± 0.3	102.4 ± 12.7
36.4 ± 0.5	2.6 ± 0.3	1.4 ± 0.2	41.3 ± 4.7	5.2 ± 0.6	7.9 ± 0.9	149.7 ± 16.1
39.6 ± 0.8	1.6 ± 0.2	1.0 ± 0.1	21.5 ± 2.4	4.2 ± 0.5	10.2 ± 1.2	123.6 ± 13.7
42.3 ± 0.7	1.8 ± 0.2	0.8 ± 0.1	13.3 ± 1.8	4.6 ± 0.6	11.7 ± 1.5	88.9 ± 11.3
44.7 ± 0.5	3.5 ± 0.5	1.8 ± 0.3	15.3 ± 2.4	9.9 ± 1.5	16.7 ± 2.5	88.0 ± 13.4
49.4 ± 0.8	6.0 ± 0.8	3.9 ± 0.5	14.6 ± 1.9	16.8 ± 2.1	16.1 ± 2.0	58.8 ± 7.3
51.7 ± 0.7	8.1 ± 1.0	5.2 ± 0.6	12.3 ± 1.5	19.9 ± 2.2	14.9 ± 1.7	47.9 ± 5.4
53.8 ± 0.5	14.2 ± 1.6	8.6 ± 0.9	17.9 ± 2.0	33.8 ± 3.6	19.5 ± 2.1	54.9 ± 5.8
55.8 ± 0.5	11.8 ± 2.0	7.2 ± 1.2	15.1 ± 2.6	28.0 ± 4.6	15.4 ± 2.5	35.4 ± 5.9
57.9 ± 0.8	17.0 ± 2.2	9.9 ± 1.2	19.3 ± 2.7	40.7 ± 4.7	19.7 ± 2.3	37.8 ± 5.1
61.8 ± 0.5	17.2 ± 2.0	10.9 ± 1.2	30.7 ± 3.9	46.4 ± 5.0	21.2 ± 2.3	36.1 ± 4.7
66.2 ± 0.7	8.7 ± 1.0	5.2 ± 0.6	24.2 ± 3.0	30.7 ± 3.4	14.7 ± 1.7	20.5 ± 2.6
69.8 ± 0.5	6.3 ± 0.7	4.4 ± 0.5	33.8 ± 4.1	30.5 ± 3.3	15.0 ± 1.6	20.2 ± 2.8

Table 4.7: Beam energy in the monitor foils and corresponding cross-section values of the ^{nat}Ni(p,x)^{57}Ni monitor reaction used in calculations.

Beam energy in ^{nat}Ni foil E ± dE (MeV)	Monitor reaction cross-section $\sigma_r \pm d\sigma_r$ (mb)
22.42 ± 0.91	148.7 ± 6.3
26.58 ± 0.74	182.5 ± 7.6
29.01 ± 0.76	162.8 ± 6.8
30.06 ± 0.56	148.6 ± 6.2
33.15 ± 0.71	116.5 ± 4.9
36.21 ± 0.56	96.4 ± 4.1
39.39 ± 0.77	85.4 ± 3.6
42.10 ± 0.68	80.5 ± 3.5
44.57 ± 0.56	77.8 ± 3.4
49.20 ± 0.76	74.5 ± 3.2
51.49 ± 0.68	73.3 ± 3.1
53.62 ± 0.56	72.2 ± 3.1
55.63 ± 0.56	71.3 ± 3.1
57.72 ± 0.75	70.3 ± 3.0
61.63 ± 0.56	68.7 ± 3.0
66.06 ± 0.74	66.5 ± 2.9
69.69 ± 0.55	65.5 ± 2.8

contaminant ^{46}Sc in the low proton energy region up to 18 MeV recently presented by Dellepiane et al. [66]. For some contaminants, namely ^{48}V and ^{44m}Sc, the results presented in this work constitute the first measurement.

^{50}Ti(p,x)^{44m,g}Sc cross-sections

The threshold energy for this reaction is 34 MeV with the (p,3nα) channel. Several other channels contribute to the ^{44m,g}Sc production above the threshold of 45 MeV. In figure 4.18, the results obtained in this work for the production of ^{44m}Sc are presented. This nuclear reaction was never measured before. Cross-section values are corrected for the presence of ^{49}Ti and ^{48}Ti in the enriched ^{50}Ti targets.

From the comparison with the TALYS simulation for ^{50}Ti targets an inaccurate description of the experimental data can be noticed: the maximum of the curve is largely underestimated and apparently shifted towards lower energies. But the most relevant aspect is that, even after corrections for ^{48}Ti and ^{49}Ti contaminations in the target, the presence of ^{44m}Sc was still detected below the threshold predicted by TALYS default, which is, differently from the cross-section

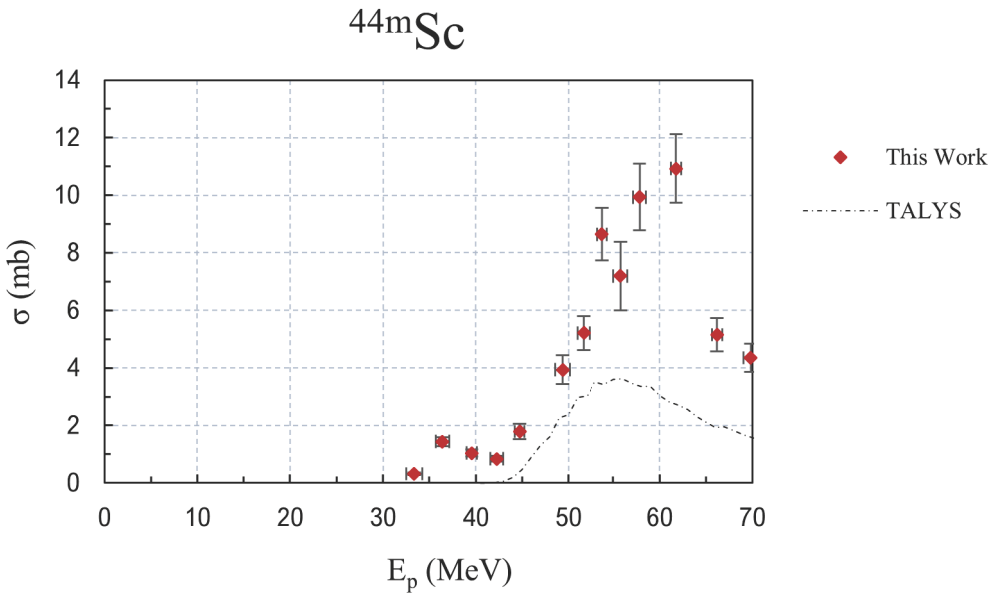

Figure 4.18: This work ^{44m}Sc cross-section results corresponding to enriched ^{50}Ti targets corrected for the presence of ^{48}Ti and ^{49}Ti compared to the theoretical trend of the ^{50}Ti(p,x)^{44m}Sc reaction.

values, usually reliable. This inconsistency is due to the contributions of ^{47}Ti and ^{46}Ti included in the enriched ^{50}Ti powder. From figure 4.19 it can be seen how in the energy range affected by this incongruity (33÷43 MeV), the TALYS ^{44m}Sc cross-section due to ^{46}Ti assumes considerably high values. From a further correction of the experimental cross-sections using theoretical values showed in figure 4.19 it was verified that the inconsistency is due to the contributions of ^{46}Ti and ^{47}Ti contaminations in the targets. However, cross-sections simulated with TALYS default are not always perfectly in agreement with experimental results, especially in the case of ^{44m}Sc, as can be noted from figures 4.3 and 4.12. For this reason, corrections performed with those theoretical values cannot be considered reliable. Anyway, they highlighted how even small percentage like 1.69% cannot always be neglected. Unfortunately, experimental cross-sections useful for corrections are not available in literature up to now. A collaboration with experts of the TALYS code is carried on to theoretically better describe the cross-sections due to ^{46}Ti and ^{47}Ti contributions, considering all the possible combinations of level densities and optical models, and eventually use those values for the corrections in the whole energy range up to 70 MeV. This work is currently still in progress.

For the objective of this thesis, the ^{44m,g}Sc cross-section results reported in table 4.6 (and in figure 4.18 for ^{44m}Sc) are compared to TALYS curves where a mixed target, ^{mix}Ti, was simulated. Cross-section values were already corrected

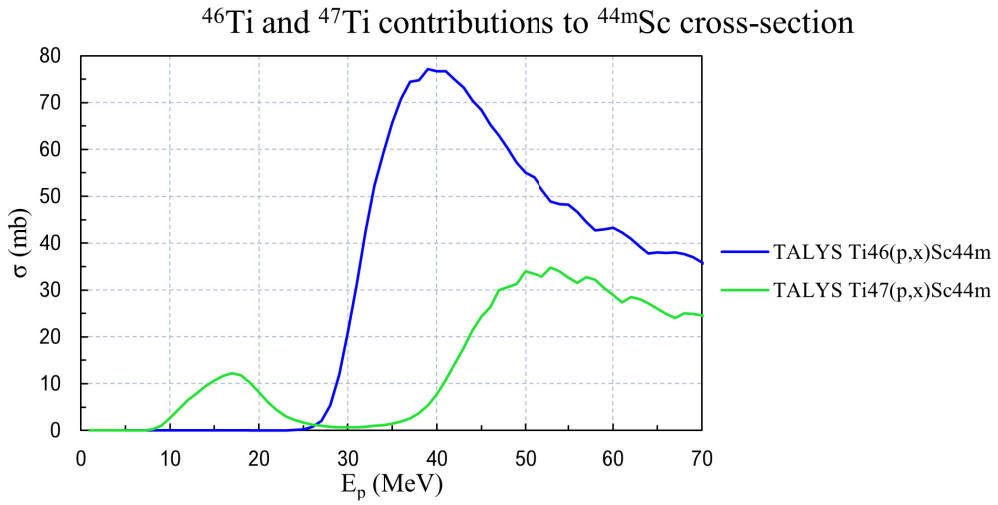

Figure 4.19: TALYS default code simulations for the production cross-section of ^{44m}Sc from ^{46}Ti (blue line) and ^{47}Ti (green line).

for ^{48}Ti and ^{49}Ti contributions, thus ^{mix}Ti was composed by 1.69% of ^{46}Ti, 1.29% of ^{47}Ti, and the remaining 97.02% of ^{50}Ti. This comparison is reported in figure 4.21 for ^{44m}Sc and in figure 4.22 for ^{44g}Sc, whose situation is analogous but with even higher contributions from ^{46}Ti and ^{47}Ti, as can be seen from figure 4.20.

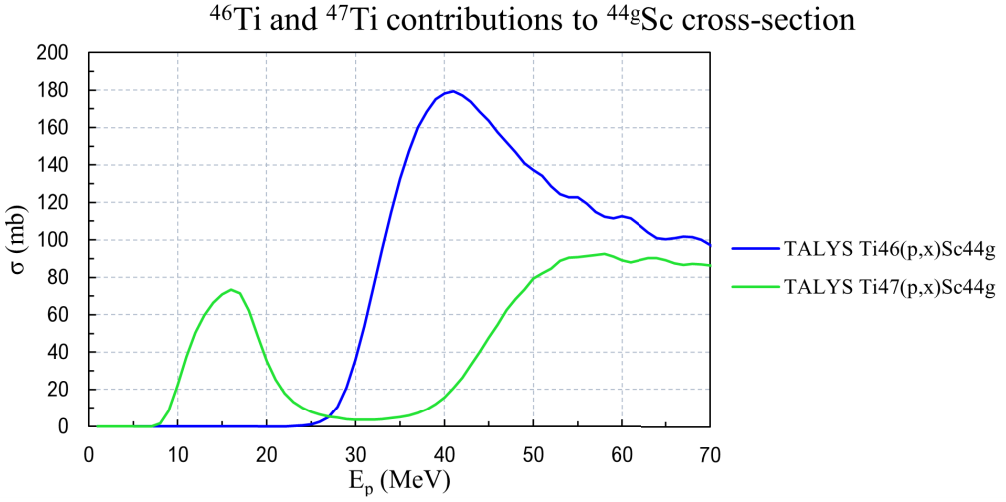

Figure 4.20: TALYS default code simulations for the production cross-section of ^{44g}Sc from ^{46}Ti (blue line) and ^{47}Ti (green line).

In figure 4.21, the experimental data at higher energies are still not well described by the TALYS curve which underestimates and slightly anticipates the higher peak. The small peak due to ^{46}Ti and ^{47}Ti contributions is now predicted and sufficiently well described by theory.

In figure 4.22, the ^{mix}Ti TALYS default simulation is now close to experimen-

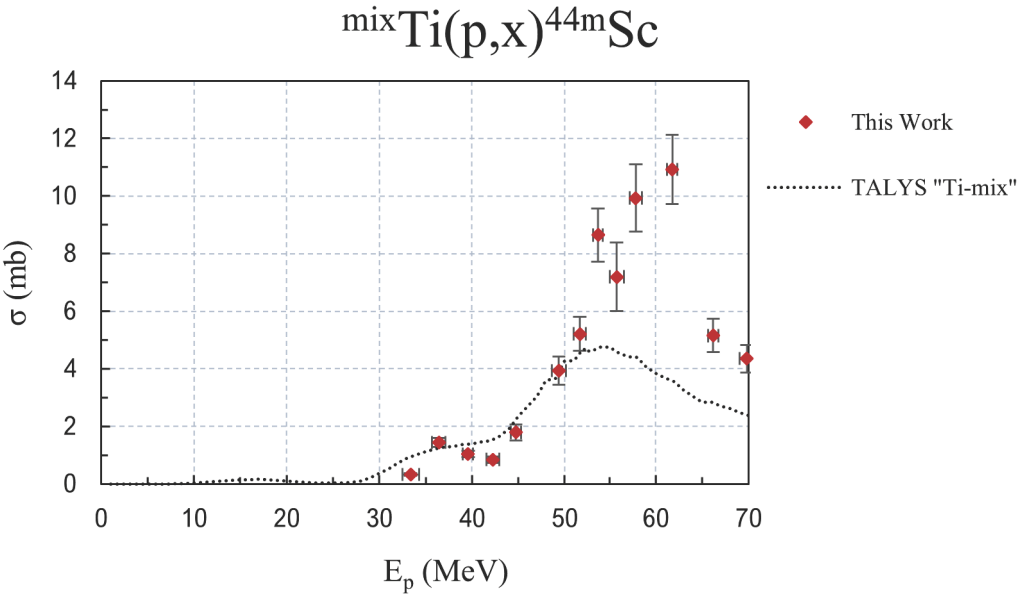

Figure 4.21: Cross-section trend of the ^{mix}Ti(p,x)^{44m}Sc reaction, where ^{mix}Ti is a target composed by 1.69% of ^{46}Ti, 1.29% of ^{47}Ti, and 97.02% of ^{50}Ti.

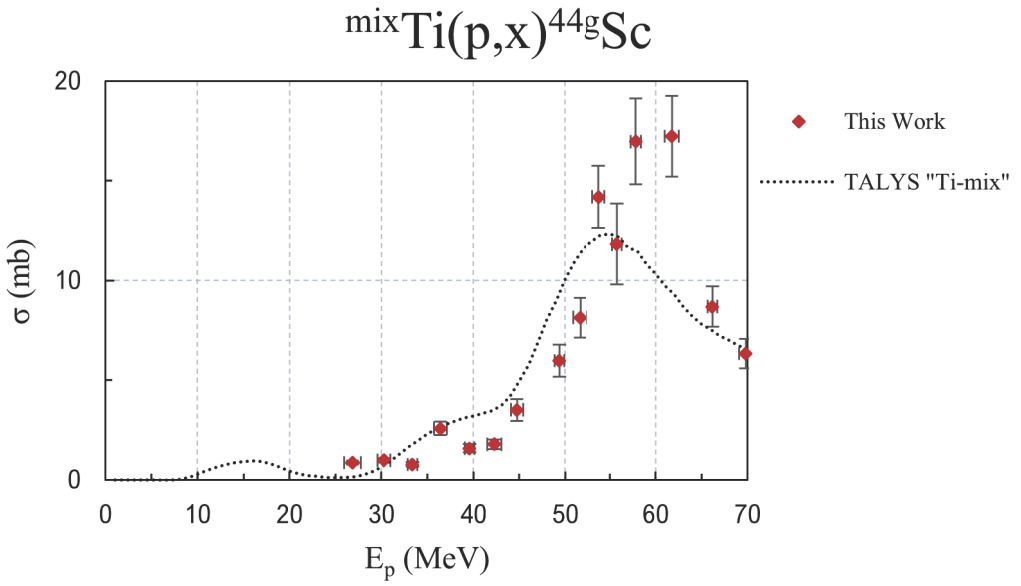

Figure 4.22: Cross-section trend of the ^{mix}Ti(p,x)^{44g}Sc reaction, where ^{mix}Ti is a target composed by 1.69% of ^{46}Ti, 1.29% of ^{47}Ti, and 97.02% of ^{50}Ti.

tal values. Cross-section data below 43 MeV, due to ^{46}Ti and ^{47}Sc contaminations in the target, are predicted by theory. However, theoretical curve does not reproduce experimental cross-section perfectly. In fact, in the energy region above 50 MeV, the peak is underestimated and slightly anticipated by theoretical simulations. Actually, Gadioli et al. measured this reaction in the past but their results

are not included here since this work corrections for isotopic contaminations in the target are not concluded yet. A comparison would not have a scientific relevance.

^{50}Ti(p,x)^{46}Sc cross-section

The presence of ^{46}Ti and ^{47}Ti in the target is no longer a problem for ^{46}Sc and heavier produced radionuclides. All the 7 reaction channels leading to the production of ^{46}Sc from ^{50}Ti targets have a threshold energy included in the range 13÷42 MeV. This reaction was measured by Gadioli et al. up to 85 MeV and one experimental point was recently presented by Dellepiane et al. at about 18 MeV, where the experimental ^{46}Sc activation function begins. Those results are reported in figure 4.23, together with this work results, corrected for the presence of ^{48}Ti and ^{49}Ti in the targets, and TALYS simulated curve.

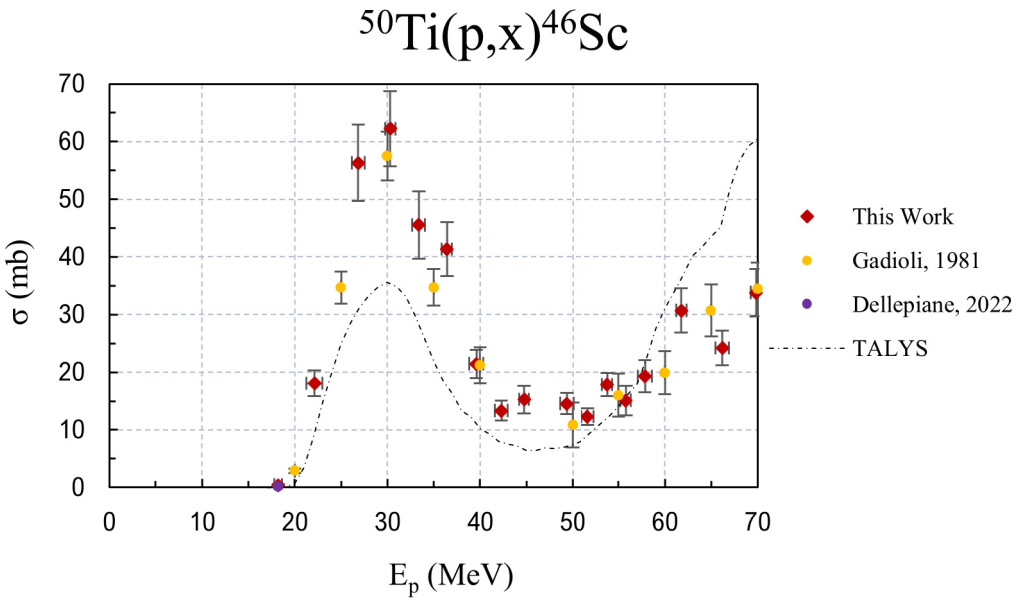

Figure 4.23: Cross-section trend of the ^{50}Ti(p,x)^{46}Sc reaction.

Net of some fluctuations, a good agreement can be observed between all the experimental datasets. The theoretical curve, instead, underestimates the experimental points up to 50 MeV. At the peak at 30 MeV this underestimation reaches a value of about 40%. On the other hand, above 60 MeV the theoretical curve tendency is to overestimate the experimental points up to about 40% (maximum discrepancy at 70 MeV).

^{50}Ti(p,x)^{47}Sc cross-section

The threshold energy of the first reaction channel contributing to the production of ^{47}Sc, namely the (p,α) one, is quite low, approximately 2 MeV. This reaction generates the first peak that can be seen in figure 4.24. Some other channels are then open starting from the (p,pt) one with a threshold energy of 22 MeV up to the last one, the (p,2n2p), which has a threshold energy of 31 MeV. Results by Gadioli et al. and by Dellepiane et al. are available in literature and reported in figure 4.24. The latter dataset covers only the proton energy range up to 18.2 MeV, and it disagrees with the former one.

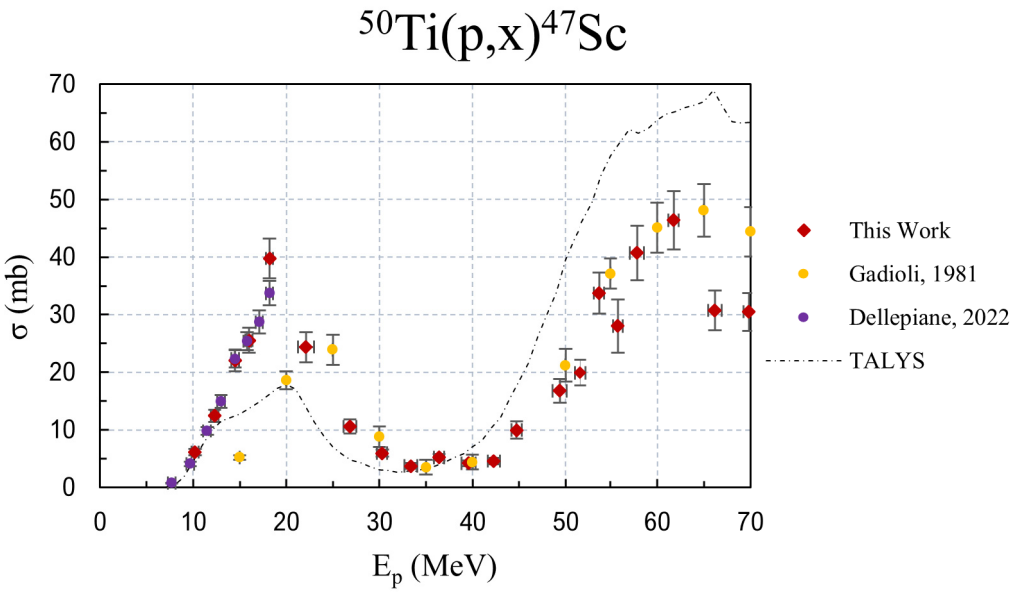

Figure 4.24: Cross-section trend of the ^{50}Ti(p,x)^{47}Sc reaction.

This work results up to 18.2 MeV are in agreement with the newest results by Dellepiane et al., while above 18.2 MeV there is a quite good accordance with experimental points by Gadioli et al., except for the highest energy region above 65 MeV. There, a fluctuation towards lower cross-section values can be observed. In fact, the cross-section corresponding to the two highest energies investigated (66.2 MeV and 69.8 MeV) are not perfectly following the trend described by the other results for most of the produced radionuclides (see figures 4.21, 4.22, 4.23, and 4.25). This effect can be eventually caused by the evaluated thickness of the targets: if the effective thickness is lower than the evaluated one the actual cross-section will be higher. However, this cannot be verified since further thickness analysis cannot be done as long as the targets are active, but measurements can

be eventually repeated with new targets.

The theoretical curve well reproduces the general trend of the experimental points but it underestimates the low energy peak and, at the same time, it overestimates the experimental datasets of about 30% above 40 MeV.

^{50}Ti(p,x)^{48}Sc cross-section

The reaction channels able to produce ^{48}Sc when using proton beams on ^{50}Ti targets are only three, namely (p,^{3}He) with E_{th}= 15 MeV, (p,pd) with E_{th}=20 MeV, and (p,n2p) with E_{th}= 23 MeV. The ^{50}Ti(p,x)^{48}Sc reaction was previously measured by Gadioli et al. and their results are reported in figure 4.25 for comparison with this work results.

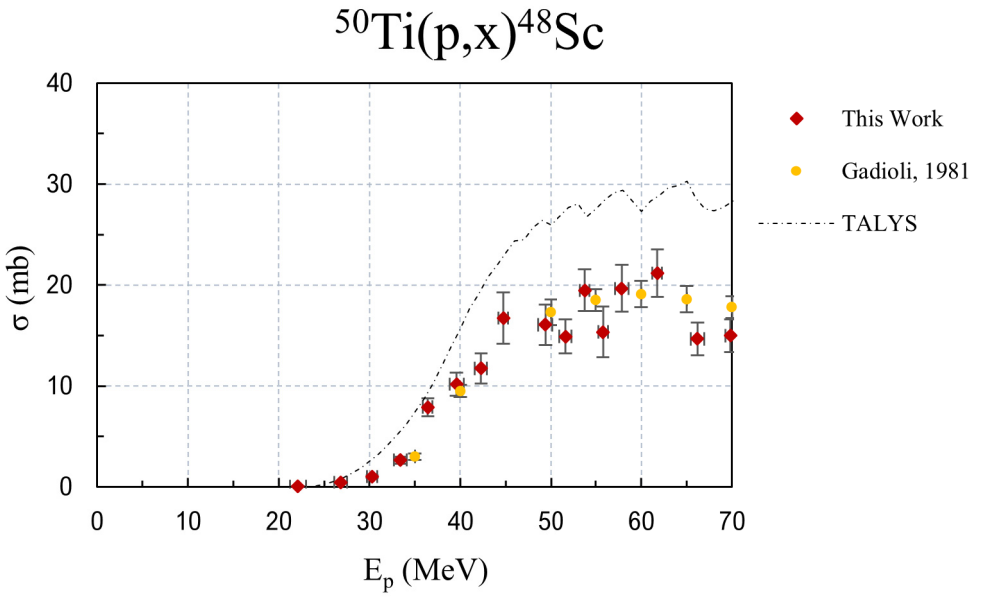

Figure 4.25: Cross-section trend of the ^{50}Ti(p,x)^{48}Sc reaction.

A good agreement can be observed in the whole energy range between this new results and the previous dataset. TALYS simulation with default parameters reproduces quite well the general experimental cross-section trend but overestimates the experimental values up to about 30% in the highest energy range. This overestimation was encountered also when using enriched ^{49}Ti, as can be seen from figure 4.15.

Considering all the Sc-isotopes produced by protons impinging on ^{50}Ti targets a good energy interval where only ^{47}Sc is produced can be individuated, as can be seen from figures 4.21÷4.25. This energy interval is $E_p < 18$ MeV. When

corrections for the ^{44m,g}Sc produced radionuclides will be completed, TTYs in some different energy ranges will be calculated with the objective to assess if also a wider energy range can be exploited to enhance the ^{47}Sc production, always keeping the purity high, as required for medical applications.

^{50}Ti(p,3n)^{48}V cross-section

Only one nuclear reaction channel can produce ^{48}V from ^{50}Ti targets, namely the (p,3n) channel, and it has a threshold energy of 24 MeV. The cross-section deriving from this reaction channel is reported in figure 4.26.

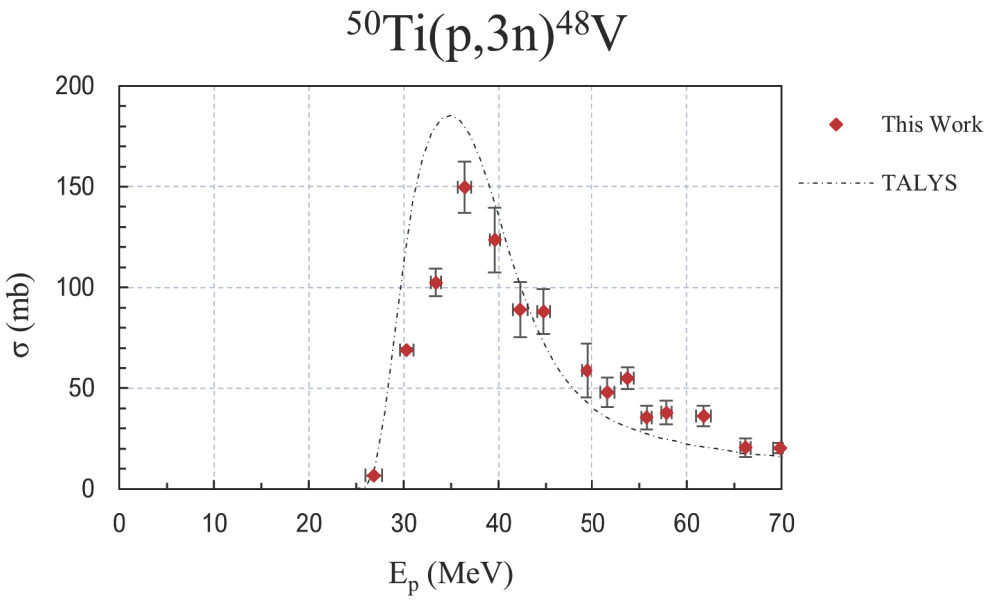

Figure 4.26: Cross-section trend of the ^{50}Ti(p,3n)^{48}V reaction.

Experimental results of this work are well reproduced by the theoretical simulation performed with TALYS default parameters, except for the peak which is overestimated. The value assumed by theoretical curve is between 20% and 45% higher than the experimental one. More experimental points in this lower energy region of the curve would better describe the peak and consequently it would be possible to better estimate the disagreement between experimental and theoretical trends.

This nuclear reaction was never measured before, for this reason results were compared only to TALYS theoretical estimations in figure 4.26. Few other experimental measurements are advisable to confirm these experimental results. This recommendation is valid also for other nuclear reaction cross-sections considered

in this chapter.

At the start of the INFN-LNL new installed cyclotron, within the SPES program, some of these measurements can be repeated.

4.3.1 Patent request for optimised ^{47}Sc production

On September 8^{th} 2023, I deposited a patent in collaboration with my Ph.D. supervisors Dr. Liliana Mou and Dr. Gaia Pupillo and the TALYS experts Dr. Luciano Canton and Dr. Francesca Barbaro based on the results obtained with the PASTA and REMIX projects. The INFN patent request number is 102023000018477 (it is not available online yet). A multi-layer target is proposed in this patent to maximize the production of ^{47}Sc while minimizing the co-production of ^{46}Sc and ^{48}Sc. The first layer is composed of a ^{nat}V target thick enough to cover the energy range 35÷22 MeV. The following second layer material is enriched ^{50}Ti to exploit the 22÷9 MeV energy region where the ^{50}Ti(p,α)^{47}Sc nuclear reaction begins to be convenient over the ^{nat}V(p,x)^{47}Sc one for the purpose of producing ^{47}Sc. With this configuration, the production yields reported in table 4.8 can be obtained, assuming 1 h irradiation time and 1 μA beam current, for ^{47}Sc and its contaminants ^{46}Sc and ^{48}Sc. Those values assure a RNP at the EoB higher than 99%.

Table 4.8: ^{47}Sc, ^{46}Sc and ^{48}Sc yields obtained for the multilayer target considering a 1 h irradiation time and 1 μA proton beam current.

	^{47}Sc yield (MBq)	^{46}Sc yield (MBq)	^{48}Sc yield (MBq)
^{50}Ti layer (9÷22 MeV)	8.8	0.05	0.001
^{nat}V layer (22÷35 MeV)	4.2	0.02	0.0005
Tot (9÷35 MeV)	13.0	0.07	0.0015

In comparison to a single layer target composed by only ^{nat}V target and covering the whole energy range 35÷9 MeV, the proposed multi-layer configuration allows to increase the production of about 300%, with a meaningless degradation of the RNP which remains higher than 99%.

Cross-sections' measurements are an essential element in the investigation of new or alternative possible production routes. They can give a first indication on the possible energy ranges to maximize the production while minimizing the

co-production of contaminants. However, they are not sufficient. Dosimetric evaluations are also needed to complete the information through the estimation of the absorbed doses to the organs and effective dose determined by the use of a specific radiopharmaceutical. Yields calculations, starting from experimental cross-sections, are the fundamental ingredient for dosimetric evaluations. Thus, the complementarity of dosimetry and cross-section measurements is evident and each one is indispensable for the investigation of new production routes of any innovative medical radionuclide.

Chapter 5

Dosimetric evaluations for the ^{47}Sc-cm10 radiopharmaceutical

The estimation of the radiation dose imparted to a patient through the administration of a diagnostic or therapeutic radiopharmaceutical is essential in nuclear medicine to evaluate the risks and the benefits arising from its use [119]. The main quantity used to quantify the amount of radiation received is the *absorbed dose*, D. It is defined as the energy absorbed per unit mass of irradiated medium:

$$D = \frac{dE}{dm} \tag{5.1}$$

where dE is the energy deposited by ionizing radiation in a material volume of mass dm. Its unit in the International System of Units is the *gray* (Gy), which corresponds to J/kg.

However, a biological effect can be caused by different kinds of radiation. This is taken into consideration by the quantity *equivalent dose*, $H_{T,R}$. It is defined as the absorbed dose modified by a factor which takes into account the effectiveness of the radiation in producing biological damage:

$$H_{T,R} = w_R \cdot D_{T,R} \tag{5.2}$$

where $D_{T,R}$ is the absorbed dose delivered by radiation of type R averaged over a tissue or organ T, while w_R is the weighting factor for radiation type R (dimensionless). The values recommended for the quantity w_R by the International Commission on Radiological Protection (ICRP) are reported in table 5.1. They are from the ICRP Publication 103 [120]. According to the w_R values, for photons and electrons, absorbed dose (in Gy) and equivalent dose (in Sv) coincide. For

other particles, equivalent dose is a multiple of the absorbed dose.

Table 5.1: Weighting factor values recommended by ICRP Publication 103 for different radiation types.

Radiation type	w_R
Photons	1
Electrons Muons	1
Protons Charged pions	2
α particles Fission fragments Heavy ions	20
Neutrons	$\begin{cases} 2.5 + 18.2e^{-[ln(E_n)]^2/6} & \text{for } E_n < 1MeV \\ 5.0 + 17.0e^{-[ln(2E_n)]^2/6} & \text{for } 1MeV < E_n < 50MeV \\ 2.5 + 3.25e^{-[ln(0.04E_n)]^2/6} & \text{for } E_n > 50MeV \end{cases}$

In principle absorbed dose and equivalent dose have the same unit of measure. In practise, a specific unit is used for equivalent dose, the *sievert* (Sv).

To take into account also the radiosensitivity of each type of tissue, organ or system an additional dimensionless weighting factor is used, w_T. It represents the probability of expressing fatal cancers or genetic defects for each kind of tissue or organ. The w_T values, recommended in ICRP Publication 103 [120], are reported in table 5.2. The sum of the organs' equivalent doses, each multiplied by the corresponding weighting factor, returns the effective dose, E:

$$E = \sum_T H_T \cdot w_T \tag{5.3}$$

where

$$H_T = \sum_R H_{T,R}. \tag{5.4}$$

The weighting factors w_T are derived from statistical studies on the expression of any effect in radiation exposed populations. For this reason, and due to the involved uncertainties, there are several opinions about the relevance of the effective dose quantity in nuclear medicine. By accepting that it should never be used in radiation therapy, as it is related to the evaluation of the stochastic risks consequent to exposure, and that it should not be used to evaluate the individual risk, but it should be applied to a population, its usefulness is in the possibil-

Table 5.2: Weighting factor values recommended by ICRP Publication 103 for different organs or tissues.

Organ or tissue	w_T
Red bone marrow Colon Lung Stomach Breasts Others	0.12
Gonads	0.08
Bladder Oesophagus Liver Tyroid	0.04
Bone surface Brain Salivary glands Skin	0.01
Total	1

ity to compare doses due to radiopharmaceuticals with different distribution and retention patterns in the body.

To estimate, in practise, the amount of energy absorbed per unit mass of each tissue, the equation 5.1 can be expressed as:

$$D = \frac{k\tilde{A}\sum_i y_i E_i \phi_{i,(T \leftarrow S)}}{m} \tag{5.5}$$

where k is a proportional constant converting energy (MeV) in dose (Gy), equal to $1.6 \cdot 10^{-19}$ when expressed in $\frac{Gy \cdot kg}{MBq \cdot s \cdot MeV}$, y is the number of radiations with energy E emitted per nuclear transition, E is the energy per radiation (MeV), ϕ is the fraction of energy emitted by the source S that is absorbed in the target T, known as *absorbed fraction*, which, for example, conventionally assumes the value 1.0 for electrons and beta particles whose energy is typically absorbed, and m is the mass of the target organ (kg). $\tilde{A}$ is the number of nuclear transitions, also known as *cumulated activity* (MBq·s), corresponding to the time integral of the activity.

Equation 5.5 is the one implemented in dosimetric software to calculate the absorbed dose for each organ, and the derived effective dose consequently, when a specific radiopharmaceutical is administered to a patient. It is expressed with different mathematical formalisms depending on the specific software but the

meaning is always the same. The quantities involved in this equation represent the input parameters to enter in the software for a numerical solution:

- y_i and E_i are the quantities related to the radionuclide in question. Decay data of a large number of radionuclides can be found in the ICRP Publication 107 [121], but they are also available online [7].

- $\phi_{i,(T\leftarrow S)}$ is a quantity depending on the type of radiation emitted but also on the human body modelling. They are discussed in the ICRP Publication 133 [122], where they are referred to as SAFs (Specific Absorbed Fractions), actually corresponding to $\frac{\phi_i}{m}$.

- m is a human body model dependent quantity. The reference computational phantoms are described both in ICRP Publication 89 [123] and in ICRP Publication 110 [124].

- $\tilde{A}$ is a quantity extracted from biokinetic data for a specific radiopharmaceutical. It is usually derived from observations of the radiopharmaceutical distribution and clearance in body organs of animals or human subjects. Normally, cumulated activity is used normalized to administered activity, A_0, becoming the so-called TIACs (Time Integrated Activity Coefficients), also indicated as $\tilde{a}$ (MBq·s/MBq).

The first four quantities (y_i, E_i, $\phi_{i,(T\leftarrow S)}$, and m) are conventionally grouped in the parameter *S-value*, defined as the absorbed dose rate to target region per unit activity in source region. S-values are usually already implemented in dosimetric software. TIACs, instead, come from biodistribution studies and their derivation from activities registered in animal organs is described in section 5.1. Those are the two elements needed to implement dose estimation formalism in dosimetry software.

5.1 TIACs derivation

Even if human studies are always preferable for dose estimation, the gathering of animal data is an essential first step for a preliminary indication. Data consist in measured activities as a function of time in the animal organs identified as source regions, where the radiopharmaceutical concentrates, and in the rest of the body (sometimes generally indicated as muscle), which should be considered a source

region too [125]. The animals used are typically mice and, for statistics, more than three mice should be sacrificed for each time point of radiopharmaceutical biodistribution study. Activity measurements should be repeated to properly characterize the behaviour of the radiopharmaceutical in each organ, which can be divided in three phases: uptake, retention, and elimination. A prediction of the behaviour should also be taken into account for a precise timing of the measurements: the objective is to have more than one measurement for each phase, if possible, thus it is important to approximately know the phases' duration. Considered organs are usually weighted to express activity measurements' results as percentages of the injected activity per gram of tissue, $\%IA/g$.

Extrapolation of animal data to humans is not an exact science. Many different methods have been investigated and no one proved to be superior to the others. One of the most popular methods, used in this thesis work, is based on the following formula [119]:

$$\left(\frac{\%IA}{organ}\right)_{human} = \left[\left(\frac{\%IA}{g}\right)_{animal} \cdot \left(TB_{weight}\right)_{animal}\right] \cdot \left(\frac{O_{weight}}{TB_{weight}}\right)_{human} \tag{5.6}$$

where $\left(\frac{\%IA}{g}\right)_{animal}$ is the above-mentioned data coming from animal biodistribution studies, $\left(TB_{weight}\right)_{animal}$ is the total body weight of the animal (kg), O_{weight} represents the weight of each considered organ (kg) in the human body, whose value are reported in [123], as it also is for the human total body weight (kg), $\left(TB_{weight}\right)_{human}$, which for the reference adult male phantom takes the value 70 kg.

All the organs' extrapolated $\frac{\%IA}{organ}$ as a function of the time need to be fitted to obtain the TIACs. A three-exponential function is the fitting curve better reproducing the trend:

$$\frac{\%IA}{organ}(t) = \sum_{i=1}^{3} A_i e^{-a_i t} \tag{5.7}$$

where each of the three exponential terms represents a phase between uptake, retention and elimination of the radiopharmaceutical. The uptake phase in the organs is characterized by a negative value of the A_i coefficient, while retention and elimination phases are represented by positive values. The exception is when considering blood as the organ. Since the radiopharmaceutical is generally injected directly in the bloodstream, the uptake can be considered immediate, so

% IA (t=0) =100%.

In this work, fitting procedure was performed using the software Origin v.2023b (OriginLab Corporation, Northampton, Massachusetts, USA) with data extrapolated from biodistribution studies performed on mice with a ^{47}Sc-labelled DOTA-folate conjugate, the ^{47}Sc-cm10 [126]. DOTA-folate conjugate cm10 binds selectively to folate receptors expressed on many tumour types [126]. In Origin there is the possibility to introduce user defined fitting curves. For the aim of this work the equation 5.7 was incorporated in the software. In figure 5.1 an example of obtained fits is reported for kidney and blood. The representation of these two organs results was chosen to highlight how, for blood, the uptake phase is missing since the radiopharmaceutical is injected directly in a tail vein, but also how in the kidneys the clearance is slower than in blood.

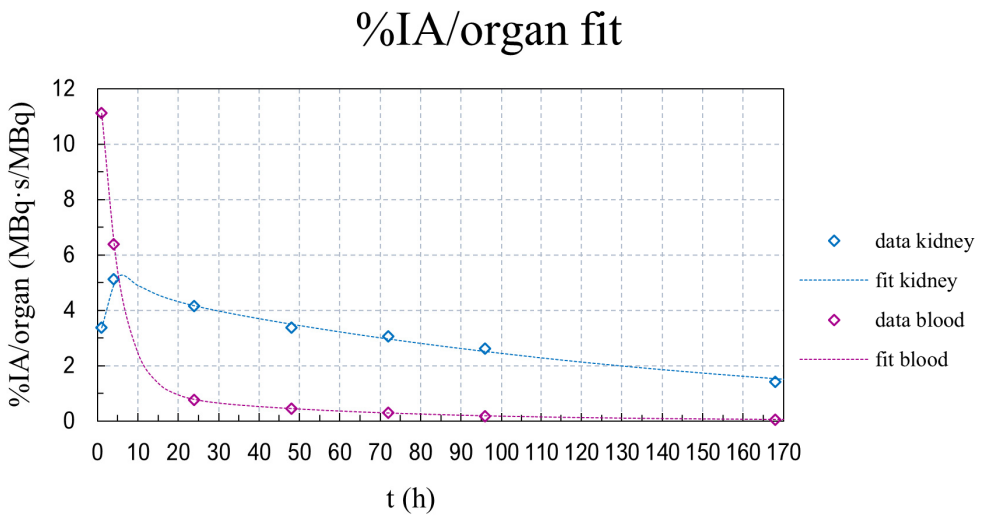

Figure 5.1: Fit example of the %IA/organ extrapolated from biodistribution studies on mice for two organs. Blue line is the fit for kidney data (blue points). Purple line is the fit for blood data (purple points).

From the parameters A_i and a_i obtained with the fitting procedure, TIACs for each organ can be calculated as:

$$TIAC = \sum_{i=1}^{3} \frac{A_i}{a_i + \lambda_p} \cdot \frac{1}{100} \tag{5.8}$$

where λ_p is the decay constant of the radionuclide in the radiopharmaceutical. The TIACs obtained are reported in table 5.3. They were calculated for the radionuclide ^{47}Sc, but also for ^{46}Sc and ^{48}Sc which are co-produced contaminants that may be present in the final solution, as it is when the production route via

^{nat}V targets bombarded with protons is considered. They have to be taken into account since they compete with ^{47}Sc in the labelling procedure, and so they can be introduced in the human body contributing to the dose imparted to a patient. Dosimetric evaluations are exploited to assess the maximum quantity of contaminants tolerable for a patient that consequently can be accepted in the produced final solution.

Table 5.3: TIACs (or number of disintegrations) in source organs for ^{47}Sc-cm10 and eventual contaminants ^{46}Sc-cm10 and ^{48}Sc-cm10, considering an adult male reference phantom [123].

Organ or Tissue	TIACs $\left(\frac{MBq \cdot h}{MBq}\right)$		
	^{47}Sc-cm10	^{46}Sc-cm10	^{48}Sc-cm10
Blood	0.45	0.46	0.45
Lung	0.32	0.64	0.24
Spleen	0.04	0.21	0.02
Kidney	3.13	6.70	2.13
Stomach	0.04	0.12	0.03
Intestines	0.03	0.06	0.02
Liver	1.60	3.17	1.14
Salivary glands	0.10	0.26	0.07
Muscle	7.42	12.43	5.49
Bone	1.08	4.04	0.67

Quantities in table 5.3 are given as input in dosimetric software to evaluate absorbed doses to organs and effective dose to the whole body which can be attributed to ^{47}Sc or to the co-produced contaminants ^{46}Sc and ^{48}Sc present in the solution. It is important to remember that the estimations performed with those software have not the ultimate aim of medical applications. They are just a preliminary evaluation helpful to establish the most promising production conditions considering the dose administered to a patient in different scenarios. Before moving to medical employment of the radiopharmaceutical, biodistribution studies and additional evaluations in clinical trials involving humans are necessary.

5.2 Internal dosimetry software

In this Ph.D. work two are the software used to perform dosimetric calculations: MIRDCalc v1.1 (University of Florida, Gainesville, Florida, USA, and Memorial Sloan Kettering Cancer Center, New York, USA) [127] and IDAC-Dose 2.1 (Umeå University, Sweden) [128]. At the moment, a version 2.1 of MIRDCalc software has been released. Updates are few and largely cosmetic, leaving unchanged

results presented in this thesis.

MIRDcalc is a free Excel-based software [130]. It gives the possibility to choose between 12 (6 male and 6 female) computational reference phantoms, paediatric or adult. Those phantoms are modelized according to ICRP Publication 143 [129] and ICRP Publication 110 [124], respectively. The mathematical format used is the voxel phantom, meaning that the human anatomy is represented in detail as much as possible with the help of a large number of small volume elements, the voxels [124]. Adult phantoms organ masses used in the software are described in ICRP Publication 89 [123]. Masses of the target organs can eventually be modified in the software. An important lack of MIRDcalc, for the purpose of this thesis work, is the absence of ^{48}Sc in the list of selectable radionuclides.

IDAC-Dose 2.1 is a free dosimetry software based on MATLAB [128]. This software has the same references as MIRDcalc for S-values computation and human body modelling. However, in IDAC-Dose only the adult male and female reference phantoms are available. They are always described following the voxel format, so they are identical to the two adult reference MIRDcalc phantoms. In IDAC-Dose, ^{48}Sc is present as possible radionuclide labelling of the radiopharmaceutical.

These two software were used to perform dosimetric calculations for the DOTA-folate conjugate cm-10 radiolabelled with ^{47}Sc, considering the possible contaminations of ^{46}Sc and ^{48}Sc in some proton beam energy intervals when using ^{nat}V targets. Those dosimetric evaluations were previously performed with a different software, OLINDA 2.1.1 [131, 132]. Results obtained with this software can be found in [133].

OLINDA/EXM (Hermes Medical Solutions, Stockholm, Sweden) is a purchasable software written in Java. The main difference of this software is the use of RADAR (RAdiation Dose Assessment Resource) defined reference phantoms [134] that determines the computation of different S-values. The development of the reference phantoms series in the software code is based on the NURBS (Non-Uniform Rational B-Spline) modelling technique which allows a more realistic rendering of human body. Figure 5.2 (a) shows the adult male NURBS model used in OLINDA compared to the voxel phantom model used in MIRDcalc and IDAC-Dose (figure 5.2 (b)). In figure 5.2 (c) there is the last evolution of the ICRP phantoms, called Mesh-Type Reference Computational Phantoms (MRCPs), and described in the recent ICRP Publication 145 [135]. Those phantoms, not introduced in software yet, will overcome the limits of the voxel format in the

modelling of the small structures of the tissues (e.g. lens of the eye), and so can be implemented in more precise dose calculations.

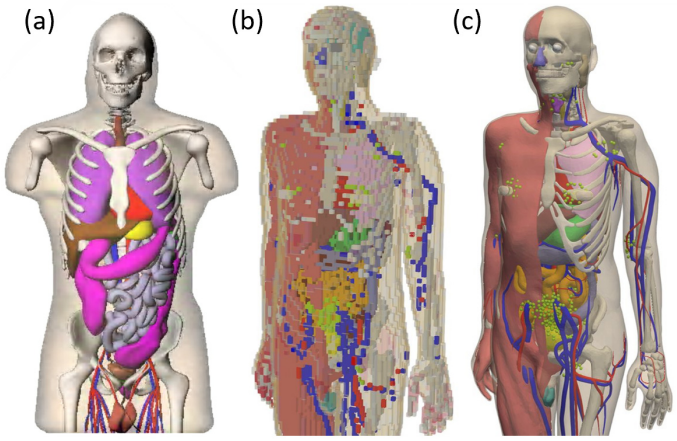

Figure 5.2: Adult reference male phantom models: (a) NURBS model based on RADAR phantoms used for example in OLINDA software; (b) voxel model based on ICRP Publication 110 phantoms [124] used, for example, in MIRDcalc and IDAC-Dose software; (c) MRCPs archetypal model based on the latest ICRP Publication on phantoms [135].

The RADAR phantoms and the ICRP Publication 110 phantoms are based on the same reference organ parenchyma masses but have different organ shapes and positioning [130]. Moreover, RADAR phantoms do not include a blood source organ and do not take into account the organ fractional blood content. Some issues are also linked to the muscle source organ. This tissue in not included in the OLINDA phantom model. In dosimetric evaluations performed with OLINDA 2.1.1 software for the ^{47}Sc-cm10 radiopharmaceutical, where the radionuclide is produced via the ^{nat}V(p,x) nuclear reaction, the blood TIAC was assigned to the heart contents source organ, and the muscle TIAC was assigned to the whole-body source organ. Since no specific indications were given in the biodistribution data, the TIAC obtained for intestines was divided in the four components constituting the human intestine, namely left colon, right colon, small intestine, and rectum, proportionally to their masses [133]. The bone TIAC, instead, was assigned to bone surface when considering a radionuclide with a half-life shorter than 10 days (^{47}Sc and ^{48}Sc in this case), and was given to bone volume for radionuclides with half-life longer than 10 days (^{46}Sc), as suggested in ICRP Publication 30 [136].

The bone TIAC attribution to surface or volume and the subdivision of the intestines TIAC in its components was kept also in the dose calculations performed with MIRDcalc and IDAC-Dose software in the context of this Ph.D. activities. However, the phantom models used in these two software give the possibility to

choose both blood and muscle as source organs. More precisely, in IDAC-Dose heart contents is not available as source organ, so only blood was a reasonable choice. For these reasons, many tests were made assigning blood and muscle TIACs to blood and muscle source organs, respectively, or to heart contents and rest of the body to reproduce as similar as possible OLINDA software conditions. During these tests, TIACs used in OLINDA dose calculations, that can be found in [133], were used to limit the initial differences only to the phantom models. Only the adult male phantom was used in all the software. The tests were limited to beam energies up to 35 MeV where, in addition to ^{47}Sc, only the contaminant ^{46}Sc was produced, since in MIRDcalc there is not the possibility to simulate the dose administration due to the radionuclide ^{48}Sc. The aim of these tests is to evaluate the influence of the source organs selection in the absorbed doses to the target organs and in the effective dose, considering the different possible radionuclides that can be present in the radiopharmaceutical final solution.

In table 5.4 are reported the results of the tests conducted considering the DOTA-folate conjugate cm10 radiolabelled exclusively with ^{47}Sc, compared to the OLINDA outputs, presented in a previous publication [133]. The blood and muscle TIACs allocation in each test is:

- TEST 1: blood TIAC is divided between heart contents (10%) and rest of body (90%), and muscle TIAC is given to muscle source organ.
- TEST 2: blood TIAC is given to blood source organ, and muscle TIAC is given to muscle source organ.
- TEST 3: blood TIAC is divided between heart contents (10%) and rest of body (90%), and muscle TIAC is assigned to rest of body source organ.
- TEST 4: blood TIAC is given to blood source organ, and muscle TIAC is assigned to rest of body source organ.

TEST 3 is the one reproducing the same TIACs distribution used in OLINDA software. From results in table 5.4 it can be noticed that this configuration in particular returns results more similar to OLINDA ones, especially when considering the effective dose E that is almost the same for MIRDcalc TEST 3 and OLINDA. However, for most organs, also TEST 4 shows results compatible with OLINDA ones. This means that, while the allocation of the blood TIAC to blood or heart contents source organs produces relatively small effects (small differences between TEST 1 and TEST 2, and between TEST 3 and TEST 4), the choice of

Table 5.4: Absorbed doses to various main organs and effective dose obtained with MIRDcalc 1.1 for different configurations, compared to OLINDA 2.1.1 results, for ^{47}Sc-cm10.

Organ or Tissue	MIRDcalc (mGy/MBq)				OLINDA (mGy/MBq)
	TEST 1	TEST 2	TEST 3	TEST 4	
Adrenals	0.0301	0.0311	0.0386	0.0406	0.0362
Small intestine	0.00805	0.01	0.0153	0.018	0.0191
Stomach	0.0139	0.0159	0.0208	0.0235	0.0235
Heart wall	0.00793	0.00974	0.0165	0.0197	0.0231
Kidneys	0.537	0.541	0.537	0.541	0.729
Liver	0.0578	0.0617	0.0582	0.0622	0.0736
Lungs	0.0318	0.0411	0.0321	0.0415	0.03
Pancreas	0.0126	0.0137	0.0221	0.0241	0.017
Red marrow	0.00893	0.00969	0.0185	0.0203	0.0113
Spleen	0.019	0.0242	0.0195	0.0248	0.0262
E (mSv/MBq)	0.0189	0.0204	0.0254	0.0277	0.0252

muscle or rest of body as source organ for the muscle TIAC is more relevant (big differences between TEST 1/2 and TEST 3/4). There are some exceptions, as in the case of kidneys, for which the attribution of the muscle TIAC seems to not have any influence, so the only effect is the small one related to the blood TIAC assignment.

The same tests were performed also for ^{46}Sc-cm10. The results are reported in table 5.5.

Table 5.5: Absorbed doses to various main organs and effective dose obtained with MIRDcalc 1.1 for different configurations, compared to OLINDA 2.1.1 results, for ^{46}Sc-cm10.

Organ or Tissue	MIRDcalc (mGy/MBq)				OLINDA (mGy/MBq)
	TEST 1	TEST 2	TEST 3	TEST 4	
Adrenals	0.802	0.808	0.83	0.839	0.84
Small intestine	0.191	0.192	0.244	0.227	0.199
Stomach	0.236	0.239	0.269	0.277	0.232
Heart wall	0.173	0.179	0.203	0.223	0.19
Kidneys	1.91	1.91	1.92	1.93	2.62
Liver	0.414	0.424	0.423	0.434	0.477
Lungs	0.214	0.231	0.218	0.239	0.187
Pancreas	0.325	0.328	0.373	0.381	0.248
Red marrow	0.179	0.193	0.2	0.215	0.176
Spleen	0.338	0.346	0.349	0.359	0.428
E (mSv/MBq)	0.199	0.203	0.219	0.226	0.193

The first consideration is that ^{46}Sc causes surely higher doses to human body, confirming the need to reduce as much as possible its presence in the production

phase. Going in details, it can be noticed that TEST 1 shows results more similar to OLINDA ones, particularly when comparing the E values. However, when considering ^{46}Sc, fluctuations in the corresponding absorbed doses between all the tests are more limited, resulting in a higher compatibility of the OLINDA software results with all the MIRDcalc software tests. A constant noteworthy behaviour can be observed for kidneys: as in the case of ^{47}Sc-cm10, the absorbed dose for this organ has a quite identical value for every TIACs distribution, and this value is always smaller of about 30% with respect to OLINDA software dose calculation. This difference can be probably attributed to the different organ masses used in MIRDcalc (and IDAC-Dose) and OLINDA. In fact, while in OLINDA software the weight of the blood contained in the organs is not included in the organ masses, in MIRDcalc software it is considered. The resulting constant non-negligible difference in kidneys absorbed doses has a particular importance because this target organ always receives the highest dose. Moreover, this constant difference is obtained also when using IDAC-Dose 2.1 software.

IDAC-Dose has no heart contents as source organ, so only tests on muscle TIAC allocation could be performed. Blood TIAC was always assigned to blood source organs while:

- in TEST 5 muscle TIAC is given to muscle source organ.
- in TEST 6 muscle TIAC is given to "other".

Obtained absorbed doses and effective dose for ^{47}Sc-cm10 are reported in table 5.6, compared to OLINDA results.

TEST 5 is the counterpart of TEST 2 in table 5.4, while TEST 6 is the one of TEST 4 for the TIACs distribution. Results obtained with IDAC-Dose and MIRDcalc for corresponding configurations are always quite similar if not identical. This is true also for the case of ^{46}Sc-cm10, whose results are presented in table 5.7. In this case, TEST 2 of table 5.5 and TEST 5 of table 5.7 show exactly the same values for the absorbed doses to organs. This can be considered an evident consequence of the same phantom format implemented in the two software.

Concerning the comparison with OLINDA software results, IDAC-Dose outcomes are in most cases comparable, but not always similar, in particular when looking at the effective dose. This is surely due to the fact that the OLINDA software phantom model is different, but also the irreproducibility of OLINDA TIACs assignation to source organs in IDAC-Dose contributes.

Table 5.6: Absorbed doses to various main organs and effective dose obtained with IDAC-Dose 2.1 for different configurations, compared to OLINDA 2.1.1 results, for ^{47}Sc-cm10.

Organ or Tissue	IDAC-Dose (mGy/MBq) TEST 5	TEST 6	OLINDA (mGy/MBq)
Adrenals	0.0311	0.0391	0.0362
Small intestine	0.00998	0.0167	0.0191
Stomach	0.0158	0.0223	0.0235
Heart wall	0.0097	0.0182	0.0231
Kidneys	0.538	0.538	0.729
Liver	0.0615	0.0618	0.0736
Lungs	0.0276	0.034	0.03
Pancreas	0.0136	0.0223	0.017
Red marrow	0.00966	0.0189	0.0113
Spleen	0.0242	0.0247	0.0262
E (mSv/MBq)	0.0211	0.0289	0.0252

Table 5.7: Absorbed doses to various main organs and effective dose obtained with IDAC-Dose 2.1 for different configurations, compared to OLINDA 2.1.1 results, for ^{46}Sc-cm10.

Organ or Tissue	IDAC-Dose (mGy/MBq) TEST 5	TEST 6	OLINDA (mGy/MBq)
Adrenals	0.808	0.833	0.84
Small intestine	0.192	0.221	0.199
Stomach	0.239	0.27	0.232
Heart wall	0.179	0.208	0.19
Kidneys	1.91	1.92	2.62
Liver	0.423	0.432	0.477
Lungs	0.204	0.221	0.187
Pancreas	0.328	0.368	0.248
Red marrow	0.193	0.211	0.176
Spleen	0.346	0.357	0.428
E (mSv/MBq)	0.224	0.245	0.193

Since in MIRDcalc and in IDAC-Dose there is the possibility to choose blood and muscle as source organs, effective doses resulting from this configuration both for ^{47}Sc-cm10 and ^{46}Sc-cm10 were then used in section 5.3 to assess the best proton beam energy interval and irradiation time for the production of ^{47}Sc using ^{nat}V targets.

5.3 Dosimetry analysis for irradiation parameters evaluation

Nuclear cross-section results are necessary to give a hint on which can be an ideal energy interval for the production of a radionuclide. In this interval, the production of the radionuclide of interest should be maximized while the yield of eventual co-produced contaminants should be minimized. These contaminants present in the final solution (mainly isotopic contaminants since non-isotopic ones can be chemically separated) cannot be ignored because they can compete in the radiolabelling procedure of the radiopharmaceutical, and so can contribute to the exposure of a patient to radiation. This contribution needs to be quantified to evaluate if, from a clinical point of view, a safe application of the radiopharmaceutical can be guaranteed. To make this possible a limit on the RNP has to be established, usually expressed as a percentage. For a good manufacturing practice (GMP), it is indicatively set higher than 99%, confining the radioisotopic impurities level at maximum 1%, and then properly reduced, if possible, for each radiopharmaceutical. RNP, defined in chapter 4, is calculated, at EoB, as the ratio between the activity of the radionuclide of interest and the sum of all the activities of the involved radionuclides:

$$RNP = \frac{A_x(t)}{\sum_i A_{x,i}(t)} \cdot 100 \tag{5.9}$$

and its evolution with time is obtained exploiting the activity exponential radioactive decay law. In this way, since radionuclides have different half-lives, it is possible to check how long the limit on RNP is fulfilled.

Another important factor to determine the maximum acceptable quantity of impurities is the Dose Increase (DI), which represents the additional contribution to the radiation dose imparted to a patient due to the contaminants' presence. There is not a fixed value for DI that has to be respected. A limit of 10% is considered a good starting point and it is the one adopted in this work. The DI is evaluated as the ratio between the impurities' effective doses, Es, given by the corresponding fractions of injected activity and the total effective dose, ED_t, given by all the produced radionuclides:

$$DI = \frac{\sum_i f_i(t)E_i}{\sum_j f_j(t)E_j} = \frac{\sum_i f_i(t)E_i}{ED_t(t)} \tag{5.10}$$

where the sum in i indicates that only contaminants contributions are con-

sidered, while the sum in j is total so all the produced radionuclides are included, also the one of interest. The f, instead, is the fraction of total activity of the corresponding radioisotope and it varies with time as well as DI, consequently.

Those two limits on RNP and DI calculated in different beam energy intervals and irradiation times, for a fixed beam intensity, can indicate which are the best options for the production of a new medical radionuclide. They complete and refine the information given by the nuclear cross-sections adding the knowledge of the maximum amount of admissible impurities, for a specific radiopharmaceutical, and of the irradiation parameters for which this requirement is respected. Moreover, RNP and DI limits establish the time of validity of the radiopharmaceutical after the EoB, corresponding to the time interval in which both RNP>99% and DI<10% conditions are met.

5.3.1 Dosimetric evaluation of the ^{nat}V(p,x)^{47}Sc production route

The ^{47}Sc production route using protons impinging on ^{nat}V targets was investigated during the PASTA project. Cross-section measurement results were presented in [69, 84] and they were also the topic of my master thesis [83]. From those results a promising energy interval, namely $E_p < 30$ MeV, was individuated where the production of ^{47}Sc occurs with a really low co-production of ^{46}Sc. The activities produced at EoB were estimated to be 41.5 MBq/μA and 111 MBq/μA for 24 h and 80 h irradiation times, respectively, for ^{47}Sc, and 14.9 kBq/μA and 49.2 kBq/μA for ^{46}Sc, correspondingly [70]. Dosimetric evaluations based on PASTA project and literature available cross-section results were performed, using OLINDA 2.1.1 software, in [133]. In that work, RNP and DI in various energy intervals, namely 19÷30 MeV, 19÷35 MeV, 19÷40 MeV, and 19÷45 MeV, for both 24 h and 80 h irradiation time were evaluated, considering a hypothetical beam intensity of 1 μA. From the dosimetric results, it was possible to assess that the most advantageous energy interval, where the production of ^{47}Sc is maximized while containing the impurities quantity within the limits, was 19÷35 MeV. To have an even higher ^{47}Sc production 80 h irradiation time should be chosen, although the time of validity of the radiopharmaceutical, t_{MAX} (time interval after the EoB in which RNP and DI limits are satisfied), is reduced to 30 h.

In this thesis work the same calculations and results analyses were repeated, but using MIRDcalc 1.1 and IDAC-Dose 2.1 software to check if the same conclusions could be reached despite different phantom modelling. In both the software

the TIACs in table 5.3 were used and blood and muscle were chosen as source organs for the corresponding TIACs. Dosimetric simulations were limited to the 19÷30 MeV and 19÷35 MeV energy intervals because above 35 MeV ^{48}Sc starts to be produced but, at the moment, this radionuclide is not included in the list of MIRDcalc selectable radionuclides. RNP is a quantity dependent on the produced activity and not on the radiopharmaceutical biodistribution so it is the same regardless of the software used. Its behaviour as a function of time in the different energy intervals and irradiation times investigated is here reported in figure 5.3, identical to what presented in [133], together with a focus on the RNP>90% area to better evaluate the curves trend in this region.

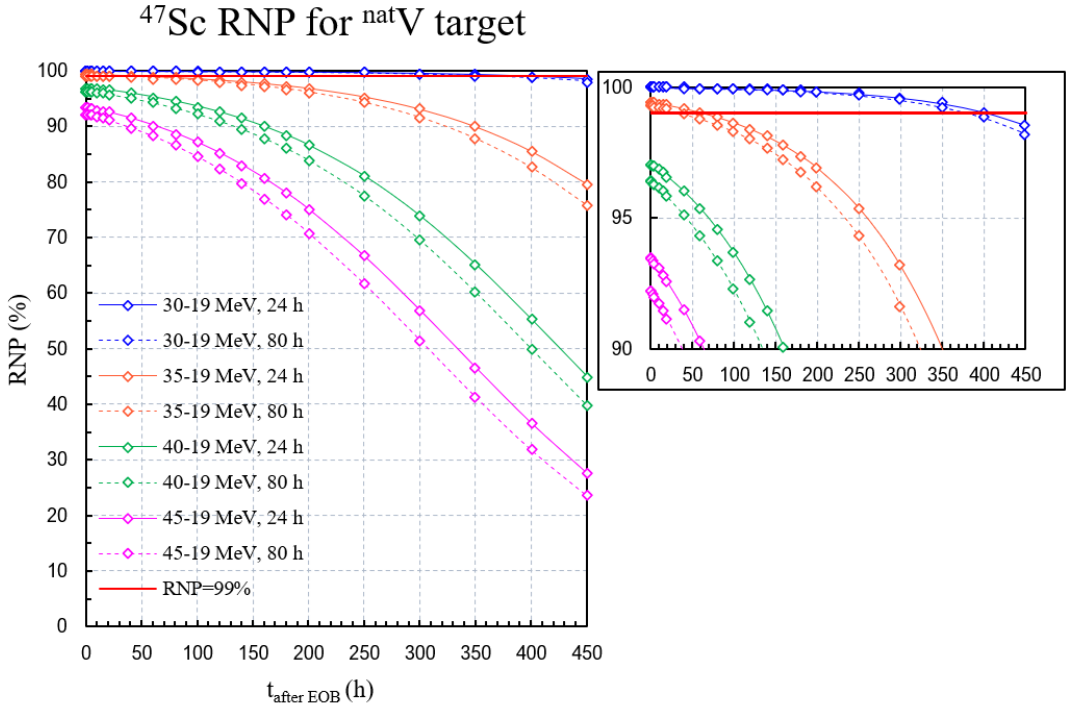

Figure 5.3: ^{47}Sc RNP as a function of time after EoB for different irradiation times and energy intervals investigated for the production via the ^{nat}V(p,x)^{47}Sc nuclear reaction, considering a beam intensity of 1 μA [133]. A 90÷100% interval close-up of the RNP is in the box on the right.

As already underlined in [133], due to the presence of both ^{46}Sc and ^{48}Sc, the RNP is never higher than 99% in the energy intervals 19÷40 MeV and 19÷45 MeV for none of the irradiation times, as also shown in figure 5.3. Those energy intervals have to be excluded for a possible production of ^{47}Sc via the ^{nat}V(p,x) nuclear reaction. For this reason, the limitation of dosimetric simulations to 19÷30 MeV and 19÷35 MeV energy intervals did not constitute a huge problem. In the energy interval 19÷30 MeV the RNP limit above 99% is satisfied for a long time after the EoB, namely 375 h and 400 h for 80 h and 24 h irradiation

time respectively, while this time is reduced to 30 h and 60 h, respectively, in the energy range 19÷35 MeV [133].

However, also the DI has to be evaluated. Absorbed and effective doses obtained for ^{47}Sc and ^{46}Sc with MIRDcalc and IDAC-Dose are reported in table 5.8. Those effective doses are used to calculate DI.

Table 5.8: Absorbed doses to various main organs and effective dose obtained with MIRDcalc 1.1 and IDAC-Dose 2.1 for the DOTA-folate conjugate cm-10 radiolabelled with ^{47}Sc and ^{46}Sc.

Organ or Tissue	MIRDcalc (mGy/MBq)		IDAC-Dose (mGy/MBq)	
	^{47}Sc-cm10	^{46}Sc-cm10	^{47}Sc-cm10	^{46}Sc-cm10
Adrenals	0.0389	1.01	0.0379	1.01
Brain	0.00154	0.0551	0.00133	0.0544
Esophagus	0.00787	0.196	0.00675	0.192
Eyes	0.00119	0.0501	0.00101	0.0497
Gallbladder wall	0.0199	0.497	0.0196	0.496
Colon-left	0.00871	0.217	0.00763	0.214
Colon-right	0.0110	0.276	0.00988	0.274
Colon-rectum	0.00536	0.113	0.00434	0.111
Heart wall	0.00830	0.192	0.00692	0.185
Kidneys	0.731	2.42	0.726	2.42
Liver	0.0797	0.535	0.0782	0.531
Lungs	0.0373	0.243	0.0242	0.215
Pancreas	0.0150	0.399	0.0141	0.396
Prostate	0.00417	0.119	0.00398	0.118
Salivary glands	0.110	0.381	0.110	0.380
Spleen	0.0297	0.434	0.0281	0.431
Small intestine	0.00956	0.222	0.00848	0.220
Stomach	0.0156	0.279	0.0145	0.275
Testes	0.00308	0.0808	0.00281	0.0801
Thymus	0.00382	0.120	0.00354	0.117
Thyroid	0.00449	0.118	0.00380	0.114
Urinary bladder	0.00355	0.109	0.00340	0.108
E (mSv/MBq)	0.0223	0.232	0.0307	0.244

From values in table 5.8 it can be noticed that absorbed doses due to ^{46}Sc-cm10 are always higher than ^{47}Sc ones, about 1 or 2 order of magnitude. The same is true also for the effective doses, as consequence. The target organ receiving the higher dose per unit administered activity is kidneys. Comparing MIRDcalc and IDAC-Dose results, similar values are obtained, identical in some cases (e.g. salivary glands for ^{47}Sc-cm10, adrenals for ^{46}Sc-cm10).

In table 5.9 there are the activities at EoB for ^{47}Sc and ^{46}Sc produced with

proton beams on ^{nat}V targets for different irradiation parameters, considering a beam current of 1μA. Those values are used to determine the fractions at any time after the EoB needed in equation 5.10 to calculate the DI. The results as function of time after EoB are reported in figure 5.4 for MIRDcalc software and in figure 5.5 for IDAC-Dose software.

Table 5.9: Calculated yields at EoB for ^{47}Sc and ^{46}Sc produced with a 1μA proton beam impinging on ^{nat}V targets at different irradiation conditions [133].

$\mathbf{t_{irr}}$ **=24 h**		
Activity	19÷30 MeV	19÷35 MeV
^{47}Sc (MBq)	41.5	105
^{46}Sc (MBq)	$1.49{\cdot}10^{-2}$	$6.45{\cdot}10^{-1}$
$\mathbf{t_{irr}}$ **=80 h**		
Activity	19÷30 MeV	19÷35 MeV
^{47}Sc (MBq)	111	279
^{46}Sc (MBq)	$4.92{\cdot}10^{-2}$	2.13

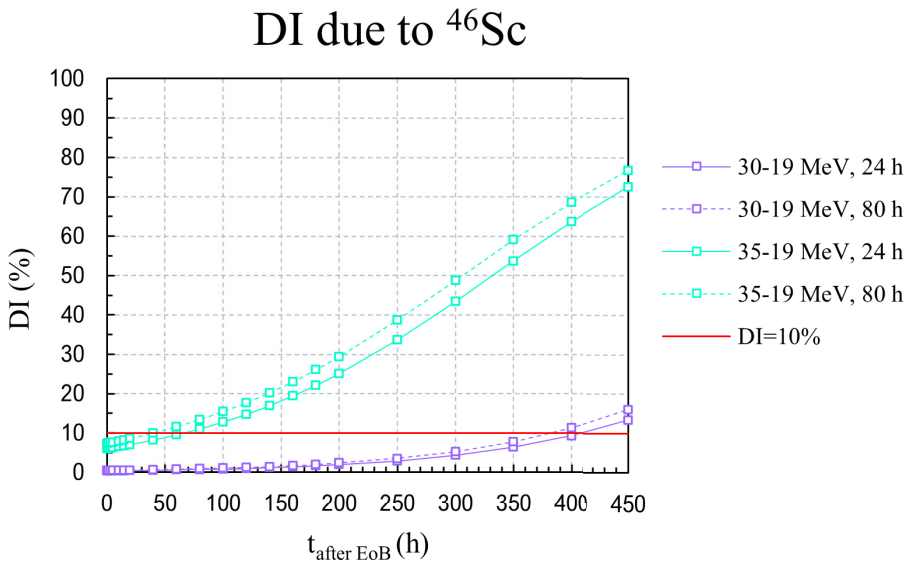

Figure 5.4: DI due to the presence of ^{46}Sc evaluated with MIRDcalc 1.1 software as a function of time after EoB for different irradiation times and energy intervals investigated for the production via the ^{nat}V(p,x)^{47}Sc nuclear reaction, considering a beam intensity of 1 μA.

From figures 5.5 and 5.4 it is evident that both the energy intervals 19÷30 MeV and 19÷35 MeV allow a ^{47}Sc production pure enough for medical application whatever the irradiation time is 24 h or 80 h, since the DI assumes values lower than 10% for some time intervals after EoB. This is true for both the software. In fact, the DI trends are really similar, an expected consequence of the similar

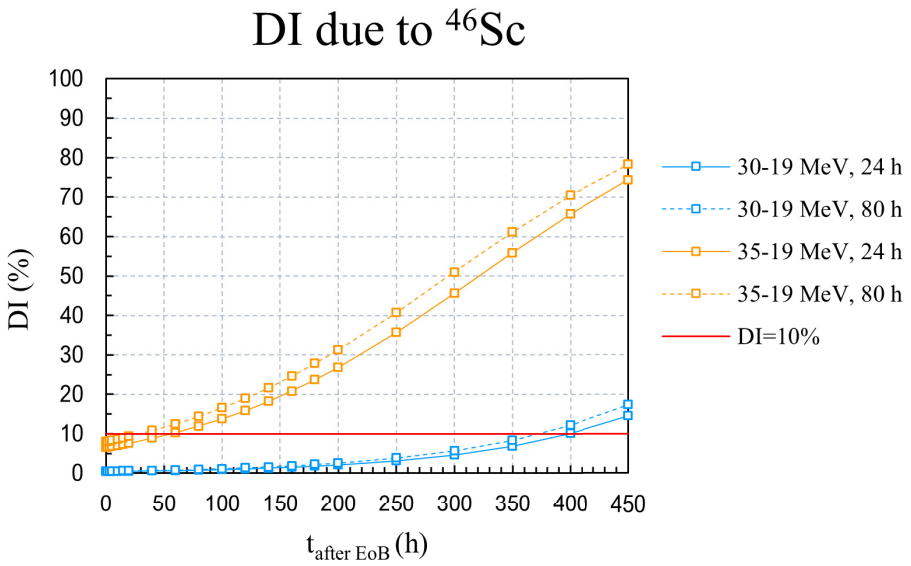

Figure 5.5: DI due to the presence of ^{46}Sc evaluated with IDAC-Dose 2.1 software as a function of time after EoB for different irradiation times and energy intervals investigated for the production via the ^{nat}V(p,x)^{47}Sc nuclear reaction, considering a beam intensity of 1 μA.

absorbed doses. However, the trends are not perfectly overlapping. The time intervals after EoB where the condition DI<10% is satisfied differs of about 10 h between MIRDcalc and IDAC-Dose evaluations. In particular, for every scenario investigated, the time interval derived from MIRDcalc results is 10 h longer than the corresponding one deduced from IDAC-Dose simulation results.

The time intervals obtained imposing the 10% limit on DI have to be compared, then, to the time intervals obtained from the requirement RNP>99%. All these resulting time intervals are summarised in table 5.10.

Time intervals obtained imposing RNP>99% are equal to the ones obtained imposing DI<10% when DI is calculated starting from the IDAC-Dose simulation results. The only exception is encountered for the irradiation parameters: beam energy range 19÷35 MeV and 24 h irradiation time. In this case, time interval after EoB is reduced to 55 h by IDAC-Dose results. Concerning the MIRDcalc results, the most stringent condition is always the RNP limit whatever irradiation parameters are considered.

The RNP as the factor delimiting the time interval after EoB in which the radiopharmaceutical can be used safely is the same outcome obtained performing simulations with OLINDA 2.1.1 software [133]. All the three software (IDAC-Dose, MIRDcalc, and OLINDA) agree that, to maximize the ^{47}Sc production the energy interval 19÷35 MeV and the irradiation time 80 h should be chosen

Table 5.10: Time interval after EoB in which the limits on RNP or DI are fulfilled. Results for the ^{nat}V(p,x)^{47}Sc production route with different irradiation parameters are considered, supposing a beam intensity of 1 μA and the use of both IDAC-Dose and MIRDcalc dosimetric software.

MIRDcalc derived time interval where DI<10%		
Energy interval	t_{irr} =24 h	t_{irr} =80 h
19÷30 MeV	410 h	385 h
19÷35 MeV	65 h	40 h
IDAC-Dose derived time interval where DI<10%		
Energy interval	t_{irr} =24 h	t_{irr} =80 h
19÷30 MeV	400 h	375 h
19÷35 MeV	55 h	30 h
Time interval where RNP>99%		
Energy interval	t_{irr} =24 h	t_{irr} =80 h
19÷30 MeV	400 h	375 h
19÷35 MeV	60 h	30 h

even if the time interval after EoB to inject the radiopharmaceutical is limited to 30 h. With these irradiation conditions the maximum ^{47}Sc activity that can be produced at EoB, considering a 100 μA beam current, is 27.9 GBq.

Even if an accordance has been found in the final evaluation of the irradiation parameters compared to [133], it has to be remembered that they are mainly determined from RNP values and not from dosimetric simulations. In fact, from the observation of the absorbed doses obtained some differences have been highlighted, especially linked to the different phantoms' modelling. However, the uncertainties are acceptable if compared to the uncertainties introduced by the animal to human scaling. To make the dosimetric analysis more precise, human biodistribution data are advisable and the analysis should be extended to different radiopharmaceuticals, as the dosimetric contribution of the impurities is dependent on the biodistribution and kinetics characteristics of the considered radiopharmaceutical [137].

5.3.2 Evaluation of the ^{47}Sc production using enriched Ti targets

In the REMIX project ^{47}Sc production using proton beams on enriched ^{48,49,50}Ti targets was investigated. In section 4.2 the lack of an energy interval where the production of ^{47}Sc using enriched ^{49}Ti targets is maximized while the one of contaminants is minimized has been already highlighted. Too many contaminants with a high cross-section are co-produced in the whole energy range investigated.

In section 4.3, instead, the production with enriched ^{50}Ti has been discussed. In the low energy region this production route seems to be promising, however dosimetric evaluations are postponed to when the correction of ^{44m,g}Sc cross-section results for the presence of isotopic contaminants in the target is completed.

^{48}Ti(p,x)^{47}Sc TTY at EoB for different energy intervals and different irradiation times assuming a beam current of 1 μA were presented in table 4.3 in section 4.1. From these values the RNP evolution with time was evaluated for the various scenarios. RNP trends are reported in figure 5.6.

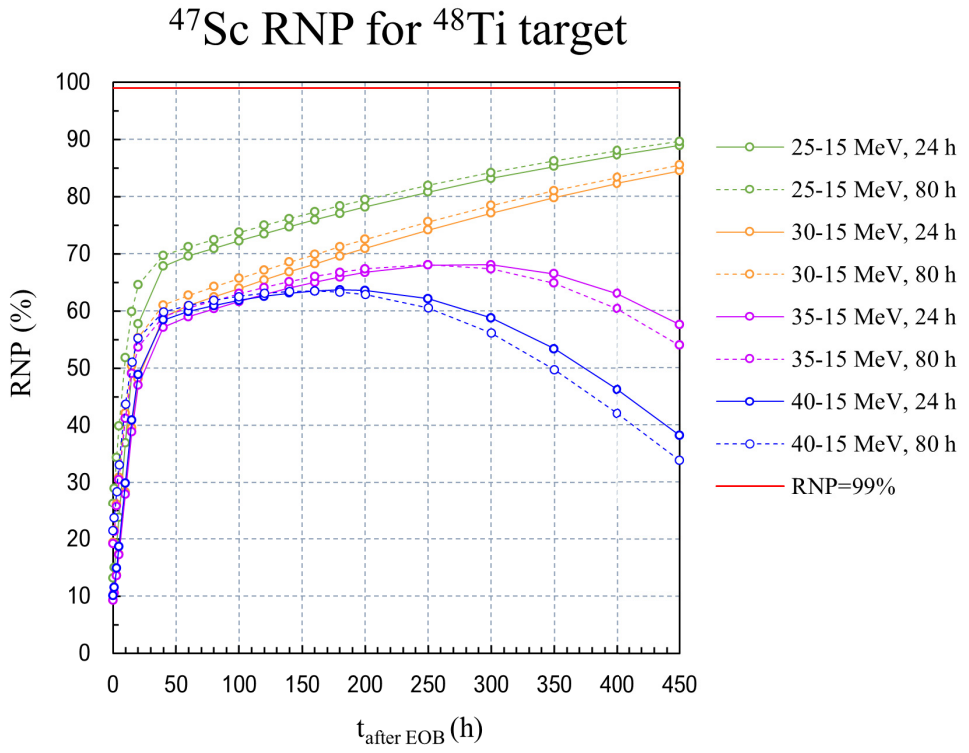

Figure 5.6: ^{47}Sc RNP as a function of time after EoB for different irradiation times and energy intervals investigated for the production via the ^{48}Ti(p,x)^{47}Sc nuclear reaction, considering a beam intensity of 1 μA.

The rapid increase soon after the EoB in all the RNP trends is due to the short half-life of ^{44g}Sc ($T_{1/2}$= 4.0420 h) and ^{43}Sc ($T_{1/2}$= 3.891 h) which can be considered decayed in about 40 h after EoB. However, ^{44m}Sc is still present as well as ^{46}Sc in the two wider energy intervals investigated. It is due to ^{46}Sc presence that the RNP decreases above 250 h after EoB: this time equals about 3 ^{47}Sc half-lives ($T_{1/2}$= 80.3808 h) and so the amount of ^{47}Sc is significantly reduced while the one of ^{46}Sc is not ($T_{1/2}$= 2010.96 h).

A RNP higher than 99% is never reached: it is always below 90%, and ap-

proaches this value only for irradiation parameters corresponding to 80 h irradiation time and 25÷15 MeV beam energy interval, but only after 450 h from the EoB. At this time, the amount of ^{47}Sc is already reduced of more than $1/32^{nd}$ (more than 5 half-lives) of its originally produced quantity. ^{48}Ti(p,x)^{47}Sc is thus not a favourable production route just considering the reached RNP. For this reason, dosimetric evaluations through software were considered unnecessary.

^{nat}V and enriched ^{50}Ti targets are the most valuable options for the production of enough pure ^{47}Sc for medical applications, when considering proton beams. While irradiation parameters for ^{nat}V targets have been already assessed, some further investigations for the evaluation of the best ^{50}Ti irradiation conditions are planned in next future. This will allow to estimate the dosimetric impact of the ^{nat}V$-^{50}$Ti multilayer target configuration proposed in the deposited patent.

Conclusions

In this thesis work, various proton-induced nuclear reactions were investigated for the production of the theranostic radionuclide ^{47}Sc. Its β^- and γ emissions can be used for internal targeted radiation therapy and for imaging with SPECT cameras, respectively. Moreover, ^{47}Sc can be paired to the β^+ emitters ^{44g}Sc or ^{43}Sc to perform PET imaging exploiting the same radiopharmaceutical. The main advantage is the possibility to evaluate the patient's response prior to therapy and so, to personalize the therapeutic treatment according to patient specificities and needs. In view of a possible future production at the INFN-LNL, where the SPES 70 MeV proton cyclotron has been installed, the LARAMED project aims at the identification of the most convenient ^{47}Sc production route, corresponding to the maximization of ^{47}Sc produced quantity while minimizing the co-produced contaminants presence, since they are responsible of an extra potentially harmful dose administration to patients.

The knowledge of nuclear reaction cross-sections is the first fundamental step to assess the existence of desirable beam energy intervals in which the medical radionuclide of interest is produced with a low probability to co-produce its contaminants. With the PASTA and REMIX projects the production routes using ^{nat}V, and enriched ^{48}Ti, ^{49}Ti, and ^{50}Ti targets are investigated. In this thesis the cross-section results concerning all the three possible enrichments for Ti targets are presented and discussed. Thin targets, consisting of thin layers ($1 \div 2$ μm) of enriched Ti powder deposited on Al substrates exploiting the HIVIPP technique, were manufactured and characterized at the INFN-LNL in the context of the E_PLATE and REMIX projects. Meanwhile the SPES infrastructure at the INFN-LNL is completed, the samples were irradiated and then the produced activity measured with γ spectroscopy at the ARRONAX facility, in Nantes (France). Some experiments with enriched ^{50}Ti targets were also conducted in Switzerland at the Bern University hospital facility to investigate the low energy range ($E_p < 18.3$ MeV) where an almost isotopically pure ^{47}Sc production can be

obtained, with a low contamination of ^{46}Sc, detected only at the highest proton energy investigated, 18.2 MeV. In addition, one ^{48}Ti target was irradiated with protons of 18.2 MeV to correct the ^{50}Ti(p,α)^{47}Sc cross-section for the contribution due to the presence of ^{48}Ti contamination in the enriched ^{50}Ti powder. Correction for isotopic contaminations in the purchased powders were also performed in the whole energy range investigated for the presence of ^{48}Ti in the ^{49}Ti enriched powder, and for the presence of both ^{48}Ti and ^{49}Ti in the ^{50}Ti powder.

Overall, cross-section values were obtained for 15 different beam energies concerning the use of enriched ^{48}Ti depositions, for 14 beam energy values for the enriched ^{49}Ti depositions, and for 21 values of the beam energy related to the enriched ^{50}Ti depositions. The cross-section values obtained were compared to previous literature data, when available, and to theoretical estimations obtained with TALYS 1.96 software using default parameters for density levels and optical models. No particular discrepancies were observed except for some cases in which theoretical curves overestimate or underestimate the experimental results. For this reason, a collaboration with theoretical nuclear modelling experts is ongoing to better reproduce the experimental points. The experts of nuclear models are also involved in the resolution of a problem regarding the ^{50}Ti(p,x)^{44m,g}Sc cross-sections: after corrections for isotopic contaminations in the target powder, some not null cross-section values were obtained at energies below the reaction threshold. It was found that those anomalies were due to the presence of also ^{46}Ti and ^{47}Ti in the targets. Even if in low percentage (less than 2%), their cross-sections for the ^{44m,g}Sc production are so high that they cannot be neglected, especially the contribution of ^{46}Ti. Since no literature experimental data are available to perform the needed correction, a strategy to correct those cross-sections is under investigation with the cooperation of theoretical nuclear physicists.

Until the cross-section results obtained for ^{50}Ti targets will not be completed, dosimetric evaluations of this production route will not be performed. In fact, dosimetry analysis is the step following the cross-section calculations, that allows to individuate the best irradiation parameters for a particular production route. The parameters can be assessed for a particular production route and a specific radiopharmaceutical. Biodistribution studies on mice available in literature for the ^{47}Sc-cm10 radiopharmaceutical were used in this thesis to evaluate the absorbed doses administered to the human organs and the total effective dose due to ^{47}Sc and the ones due to isotopic contaminants. Non-isotopic contaminants, like ^{43}K and ^{48}V, can be chemically separated so they are not a concern. Two

different software were utilised to perform dosimetric simulations. Results were used to calculate the DI (dose increase) due to present contaminants. This value, in combination with RNP (radionuclidic purity) evaluated from TTY (thick target yield) calculations, indicates which irradiation parameters (energy interval, irradiation time) can be exploited for a maximized production of the ^{47}Sc maintaining the amount of contaminants within certain safe limits. In this thesis work, those limits were indicatively imposed as RNP>99% and DI<10%. Those considerations allowed also to establish the time interval after EoB in which the radiopharmaceutical fulfils the limits and so can be safely injected in a patient.

Dosimetric simulations for the production through enriched ^{48}Ti targets were not needed because RNP never reaches a value higher than even 90%, within 450 h after the EoB, meaning that this production route is not able to provide enough pure ^{47}Sc.

Concerning enriched ^{49}Ti targets, the situation is similar: from cross-section results it was evident that an energy interval with at least a low contaminants co-production was not identifiable. However, those results are innovative since they constitute the first measurement of this nuclear reaction.

In this thesis, dosimetric analysis concerning the ^{nat}V(p,x)^{47}Sc production route were also presented, based on cross-section experimental data previously measured in the context of the PASTA project and already available in literature. From cross-sections evaluation an energy interval ($E_p < 30$ MeV) where the production of ^{47}Sc occurs with a really low co-production of ^{46}Sc was individuated. With dosimetric evaluations this interval was extended up to $E_p < 35$ MeV. In this energy interval, an irradiation time of 80 h can lead to a ^{47}Sc production pure enough for medical applications in the first 30 h after the EoB.

The promising results obtained from dosimetric evaluations of the production route with ^{nat}V and from cross-section analysis for the enriched ^{50}Ti targets were combined in the conception of a multilayer target, described in a recently submitted INFN patent (request number 102023000018477, date of submission September 8^{th}, 2023), where the ^{nat}V layer covers the energy range from 35 MeV to 22 MeV while an enriched ^{50}Ti layer is used to exploit the more advantageous production from 22 MeV to 9 MeV.

The results described and discussed in this thesis reveal the synergy between nuclear physics needed for cross-section measurements and medical physics knowledge necessary for dosimetric evaluations. This can be noted also from a wider point of view: the collaboration between multiple and various scientific disciplines

in the medical radionuclides production research field is a crucial and uncommon aspect. Regarding this topic, a future perspective of the interdisciplinary LARAMED group is that of completing the production cycle investigating also the post-irradiation processing of the target and material recovery, especially of the enriched one that is more expensive.

Next steps in the nearest future for the work here presented are the completion of cross-section data analysis for ^{50}Ti targets followed by dosimetric evaluations for the DOTA-folate conjugate cm-10 to individuate the best irradiation parameters also for this production route. Results will be presented in dedicated publications. Future perspectives include also some small-scale production tests using thick targets, according to the outcomes of this thesis. The aim is to perform some *in-vitro* and *in-vivo* preclinical studies both at the INFN-LNL and in collaboration with other research institutions, thanks to the wide national and international network of the LARAMED team. The purpose of the INFN-LNL is to become a relevant centre for the research and production of innovative and emerging radionuclides requiring a high energy proton beam to contribute to the development and supply of innovative radiopharmaceuticals.

List of Figures

List of Tables

References

[1] Lars R Holsti, *Development of clinicial radiotherapy since 1896*, (1995) *Acta Oncologica*, 34, 8, 995-1003.

[2] Carolyn J Anderson *et al.*, *A Short History of Nuclear Medicine.* In: *Radiopharmaceutical Chemistry*, (2019) Springer, Cham, Switzerland, https://doi.org/10.1007/978-3-319-98947-1_2

[3] Brian J Burkett *et al.*, *A Review of Theranostics: Perspectives on Emerging Approaches and Clinical Advancements*, (2023) *Radiology: Imaging Cancer*, 5 (4), e220157, https://doi.org/10.1148/rycan.220157

[4] IAEA Coordinated Research Project (CRP), *Therapeutic Radiopharmaceuticals Labelled with New Emerging Radionuclides (^{67}Cu, ^{186}Re, ^{47}Sc)*, (2016-2020) *CRP No. F22053.*

[5] Gaia Pupillo *et al.*, *Cyclotron-based production of innovative medical radionuclides at the INFN-LNL: state of the art and perspective*, (2023) *The European Physical Journal Plus*, 138, 1095, https://doi.org/10.1140/epjp/s13360-023-04564-3

[6] Gaia Pupillo *et al.*, *The LARAMED project at INFN-LNL: review of the research activities on medical radionuclides production with the SPES cyclotron*, (2023) *Journal of Radioanalytical and Nuclear Chemistry*, 2295(1), 020001, https://doi.org/10.1063/5.0032898

[7] National Nuclear Data Center at Brookhaven National Laboratory, *NuDat 3.0*, https://www.nndc.bnl.gov/nudat3/, (actively maintained and updated), last consultation: September 2023.

[8] Timothy Cain, *Nuclear Medicine. In: Inside Radiology*, https://www.insideradiology.com.au/nuclear-medicine/#:~:text=The%

20actual%20amount%20of%20the,between%20different%20types%20of%20studies. (Updated July 2017), last consultation: February 2024.

[9] IAEA Bulletin 55, *Radiation and radionuclides in medicine*, (2014) *IAEA Bulletin 55-4*.

[10] World Nuclear Association, *Radioisotopes in Medicine*, https://world-nuclear.org/information-library/non-power-nuclear-applications/radioisotopes-research/radioisotopes-in-medicine.aspx (Updated February 2023), last consultation: April 2023.

[11] OECD/NEA, *The Supply of Medical Isotopes: An Economic Diagnosis and Possible Solutions*, (2019) OECD Publishing, Paris, https://doi.org/10.1787/9b326195-en

[12] Guillermina Ferro-Flores, Consuelo Artega de Murphy and Laura Meléndez-Alafort, *Third Generation Radiopharmaceuticals for Imaging and Targeted Therapy*, (2006) *Current Pharmaceutical Analysis*, 2, 339-352 https://doi.org/10.2174/157341206778699555

[13] Gopal B Saha, *Fundamentals of Nuclear Pharmacy* 5th edition (2004) Sringer-Verlag, New York, USA.

[14] Rafael T M de Rosales, *Potential clinical applications of bimodal PET-MRI or SPECT-MRI agents*, (2014) *Journal of Labelled Compounds and Radiopharmaceuticals*, 57, 4, 298-303, https://doi.org/10.1002/jlcr.3154

[15] Maurizio Conti and Lars Eriksson, *Physics of pure and non-pure positron emitters for PET: a review and a discussion*, (2016) *EJNMMI Physics*, 3, 8, https://doi.org/10.1186/s40658-016-0144-5

[16] Elisa M Crestoni, *Radiopharmaceuticals for Diagnosis and Therapy*, (2018) *Elsvier*, Reference Module in Chemistry, Molecular Sciences and Chemical Engineering, https://doi.org/10.1016/B978-0-12-409547-2.14205-2

[17] Stuart C White, *Oral radiology*, 7th edition (2014) Mosby Elsevier, Missouri, 229-249, https://doi.org/10.1016/B978-0-323-09633-1.00014-6

[18] Committee on the mathematics and physics of emerging dynamic biomedical imaging, *Mathematics and Physics of Emerging Biomedical Imaging*, (1996) National Academy Press, Washington D.C., https://www.ncbi.nlm.nih.gov/books/NBK232492/

[19] Mediso Ltd. commercial website, *Clinical products*, https://mediso.com/global/en/product/group/clinical-products, last consultation: February 2024.

[20] Simon R Cherry, James A Sorenson and Michael E Phelps, *Physics in Nuclear Medicine*, 4th edition (2012) W.B. Saunders, Philadelphia, 209-231, https://www.sciencedirect.com/science/article/pii/B9781416051985000149

[21] Michael Ljungberg and Hendrik P Pretorius, *SPECT/CT: an update on technological developments and clinical applications*, (2018) *The British Journal of Radiology*, 91 (1081), 20160402, https://doi.org/10.1259/bjr.20160402

[22] Douglas J Wagenaar *et al.*, *Advantages of semiconductor CZT for medical imaging*, (2007) *Proceedings of SPIE*, 6707, Penetrating Radiation Systems and Applications VIII, 67070I, https://doi.org/10.1117/12.740329

[23] Ruth E Schmitz, Adam M Alessio and Paul E Kinaham, *The Physics of PET/CT scanners*, https://depts.washington.edu/imreslab/education/Physics%20of%20PET.pdf, last consultation: August 2023.

[24] Siemens Healthineers AG commercial website, *Molecular imaging*, https://www.siemens-healthineers.com/molecular-imaging, last consultation: February 2024.

[25] Wei Jiang, Yamn Chalich and M Jamal Deen, *Sensor for Positron Emission Tomography Applications*, (2019) *Sensors (Basel)*, 19 (22), 5019, https://doi.org/10.3390/s19225019

[26] Sofia Pascu and Jon Dilworth, *Recent developments in PET and SPECT imaging*, (2014) *Journal of Labelled Compounds and Radiopharmaceuticals*, 57, 191-194, https://doi.org/10.1002/jlcr.3196

[27] Farhad Daghighian, Ronald Sumida and Michael E Phelps, *PET Imaging: An Overview and Instrumentation*, (1990) *Journal of Nuclear*

Medicine Technology, 18 (1), 5-15, https://tech.snmjournals.org/content/jnmt/18/1/5.full.pdf

[28] Martine E Lomax, Lisa K Folkes and Peter O'Neill, *Biological Consequences of Radiation-induced DNA Damage: Relevance to Radiotherapy*, (2013) *Clinical Oncology*, 25 (10), 578-585, https://doi.org/10.1016/j.clon.2013.06.007

[29] Joy N Kavanagh, Kelly M Redmond, Giuseppe Schettino and Kevin M Prise, *DSB Repair - A radiation perspective*, (2013) *Antioxidants & redox signaling*, 18 (18), 2458-2472, http://doi.org/10.1089/ars.2012.5151

[30] INTERNATIONAL ATOMIC ENERGY AGENCY, *Radiation Biology: A Handbook for Teachers and Students*, (2010) Training Course Series 42, IAEA, Vienna, https://www.iaea.org/publications/8219/radiation-biology-a-handbook-for-teachers-and-students

[31] George Sgouros, Lisa Bodei, Michael R McDevitt and Jessie R Nedrow, *Radiopharmaceutical Therapy in cancer: clinical advances and challenges*, (2020) *Nature Reviews Drug Discovery*, 19, 589-608 https://doi.org/10.1038/s41573-020-0073-9

[32] Roger M Pallares and Rebecca J Abergel, *Development of radiopharmaceuticals for targeted alpha therapy: Where do we stand?*, (2022) *Frontiers in Medicine (Lausanne)*, 9, 1020188 https://doi.org/10.3389/fmed.2022.1020188

[33] Roger M Pallares and Rebecca J Abergel, *Nanoparticles for targeted cancer radiotherapy*, (2020) *Nano Research*, 13, 2887-2897, https://doi.org/10.1007/s12274-020-2957-8

[34] Agnieszka Majkowska-Pilip *et al.*, *Nanoparticles in Targeted Alpha Therapy*, (2020) *Nanomaterials*, 10 (7), 1366, https://doi.org/10.3390/nano10071366

[35] Khairi M-S Abdullah, *Fundamentals in Nuclear Physics*, (2014) University of Duhok, Kurdistan Region-Iraq, https://www.researchgate.net/publication/315381123_FUNDAMENTALS_IN_NUCLEAR_PHYSICS

[36] S Hertz, A Roberts and R D Evans, *Radioactive iodine as an indicator in the study of thyroid physiology*, (1938) *Proceedings of the Society fer*

Experimental Biology and Medicine, 38 (4), 510-513 https://doi.org/10.3181/00379727-38-9915P

[37] Earle M Chapman and Robley D Evans, *The treatment of hyperthyroidism with radioactive iodine*, (1946) *Journal of the American Medical Association*, 131 (2), 86-91 https://doi.org/10.1001/jama.1946.02870190010003

[38] Siccandar Jeelani *et al.*, *Theranostics: A treasured tailor for tomorrow*, (2014) *Journal of Pharmacy and Biollied Sciences*, 6 (1), S6-8 https://doi.org/10.4103/0975-7406.137249

[39] Lisa Bodei *et al.*, *Radiotheranostics in oncology: current challenges and emerging opportunities*, (2022) *Nature Reviews Clinical Oncology*, 19, 534-550 https://doi.org/10.1038/s41571-022-00652-y

[40] Gaia Pupillo *et al.*, *Nuclear data for light charged particle induced production of emerging medical radionuclides*, (2022) *Radiochimica Acta*, 110(6-9), 689-706 https://doi.org/10.1515/ract-2022-0011

[41] Renata Mikolajczak *et al.*, *Production of scandium radionuclides for theranostic applications: towards standardization of quality requirements*, (2021) *EJNMMI Radiopharmacy and Chemistry*, 6 (19), https://doi.org/10.1186/s41181-021-00131-2

[42] Suresh C Srivastava, *A Bridge not too Far: Personalized Medicine with the use of Theragnostic Radiopharmaceuticals*, (2013) *Journal of Postgraduate Medicine, Education and Research*, 47 (1), 31-46 https://doi.org/10.5005/jp-journals-10028-1054

[43] Amir R Jalilian *et al.*, *IAEA Activities on* ^{67}Cu, ^{186}Re, ^{47}Sc *Theranostic Radionuclides and Radiopharmaceuticals*, (2021) *Current Radiopharmaceuticals*, 14 (4), 306-314 https://doi.org/10.2174/1874471013999200928162322

[44] Syed M Qaim, *Medical Radionuclide Production: Science and Technology* (2020) De Gruyter, Berlin, Boston, https://doi.org/10.1515/9783110604375

[45] Irène Curie and Frederic Joliot, *Un nouveau type de radioactivité*, (1934) *Comptes rendus de l'Academie des sciences*, 198, 254-256.

[46] Valery Nesvizhevsky and Jacques Villain, *The discovery of the neutron and its consequences (1930–1940)*, (2017) *Comptes Rendus Physique*, 18, 592-600,https://doi.org/10.1016/j.crhy.2017.11.001

[47] Enrico Fermi, *Radioactivity Induced by Neutron Bombardment*, (1934) *Nature*, 133, 757,https://doi.org/10.1038/133757a0

[48] Otto Hahn and Fritz Straßmann, *Radium isotopes from uranium by irradiation with rapid and slow neutrons*, (1938) *Naturwissenschaften*, 26, 756.

[49] Ernest O Lawrence, *Method and apparatus for the acceleration of ions*, (1932) *Google patents*, US1948384A, https://patents.google.com/patent/US1948384

[50] World Nuclear Association, *Research Reactors*, https://world-nuclear.org/information-library/non-power-nuclear-applications/radioisotopes-research/research-reactors.aspx#:~:text=About%20820%20research%20and%20test,in%20the%201960s%20and%201970s. (Updated June 2021), last consultation: September 2023.

[51] Geoffrey M Currie, Janelle M Wheat, R Davidson and Hosen Kiat, *Radionuclide Production*, (2011) *The Radiographer*, 58 (3), 46-52, https://onlinelibrary.wiley.com/doi/pdf/10.1002/j.2051-3909.2011.tb00155.x

[52] JWB, *Thermal fission yield mass for neutron fission (neutron energy 1,5 MeV) of U-235, U-238, and Pu-239*, (2008) *en.wikipedia*, https://commons.wikimedia.org/wiki/File:ThermalFissionYield.svg#file

[53] International Atomic Energy Agency, *Production of Long Lived Parent Radionuclides for Generators:* ^{68}Ge, ^{82}Sr, ^{90}Sr *and* ^{188}W, (2010) *IAEA Radioisotopes and Radiopharmaceuticals Series*, No. 2, IAEA, Vienna, AUstria https://www-pub.iaea.org/MTCD/Publications/PDF/Pub1436_web.pdf

[54] Aleksandra Peeva, *Cyclotrons - What are They and Where Can you Find Them*, https://www.iaea.org/newscenter/news/cyclotrons-what-are-they-and-where-can-you-find-them#:~:text=There%20are%20over%201500%20cyclotron,cyclotron%20facilities%20from%2095%20countries. (Updated June 2021), last consultation: September 2023.

[55] International Atomic Energy Agency, *Accelerator Knowledge Portal*, https://nucleus.iaea.org/sites/accelerators/Pages/Cyclotron.aspx#InplviewHashd5afe566-18ad-4ac0-8aeb-ccf833dbc282=Paged%3DTRUE-p_Proton_x0020_Energy_x0020__x0028%3D30-p_ID%3D310-SortField%3DProton%255fx0020%255fEnergy%255fx0020%255f%255fx0028-SortDir%3DDesc-PageFirstRow%3D61 (under revision), last consultation: September 2023.

[56] Nuclear Physics European Collaboration Committee (NuPECC), *Nuclear Physics for Medicine*, (2014) *European Science Foundation*, report, http://archives.esf.org/fileadmin/Public_documents/Publications/Nuclear_Physics_in_Medicine.pdf

[57] Roman N Sagaidak, *Effects of beam wobbling and target rotation on the target temperature in experiments with intense heavy ion beams*, (2021) *Physical Review Accelerators and Beams*, 24 (8), 083001 https://doi.org/10.1103/PhysRevAccelBeams.24.083001

[58] A Pramudita, *Linacs for medical isotope production*, (2011) *Atom Indonesia*, 37 (1), 1-4 https://doi.org/10.17146/aij.2011.68

[59] Yulun Li *et al.*, *Beam dynamics optimization design of Rhodotron electron accelerator based on genetic algorithm and sensitivity analysis*, (2023) *Applied Radiation and Isotopes*, 201, 111024 https://doi.org/10.1016/j.apradiso.2023.111024

[60] David A Rotsch *et al.*, *Production of medical isotopes with electron linacs*, (2017) *Proceeding of NAPAC*, THB2IO02,1091-1095 https://doi.org/10.18429/JACoW-NAPAC2016-THB2IO02

[61] Mateusz A Synowiecki, Lars R Perk and L Frank W Nijsen, *Production of novel diagnostic radionuclides in small medical cyclotrons*, (2018) *EJNMMI Radiopharmacy and Chemistry*, 3 (3) https://doi.org/10.1186/s41181-018-0038-z

[62] Timothy R DeGrado, Mukesh K Pandey and John Byrne, *Solution target for cyclotron production of radiometals*, (2017) *Google patents*, US20170301427A1, https://patents.google.com/patent/US20170301427A1/en#patentCitations

[63] International Atomic Energy Agency, *Manual for Reactor Produced Radionuclides*, (2013) *IAEA-TECHDOC-1340*, Vienna, Austria.

[64] Sandrine Huclier-Markai *et al.*, *Promising Scandium Radionuclides for Nuclear Medicine: A Review on the Production and Chemistry up to In Vivo Proofs of Concept*, (2018) *Cancer Biotherapy and Radiopharmaceuticals*, 8 (22), https://doi.org/10.1089/cbr.2018.2485

[65] Katherina A Domnanich *et al.*, ^{47}Sc *as useful* β^-*-emitter for the radiotheranostic paradigm: a comparative study of feasible production routes*, (2017) *EJNMMI Radiopharmacy and Chemistry*, 2, 5, https://doi.org/10.1186/s41181-017-0024-x

[66] Gaia Dellepiane *et al.*, ^{47}Sc *and* ^{46}Sc *cross-section measurement for an optimized* ^{47}Sc *production with an 18 MeV medical PET cyclotron*, (2022) *Applied Radiation and Isotopes*, 189, 110428, https://doi.org/10.1016/j.apradiso.2022.110428

[67] Tommaso S Carzaniga and Saverio Braccini, *Cross-section measurement of* ^{44m}Sc, ^{47}Sc, ^{48}Sc *and* ^{47}Ca *for an optimized* ^{47}Sc *production with an 18 MeV medical PET cyclotron*, (2019) *Applied Radiation and Isotopes*, 143, 18-23, https://doi.org/10.1016/j.apradiso.2018.10.015

[68] Ryszard Misiak *et al.*, ^{47}Sc *production development by cyclotron irradiation of* ^{48}Ca, (2017) *Journal of Radioanalytical and Nuclear Chemistry*, 313, 429-434, https://doi.org/10.1007/s10967-017-5321-z

[69] Gaia Pupillo *et al.*, *Production of* ^{47}Sc *with natural vanadium targets: results of the PASTA project*, (2019) *Journal of Radioanalytical and Nuclear Chemistry*, 322, 1711-1718, https://doi.org/10.1007/s10967-019-06844-8

[70] Gaia Pupillo *et al.*, *Correction to: Production of* ^{47}Sc *with natural vanadium targets: results of the PASTA project*, (2021) *Journal of Radioanalytical and Nuclear Chemistry*, 328, 1407, https://doi.org/10.1007/s10967-021-07791-z

[71] C Shaun Loveless *et al.*, *Photonuclear production, chemistry, and in vitro evaluation of the theranostic radionuclide* ^{47}Sc, (2019) *JEJNMMI Research*, 9, 42, https://doi.org/10.1186/s13550-019-0515-8

[72] David A Rotsch *et al.*, *Electron linear accelerator production and purification of scandium-47 from titanium dioxide targets*, (2018) *Applied Radiation and Isotopes*, 131, 77-82, https://doi.org/10.1016/j.apradiso.2017.11.007

[73] Valeriia Starovoitova, Philipp Cole and Terry L Grimm, *Accelerator-based photoproduction of promising beta-emitters ^{67}Cu and ^{47}Sc*, (2015) *Journal of Radioanalytical and Nuclear Chemistry*, 305(1), 127-132, https://doi.org/10.1007/s10967-015-4039-z

[74] Gaia Pupillo *et al.*, *Research Activities on the Cyclotron-Based Production of Innovative Radionuclides: The Experience at the Legnaro National Laboratories of INFN*, (2022) *International Conference on Accelerators for Research and Sustainable Development: From Good Practices Towards Socioeconomic Impact*, IAEA-CN-301/073, https://conferences.iaea.org/event/264/contributions/20933/attachments/11227/21814/S3.B_3_73_Pupillo_Full-Paper.pdf

[75] Juan Esposito *et al.*, *LARAMED: A Laboratory for Radioisotopes of Medical Interest*, (2019) *Molecules*, 24(1), 20, https://doi.org/10.3390/molecules24010020

[76] Gaia Pupillo *et al.*, *The Laramed project at LNL: ^{67}Cu and ^{47}Sc production for theranostic applications*, (2020) *AIP Conference Proceedings*, 2295(1), 020001, https://doi.org/10.1063/5.0032898

[77] Syed M Qaim, *Nuclear Data Relevant to Cyclotron Produced Short-Lived Medical Radioisotopes*, (1982) *Radiochimica Acta*, 30, 147-162, https://doi.org/10.1515/9783110604375-009

[78] IAEA, *Nuclear Medicine Physics: A Handbook for Teachers and Students*, (2014) International Atomic Energy Agency, Vienna, https://www.iaea.org/publications/10368/nuclear-medicine-physics

[79] Glenn F Knoll, *Radiation Detection and Measurement*, 4th edition (2010) John Wiley & Sons, New York, NY, USA.

[80] Gyorgy Gyurky *et al.*, *The activation method for cross section measurements in nuclear astrophysics*, (2019) *The European Physical Journal A*, 55, 41, https://doi.org/10.1140/epja/i2019-12708-4

[81] Nahiko Otuka *et al.*, *Uncertainty propagation in activation cross section measurements*, (2017) *Radiation Physics and Chemistry*, 140, 502-510, https://doi.org/10.1016/j.radphyschem.2017.01.013

[82] Nahiko Otuka *et al.*, *Erratum to "Uncertainty propagation in activation cross section measurements" [Radiat. Phys. Chem. 140 (2017) 502-510]*, (2021) *Radiation Physics and Chemistry*, 184, 109440, https://doi.org/10.1016/j.radphyschem.2021.109440

[83] Lucia De Dominicis, *Proton-induced cross sections on V-nat target: focus on Sc-47 production*, Laurea magistrale, (2019) Università di Bologna, Corsi di Studio in Fisica [LM-DM270], https://amslaurea.unibo.it/18777/

[84] Francesca Barbaro *et al.*, *New results on proton-induced reactions on vanadium for ^{47}Sc production and the impact of level densities on theoretical cross sections*, (2021) *Physical Review C*, 104(4), 044619, https://doi.org/10.1103/PhysRevC.104.044619

[85] Gaia Pupillo *et al.*, *New results on the ^{nat}V(p,x)^{43}Sc cross section: Analysis of the discrepancy with previous data*, (2020) *Nuclrear Instruments and Methods in Physics Research B*, 464, 32-35, https://doi.org/10.1016/j.nimb.2019.11.032

[86] International Atomic Energy Agency, *Experimental Nuclear Reaction Data (EXFOR)*, https://www-nds.iaea.org/exfor/exfor.htm, (actively maintained and updated), last consultation: September 2023.

[87] Hanna Skliarova *et al.*, *HIVIPP deposition and characterization of isotopically enriched ^{48}Ti targets for nuclear cross-section measurements*, (2020) *Nuclear Instruments and Methods in Physics Research Section A: Accelerators, Spectrometers, Detectors and Associated Equipment*, 981, 164371, https://doi.org/10.1016/j.nima.2020.164371

[88] Sara Cisternino *et al.*, *Upgrade of the HIVIPP Deposition Apparatus for Nuclear Physics Thin Targets Manufacturing*, (2022) *Instruments*, 6(3), 23, https://doi.org/10.3390/instruments6030023

[89] Isao Sugai, *An application of a new type deposition method to nuclear target preparation*, (1997) *Nuclrear Instruments and Methods in Physics Research A: Accelerators, Spectrometers, Detectors and Associated Equipment*, 397(1), 81-90, https://doi.org/10.1016/S0168-9002(97)00733-X

[90] Sara Cisternino *et al.*, *Cryomilling of Isotope-Enriched Ti Powders for HIVIPP Deposition to Manufacture Targets for Nuclear Cross Section Measurement*, (2023) *Materials*, 16, 3926, https://doi.org/10.3390/ma16113926

[91] Matej Mayer, *SIMNRA User's Guide*, (2020) version 7.03 available at: *https://mam.home.ipp.mpg.de/SIMNRA-Users-Guide.pdf*

[92] Matej Mayer, *SIMNRA, a simulation program for the analysis of NRA, RBS and ERDA*, (1999) *AIP Conference Proceedings*, 475, 541-544, https://doi.org/10.1063/1.59188

[93] IAEA, *Ion Beam Analysis Nuclear Data Library (IBANDL)*, https://www-nds.iaea.org/exfor/ibandl.htm

[94] James F Ziegler, *SRIM-2003*, (2004) *Nuclear Instruments and Methods in Physics Research Section B: Beam Interactions with Materials and Atoms*, 219-220, 1027-1036, https://doi.org/10.1016/j.nimb.2004.01.208

[95] PubChem of National Center of Biotechnology Information of the National Library of Medicine, *Periodic Table of Elements*, https://pubchem.ncbi.nlm.nih.gov/periodic-table/

[96] Ferid Haddad *et al.*, *ARRONAX, a high-energy and high-intensity cyclotron for nuclear medicine*, (2008) *European Journal of Nuclear Medicine and Molecular Imaging*, 35(7), 1377-1387, https://doi.org/10.1007/s00259-008-0802-5

[97] Saverio Braccini, *The new bern PET cyclotron, its research beam line, and the development of an innovative beam monitor detector*, (2013) *AIP Conference Proceedings*, 1525, 144-150, https://doi.org/10.1063/1.4802308

[98] Alex Hermanne *et al.*, *Reference Cross Sections for Charged-particle Monitor Reactions*, (2018) *Nuclear Data Sheets*, 148, 338-382, https://doi.org/10.1016/j.nds.2018.02.009

[99] IAEA Monitor Reactions 2017, https://www-nds.iaea.org/medical/monitor_reactions.html (updated August 2019), last consultation: May 2023.

[100] Martin Auger *et al.*, *A detector based on silica fibers for ion beam monitoring in a wide current range*, (2016) *Journal of Instrumentation*, 11, P03027, https://doi.org/10.1088/1748-0221/11/03/P03027

[101] Tommaso S Carzaniga *et al.*, *Measurement of ^{43}Sc and ^{44}Sc production cross-section with an 18 MeV medical PET cyclotron*, (2017) *Applied Radiation and Isotopes*, 129, 96-102, https://doi.org/10.1016/j.apradiso.2017.08.013

[102] National Nuclear Data Center at Brookhaven National Laboratory, *Q-Value Calculator (QCalc)*, https://www.nndc.bnl.gov/qcalc/, (actively maintained and updated), last consultation: October 2023.

[103] E Gadioli *et al.*, *Emission of alpha particles in the interaction of 10–85 MeV protons with $^{48,50}Ti$*, (1981) *Zeitschrift für Physik A Atoms and Nuclei*, 301, 289-300, https://doi.org/10.1007/BF01421692

[104] James F Ziegler, M D Ziegler and Jochen P Biersack, *SRIM - The stopping and Range of ions in matter*, (2010) *Nuclear Instruments and Methods in Physics Research Section B: Beam Interactions with Materials and Atoms*, 268, 1818-1823, https://doi.org/10.1016/j.nimb.2010.02.091, website: http://www.srim.org/

[105] Naohiko Otuka *et al.*, *Towards a More Complete and Accurate Experimental Nuclear Reaction Data Library (EXFOR): International Collaboration Between Nuclear Reaction Data Centres (NRDC)*, (2014) *Nuclear Data Sheets*, 120, 272-276, https://doi.org/10.1016/j.nds.2014.07.065

[106] Viktor V Zerkin and Boris Pritychenko, *The experimental nuclear reaction data (EXFOR): Extended computer database and Web retrieval system*, (2018) *Nuclear Instruments and Methods in Physics Research Section A: Accelerators, Spectrometers, Detectors and Associated Equipment*, 888, 31-43, https://doi.org/10.1016/j.nima.2018.01.045

[107] Arjan J Koning and Dimitri A Rochman, *Modern Nuclear Data Evaluation with the TALYS Code System*, (2012) *Nuclear Data Sheets*, 113(12), 2841-2934, https://doi.org/10.1016/j.nds.2012.11.002

[108] Francesca Barbaro, *Cyclotron production of the innovative radionuclides ^{47}Sc, ^{155}Sc, and ^{52g}Mn: from cross section modeling to dosimetric evaluation*, (2023) Ph.D. thesis, Università di Pavia, https://iris.unipv.

it/retrieve/d433c912-874c-43bb-9453-59bfc1fc4169/BarbaroF_PhDthesis.pdf

[109] IAEA, *Cyclotron Produced Radionuclides: Principles and Practice*, (2008) *Technical Reports Series No. 465* International Atomic Energy Agency, Vienna, Austria https://www-pub.iaea.org/MTCD/Publications/PDF/trs465_web.pdf

[110] Alessandra Boschi *et al.*, *Interdisciplinary Tasks in the Cyclotron Production of Radiometals for Medical Applications. The Case of ^{47}Sc as Example*, (2019) *Molecules*, 24(3), 444, https://doi.org/10.3390/molecules24030444

[111] V N Levkovski, *Cross-Section of Medium Mass Nuclide Activation (A=40-100) by Medium Energy Protons and Alpha Particles (E=10-50 MeV)*, (1991) *Inter-Vesi*, Moscow, URSS.

[112] Sandor Takács *et al.*, *Investigation of the $^{nat}Mo(p,x)^{96mg}Tc$ nuclear reaction to monitor proton beams: New measurements and consequences on the earlier reported data*, (2002) *Nuclear Instruments and Methods in Physics Research Section B: Beam Interactions with Materials and Atoms*, 198(3-4), 183-198, https://doi.org/10.1016/S0168-583X(02)01528-8

[113] Liliana Mou *et al.*, *Nuclear Cross-Section of Proton-Induced Reactions on Enriched ^{48}Ti Targets for the Production of Theranostic ^{47}Sc Radionuclide, ^{46c}Sc, ^{44m}Sc, ^{44g}Sc, ^{43}Sc, and ^{48}V*, (2024) *Pharmaceuticals*, 17(1), 26, https://doi.org/10.3390/ph17010026

[114] H I West, R G Lanier, and M G Mustafa, *Excitation Functions for teh Nuclear Reactions on Titanium Leading to the Production of ^{48}V, ^{44}Sc, and ^{47}Sc, by Proton, Deuteron and Triton Irradiations at 0-35 MeV*, (1993) UCRL-ID-115738, https://www.osti.gov/servlets/purl/10142277

[115] A E Antropov *et al.*, *Study of the Cross Section for the Reactions (p,n), (α,pn), (α,xn) on Medium Weight Nuclei*, (1985) *Proceedings of the 35th Annual Conference of Nuclear Spectroscopy and Structure of Atomic Nuclei*, p.369, Leningrad, USSR.

[116] Shigeo Tanaka and Michiaki Furukawa, *Excitation Functions for (p,n) Reactions with Titanium, Vanadium, Chromium, Iron and Nickel up to*

Ep=14 MeV, (1959) *Journal of the Physical Society of Japan*, 14, 1269-1275, https://doi.org/10.1143/JPSJ.14.1269

[117] International Atomic Energy Agency, *Charged particle cross-section database for medical radioisotope production: diagnostic radioisotopes and monitor reactions*, (2001) *IAEA-TECHDOC-1211*, Vienna, Austria.

[118] Dassault systèmes, *Scilab software*, available at https://www.scilab.org/

[119] Michael G Stabin, *Fundamentals of Nuclear Medicine Dosimetry* (2008) Springer, New York, USA, https://doi.org/10.1007/978-0-387-74579-4

[120] ICRP, *The 2007 Recommendations of the International Commission on Radiological Protection*, (2007) ICRP Publication 103, *Annals of the ICRP*, 37 (2-4), available at: https://www.icrp.org/publication.asp?id=ICRP%20Publication%20103

[121] ICRP, *Nuclear Decay Data for Dosimetric Calculations*, (2008) ICRP Publication 107, *Annals of the ICRP*, 38 (3), available at: https://www.icrp.org/publication.asp?id=ICRP%20Publication%20107

[122] ICRP, *The ICRP Computational Framework for Internal Dose Assessment for Reference Adults: Specific Absorbed Fractions*, (2016) ICRP Publication 133, *Annals of the ICRP*, 45 (2), 1-74, available at: https://www.icrp.org/publication.asp?id=ICRP%20Publication%20133

[123] ICRP, *Basic Anatomical and Physiological Data for Use in Radiological Protection Reference Values*, (2002) ICRP Publication 89, *Annals of the ICRP*, 32 (3-4), available at: https://www.icrp.org/publication.asp?id=icrp%20publication%2089

[124] ICRP, *Adult Reference Computational Phantoms*, (2009) ICRP Publication 110, *Annals of the ICRP*, 39 (2), available at: https://www.icrp.org/publication.asp?id=ICRP%20Publication%20110

[125] Jeffry A Siegel *et al.*, *MIRD Pamphlet No. 16: Techniques for quantitative radiopharmaceutical biodistribution data acquisition and analysis for use in human radiation dose estimates*, (1999) *Journal of Nuclear Medicine*, 40(2), 37S-61S, available at: https://jnm.snmjournals.org/content/40/2/37S.long

[126] Cristina Müller *et al.*, *Promising Prospects for ^{44}Sc-/^{47}Sc-Based Theragnostics: Application of ^{47}Sc for Radionuclide Tumor Therapy in Mice*, (2014) *Journal of Nuclear Medicine*, 55, 1658-1664, https://doi.org/10.2967/jnumed.114.141614

[127] Adam L Kesner *et al.*, *MIRD Pamphlet No. 28, Part 1: MIRDcalc—A Software Tool for Medical Internal Radiation Dosimetry*, (2023) *Journal of Nuclear Medicine*, 64, 1117-1124, https://doi.org/10.2967/jnumed.122.264225

[128] Martin Andersson *et al.*, *IDAC-Dose 2.1, an internal dosimetry program for diagnostic nuclear medicine based on the ICRP adult reference voxel phantoms*, (2017) *EJNMMI Research*, 7:88, https://doi.org/10.1186/s13550-017-0339-3

[129] ICRP, *Paediatric Computational Reference Phantoms*, (2020) ICRP Publication 143, *Annals of the ICRP*, 49 (1), available at: https://www.icrp.org/publication.asp?id=ICRP%20Publication%20143

[130] Lukas M carter *et al.*, *MIRD Pamphlet No. 28, Part 2: Comparative Evaluation of MIRDcalc Dosimetry Software Across a Compendium of Diagnostic Radiopharmaceuticals*, (2023) *Journal of Nuclear Medicine*, 64, 1295-1303, https://doi.org/10.2967/jnumed.122.264230

[131] Michael G Stabin, Richard B Sparks and Eric Crowe, *OLINDA/EXM: The Second-Generation Personal Computer Software for Internal Dose Assessment in Nuclear Medicine*, (2005) *Journal of Nuclear Medicine*, 46(6), 1023-1027, available at: https://jnm.snmjournals.org/content/46/6/1023

[132] Michael G Stabin and Adam Farmer, *OLINDA/EXM 2.0: The new generation dosimetry modeling code*, (2012) *Journal of Nuclear Medicine*, 53(supplement 1), 585, available at: https://jnm.snmjournals.org/content/53/supplement_1/585

[133] Laura De Nardo *et al.*, *Preliminary dosimetric analysis of DOTA-folate radiopharmaceutical radiolabelled with ^{47}Sc produced through $^{nat}V(p,x)^{47}Sc$ cyclotron irradiation*, (2021) *Physics in Medicine and Biology*, 66, 025003 https://doi.org/10.1088/1361-6560/abc811

[134] Michael G Stabin *et al.*, *RADAR reference adult, pediatric, and pregnant female phantom series for internal and external dosimetry*, (2012) *Journal of*

Nuclear Medicine, 53(11), 1807-1813 https://doi.org/10.2967/jnumed.112.106138

[135] ICRP, *Adult mesh-type reference computational phantoms*, (2020) ICRP Publication 145, *Annals of the ICRP*, 49 (3), available at: https://www.icrp.org/publication.asp?id=ICRP%20Publication%20145

[136] ICRP, *Limits for Intakes of Radionuclides by Workers*, (1979) ICRP Publication 30 (Part 1), *Annals of the ICRP*, 2 (3-4), available at: https://www.icrp.org/publication.asp?id=ICRP%20Publication%2030%20(Part%201)

[137] Laura Meléndez-Alafort *et al.*, *Internal radiation dose assessment of radiopharmaceuticals prepared with cyclotron-produced* ^{99m}Tc, (2019) *Medical Physics*, 46(3), 1437-1446 https://doi.org/10.1002/mp.13393